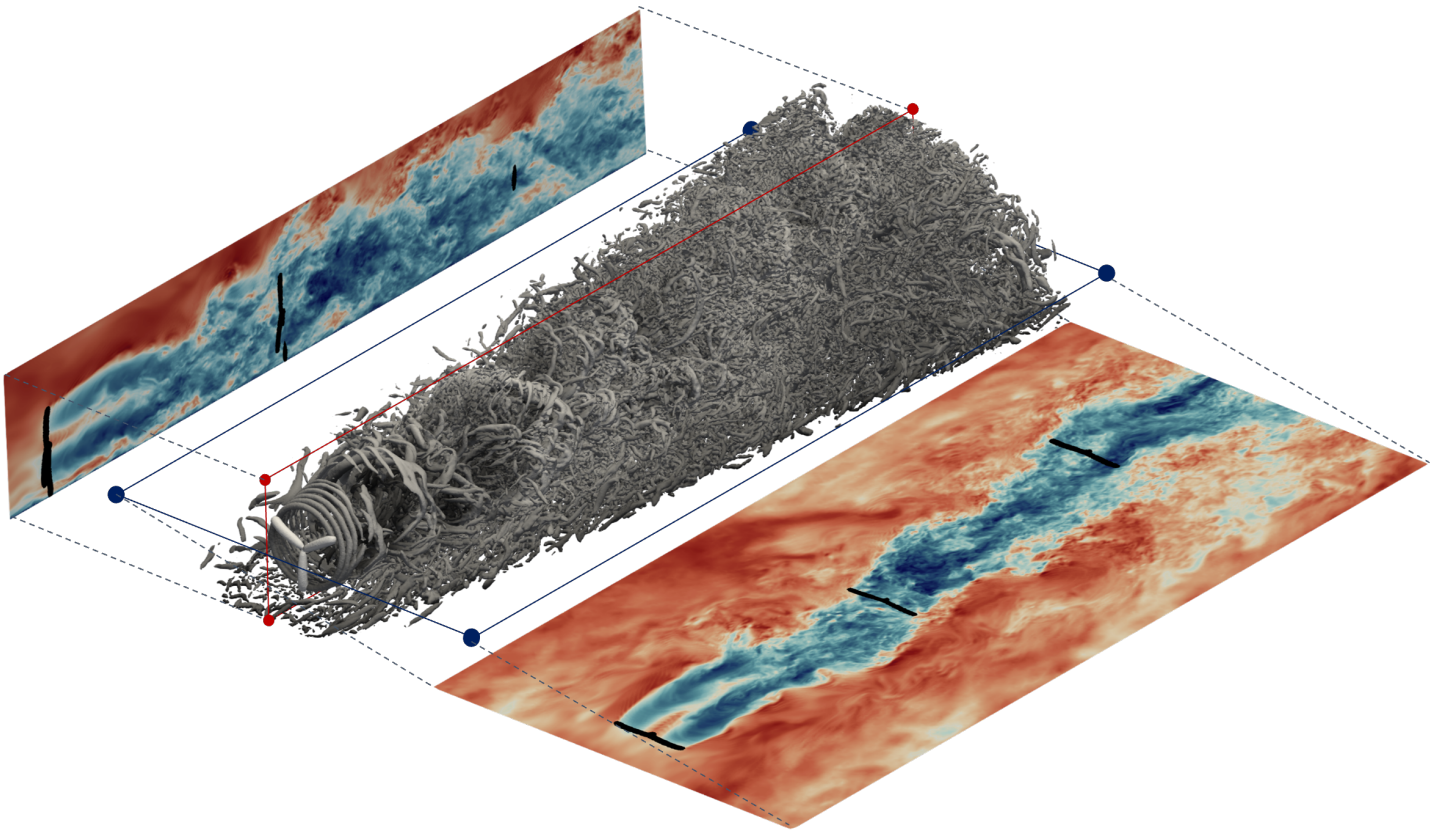


Automation and Parametric Investigation of Wind Turbine Wakes in an Aero-Servo-Elastic Large Eddy Simulation Framework

Graduation Project (SET3901)

Ansh Patel



Automation and Parametric Investigation of Wind Turbine Wakes in an Aero-Servo-Elastic Large Eddy Simulation Framework

Graduation Project (SET3901)

Thesis report

by

Ansh Patel

to obtain the degree of Master of Science
at the Delft University of Technology
to be defended publicly on October 12, 2023

Thesis committee:

Chair: Prof.dr.ir. A. Viré (TU Delft)
Supervisor: Dr. F. Houtin-Mongrolle (Siemens Gamesa)
External examiner: Dr. S.J. Hulshoff (TU Delft)
Place: Faculty of Aerospace Engineering, Delft
Project Duration: December, 2022 - September, 2023
Student number: 5450624

An electronic version of this thesis is available at <http://repository.tudelft.nl/>.



Copyright © Ansh Patel, 2023
All rights reserved.

Abstract

Wind turbine wakes have been a topic of intense research since the maturation of wind energy. This is justified given the complexity of the physics involved and their crucial impact on the operation of a wind turbine. Only recently though, the advancement in computational resources and the development of models like the Actuator Line Method (ALM), has made it possible to study wind turbine wakes while capturing their multi-scale and multi-physical aspects. In this regard, the Actuator Line - Large Eddy simulation framework has become an academic and industrial standard. Thus, this thesis has been carried out under the joint supervision of Siemens Gamesa Renewable Energy and TU Delft to study wind turbine wake interaction using the coupling between the LES library YALES2 and the servo-structural solver BHawC. The latter extends the framework to include the effects of control and structural deformation. It allows for the simulation of real wind turbines with their industrial controller.

The aim of the project was twofold, involving the development of an automatic workflow for coupled ALM-LES of wind turbine wakes which is then used to gather insights into the impact of inflow conditions on wake properties as well as the structural impact of different partial-wake incidence scenarios.

The workflow integrates the steps of external flow convergence, mesh refinement in the wake region and generation of the converged and time-averaged flow field. It allows parametric studies to be carried out with minimal intervention from the user, while ensuring the reliability of the results. With respect to the external flow, the recycling method was used to obtain fully developed turbulence with sufficient control on the turbulence properties.

An investigation of the inflow conditions showed the sensitivity of the velocity field in the wake to the ambient turbulence and wind speed. An increase in ambient TI from 5% to 10% led to 35% more wake expansion in the lateral direction and 30% faster wake recovery. The ambient wind speed played an important role in recovery by determining the operating condition of the upstream turbines which in turn affected the wake-added turbulence. An analysis of wake meandering showed that this phenomena is largely dependent on the ambient turbulence.

Lastly, the structural impact of two different partial-wake interaction scenarios was studied to highlight the importance of accounting for the wake position on the rotor of downstream turbines while carrying out load assessments. In one scenario, the turbine operated in half-wake and half free-stream while in the other, it operated under two half-wakes. It was observed that at above-rated wind speed, the first scenario led to a 35% increase in the flap-wise damage accumulated by the blade. On the other hand, the edge-wise damage changed by 4%. These results emphasized the need for considering the spatial distribution of the wake on the downstream turbines.

Acknowledgements

First of all, I would like to thank Axelle for supervising the thesis from the university's side and for acting as the chair of the thesis committee. I really appreciate the support you provided throughout the project. I would also like to thank Steven for agreeing to be a part of the committee and acting as the external examiner. Finally, I want to thank Félix for providing daily guidance and feedback. Given the numerous challenges that we faced, it would not have been possible to complete this project in such a successful manner without your support. I have learned a lot from you and it was a pleasure to work together.

Next, I would like to thank my team at SGRE. Paul, thank you for making this project possible. Laurent, I am grateful for your insights and feedback on my work. Etienne, I really appreciate your assistance in running and debugging the simulations as well as for giving feedback related to the YALES2 setup. I also appreciate the assistance of Bastien and Ricardo at various stages of the project.

I am grateful to my parents for their love and support, you contributed to this thesis in your own way. To the rest of my family back home, a big thank you. I am also grateful for all my friends from the university, Nicola, Anastasis, Ziad, Alessio, Carlo and Pietro for always providing a much-needed break from the thesis. Thank you Nirav for all the fruitful (and sometimes funny) discussions on CFD. Lastly, I am grateful for you Shriya. Thank you for always being with me.

This work is part of the W2ITASEC (Wind turbine Wake Interactions through Aero-Servo-Elastic Coupling) project provided with computer and storage resources by GENCI at TGCC thanks to the grant 2023-S142aspe00038 on the supercomputer Joliot Curie's ROME partition.

Contents

Abstract	ii
Acknowledgements	iii
List of Figures	vi
List of Tables	xi
1 Introduction	1
2 Background and literature review	3
2.1 An introduction to wind turbine wakes	3
2.2 Numerical modelling of wind turbine wakes	4
2.3 Computational Fluid Dynamics	6
2.4 Large Eddy Simulation	8
2.5 YALES2	10
2.6 Turbine modelling	12
2.7 BHawC coupling: an elastic ALM-LES implementation.	19
2.8 Literature review conclusion	25
3 Inflow conditions: recycling method for turbulence generation	27
3.1 An introduction to turbulence generation for LES	27
3.2 Recycling method for turbulence generation	29
3.3 Sensitivity study	30
3.4 Parametric study on the ground roughness and inlet flow-rate.	36
4 Towards a parametric study of wind turbine wakes	40
4.1 Steps in a typical wind turbine wake simulation	40
4.2 Wake tracking method	41
4.3 Mesh refinement procedure	42
4.4 Workflow for studying wind turbine wake interactions	49
5 Impact of inflow on multi-wake interaction	52
5.1 Simulation setup	52
5.2 Results	55
6 From full wake to half wake interaction: structural impact	67
6.1 Simulation setup	67
6.2 Results	69
7 Conclusion and recommendations	80
7.1 A reply to the research questions	80
References	88
A Appendix 1: Estimation of CPU costs	89

Nomenclature

List of Abbreviations

ABL	Atmospheric Boundary Layer
ADM	Acuator Disk Method
ALM	Acuator Line Method
BEM	Blade Element and Momentum theory
BHawC	Bonus Horizontal Axis Wind turbine simulation Code
CFD	Computational Fluid Dynamics
CFL	Courant-Friedrichs-Lewy condition
DNS	Direct Numerical Simulations
DWM	Dynamic Wake Meandering model
L1	Layout 1
LES	Large Eddy Simulations
RANS	Reynolds Averaged Navier Stokes
T1	The 1st turbine in the domain, as seen from the inflow direction
YALES2	Yet Another Large Eddy Simulation code 2

List of Symbols

\bullet	The LES filtering operator [-]
ϵ	Mollification kernel width [m]
\hat{u}	The velocity deficit in the wake [m/s]
κ	Von-Kármán constant [-]
$\langle \bullet \rangle$	The time-averaging operator [-]
μ	Dynamic viscosity [kg/ms^2]
ν	Kinematic viscosity [m^2/s^2]
ν_t	Turbulent eddy viscosity [m^2/s^2]
ϕ	Distance function for the level-set [m]
ψ	The scalar level-set field [-]

ρ	air density [kg/m^3]
τ_{ij}	Shear stress in the i -th direction on the j -th plane [N/m^2]
C_D	Airfoil drag coefficient [-]
C_L	Airfoil lift coefficient [-]
DEL	The damage equivalent load [kNm]
F_m	Variable to flag the wind turbine wake [-]
G	LES filter function [-]
h	Mesh element size [m]
p or P	Pressure field [N/m^2]
Re	Reynolds number [-]
St	Strouhal number [-]
t	Simulation time-step [s]
t_{F_m}	Threshold on the time-averaged wake flag $\langle F_m \rangle$ [-]
TI_x	The turbulence intensity in the stream-wise direction.
TI_{ref}	The target turbulence intensity over the rotor plane of the 1st turbine for a certain inflow condition [%]
u'	Turbulent fluctuations in the velocity field [m/s]
u_i or U_i	i -th component of the velocity field [m/s]
u_*	Friction velocity [m/s]
u_{ref}	The target velocity at hub height for a certain inflow condition [m/s]
x	The stream-wise direction [m]
y	The lateral or transverse direction [m]
z	The vertical direction [m]
z_0	Ground roughness [m]

List of Figures

2.1	Horns Rev, North Sea, Denmark- Low-hanging fog leads to a picturesque visualization of the wake generated by a wind turbine - <i>photo by Bel Air Aviation Denmark-Helicopter Services. January 26th, 2016</i>	3
2.2	Evolution of the velocity profile in the wake- <i>from Figure 6 pg 14. of Aerodynamics of Wind Turbine Wakes by B. Sanderse[13]</i>	4
2.3	A Large Eddy Simulation of a wind farm showing the instantaneous stream-wise velocity contours- <i>from Figure 2a pg. 7 of A Comparison of the Dynamic Wake Meandering Model, Large-Eddy Simulation, and Field Data at the Egmond aan Zee Offshore Wind Plant by M.Churchfield et al.[15]</i>	5
2.4	Ranking numerical methods in terms of computational cost (measured in CPU-hrs) and fidelity for the simulation of a single wind turbine wake	6
2.5	Level of fidelity achieved by different CFD methodologies when applied to the same fluid problem: high-speed jet flow- <i>from Figure 5.4 pg 199 of Applied Computational Fluid Dynamics and Turbulence Modelling by S.Rodriguez [7]</i>	8
2.6	Snapshots of iso-vorticity in the whole domain for different sub-grid models. NO stands for no sub-grid model, DMO for Dynamic Mix - ω model, DS for Dynamic Smagorinsky model and DMs for Dynamic Mix-S model. All four predict the destabilization of the vortices equally well but in the NO model due to a lack of dissipative terms, smaller eddies are seen - <i>from Figure 14 page 396 of Role of subgrid-scale modeling in large eddy simulation of wind turbine wake interactions by H.Sarlak et al.[25]</i>	9
2.7	An overview of the features of YALES2 - <i>taken from the YALES2 public wiki [30]</i>	10
2.8	Depiction of Double Domain Decomposition (left). Cells are divided once between processors and again for preconditioning as shown by the light grey highlights. The cells within the black outline facilitate communication between processors. The communication schematic is shown on them right- <i>from Figure 3 and 4, pg. 144 of Design of a massively parallel CFD code for complex geometries by V.Moureau, P.Domingo and L.Vervisch [9]</i>	11
2.9	Geometrical modelling involved in the Actuator Disk and Actuator line models- <i>from Figure 1 pg 3 of A Comparison of Actuator Disk and Actuator Line Wind Turbine Models and Best Practices for Their Use by L.Martínez et al.[41]</i>	13
2.10	Comparison of the streamwise velocity contours on the isosurface of the second-invariant of velocity gradient tensor as computed with the Actuator Line (left) and Actuator Disk Method (right). The difference in the near wake is visible wherein the Actuator Line Method produces the helical vortices- <i>from Figure 2 pg 3 of A Comparison of Actuator Disk and Actuator Line Wind Turbine Models and Best Practices for Their Use by L.Martínez et al.[41]</i>	14
2.11	A comparison of the measured power curve of the Nordtank 500/41 wind turbine with its Actuator Line Model- <i>from Figure 4 pg. 397 of Numerical Modeling of Wind Turbine Wakes by J. Sørensen et al. [8]</i>	14
2.12	Schematic representation of the steps involved in ALM- <i>from Figure 2.9 pg. 38 of Investigations of yawed offshore wind turbine interactions through aero-servo-elastic Large Eddy Simulations by F. Houtin-Mongrolle [36]</i> . In a) the discretization of the blade is shown along with the axes orientations of the elements. b) depicts the velocity evaluation as the sum of the local gas and blade velocities. And in c) the force mollification is shown, where the kernel approximates a Gaussian distribution.	16
2.13	The body force projection as viewed from upstream (top row) and the side (bottom row) for the two different mollification kernels. It can be observed that the anisotropic kernel yields a shape similar to the blade profile- <i>from Figure 1 pg. 5 of An Advanced Actuator Line Method for Wind Energy Applications and Beyond by M. Churchfield et al.[48]</i>	17

2.14	Q-criterion isosurfaces showing the difference in the wake structure for the two mollification methods - from Figure 1 pg. 5 of <i>An Advanced Actuator Line Method for Wind Energy Applications and Beyond</i> by M. Churchfield et al.[48]	17
2.15	Comparison of the vorticity isocontours for the classical (left) and filtered (right) Actuator Line Methods showing similar wake development- from Figure 12 pg. 10 of <i>Large-Eddy Simulation of a wind turbine using a Filtered Actuator Line Model</i> by R. Stanly et al.[49]	18
2.16	Instantaneous stream-wise velocity contours on a plane passing through the turbine center showing the differences between a wake produced with (bottom) and without (top) a tower and nacelle model. Here the only the C_p model is shown -from Figure 5 pg. 10 of <i>Modeling Wind Turbine Tower and Nacelle Effects within an Actuator Line Model</i> by M. Churchfield et al.[50]	18
2.17	The top view of the lateral velocity profile at a distance 2.8D downstream. In the flat terrain (left), the wake is symmetric while the complex terrain (right) causes a drift of the computed wake center as well as a much stronger deficit -from page 6 Figure 7 of <i>CFD three dimensional wake analysis in complex terrain</i> by F. Castellani et al.[53]	19
2.18	YALES2-BHawC coupling strategy - from Figure 5.2 pg. 137 of <i>Investigations of yawed offshore wind turbine interactions through aero-servo-elastic Large Eddy Simulations</i> by F. Houtin-Mongrolle [36]. For each temporal loop, force-displacement information is only exchanged once.	20
2.19	A simplified flowchart of the YALES2-BHawC coupling.	21
2.20	The instantaneous velocity contour showing the wake behind the full-resolved geometry of the turbine- from Figure 13 pg. 830 of <i>Fluid–structure interaction modeling of wind turbines: simulating the full machine</i> by M. Hsu et al.[56]	22
2.21	The aerodynamic power output computed by OpenFAST for the upstream, unwaked turbine under a turbulent inflow of 4%- from Figure 19a pg. 16 of <i>Numerical investigations of coupled aeroelastic performance of wind turbines by elastic actuator line model</i> by J. Zheng et al.[62]	23
2.22	The streamwise velocity contours averaged over 20 seconds on a plane perpendicular to the inflow direction at different downstream distances - from Figure 16 pg. 14 of <i>Numerical investigations of coupled aeroelastic performance of wind turbines by elastic actuator line model</i> by Zheng et al.[62]	23
2.23	The time-averaged axial velocity deficit (top) and the turbulent kinetic energy (bottom) 1D downstream of the second turbine showing how the wake profile is affected by the wind veer- from Figures 8 and 10 pgs. 1101 and 1103 of <i>Large Eddy Simulation of wind turbine wake interaction in directionally sheared inflows</i> by W. Chanprasert et al. [63]	24
2.24	Bar plots showing the Damage Equivalent Load (DEL) for the rotor shaft torque (right) and the yaw bearing moment (left)- Figure 9 pg. 217 from <i>Large Eddy Simulation of wind turbine fatigue loading and yaw dynamics induced by wake turbulence</i> by W. Chanprasert et al. [64]	24
2.25	The Q-criterion isosurface showing the instantaneous flow velocity behind a 2.3MW turbine as simulated by EllipSYS3D- from Figure 9 of <i>Wind turbines in atmospheric flow: fluid–structure interaction simulations with hybrid turbulence modeling</i> by C. Grinderslev et al. [66]	25
3.1	The shear profile obtained by synthetic turbulence with the Mann spectra [78] compared with the profile that was injected at the inlet. Note that the resultant profile is sourced from a location 3000m downstream of the inlet.	28
3.2	Visual Depiction of a Precursor simulation- from Figure 1 pg. 561 of <i>Inlet conditions for large eddy simulation: A review</i> by G. Tabor et al.[76].	29
3.3	Principle of the recycling method showing the definition of the recycling plane (right) and the interpolation of the Lagrangian particles back to the inlet (left) from Figure 4 and 5 pg. 4 of <i>Roughness-Resolved Large-Eddy Simulation of Additive Manufacturing-Like Channel Flows</i> by S. Meynet et al. [81].	29
3.4	Example of recycling and Rescaling method, showing the impact of the development of boundary layer on the recycled profile- from Figure 1a pg. 32 of <i>Inflow Turbulence Generation Methods</i> by X. Wu [70].	30
3.5	A representation of the domain showing the dimensions, the length of the recycling region and the recycling plane (in green). Note, x is the stream-wise direction, y is the transverse or lateral direction and z is the vertical direction.	31

3.6	From top to bottom: the iso-contour of the instantaneous stream-wise velocity (U_x), the time-averaged stream-wise velocity ($\langle U_x \rangle$) and the stream-wise turbulence intensity (TI_x) on a vertical slice normal to the lateral direction (left) and another slice normal to the stream-wise direction (right). The recycling plane is indicated by the gray line whereas the black line denotes the turbine location in the subsequent simulations.	32
3.7	Velocity field time averaged statistics for the baseline case. The stream-wise velocity component along the vertical direction showing the resultant shear profile at different stream-wise locations defined with respect to the inlet (a), the stream-wise turbulence intensity also along the vertical direction (b), the stream-wise velocity component along the lateral direction (c) and finally the shear profile at the turbine location fitted to a power law (d). The dashed black lines indicate the rotor plane.	33
3.8	The rotor averaged TI_x for different cases	34
3.9	The error from the shear profile ϵ_r (refer Eq. (3.10)) for different cases expressed as percentage of the target velocity at hub height (7m/s)	35
3.10	The root-mean-square of the fluctuations in the stream-wise velocity along the lateral direction $\sigma_{\langle U_x^y \rangle}$ (refer Eq. (3.11)) for different cases expressed as a percentage of the target velocity at hub height (7m/s)	36
3.11	From top to bottom: the iso-contour of U_x , $\langle U_x \rangle$ and TI_x on a vertical slice normal to the lateral direction (left) and another slice normal to the stream-wise direction (right), for the case with $z_0 = 0.17$ and $u_{ref} = 6m/s$. The recycling plane is indicated by the gray line whereas the black line denotes the turbine location in the subsequent simulations.	37
3.12	The rotor-averaged turbulence intensity as a function of the surface roughness. Note, the data are fit using a function which is of the form: $y = ce^{mx}$	38
3.13	Left: the average wind speed at hub in the stream-wise direction obtained at the end of recycling for different roughness and wind speed combinations. Right: the shear coefficient of the fitted power-law profile obtained at the end of recycling for different roughness and wind speed combinations.	38
4.1	Mesh refinement on a structured grid using refinement zones- <i>from Figure 9 pg. 9 of Numerical investigations of coupled aeroelastic performance of wind turbines by elastic actuator line model by J. Zheng et al. [62]</i>	41
4.2	Left: iso-contour on the instantaneous level-set field at a value of 0.5 showing its evolution with the flow. Right: Top view of the level-set field on a plane at hub-height.	42
4.3	The mesh before the refinement procedure is implemented. Top: the iso-contours of the cell size (h) in meters on a horizontal plane at hub height. Bottom: the same but on a vertical plane passing through the rotor centers.	43
4.4	The iso-contours on the time-averaged Metric Flag $\langle F_m \rangle$ shown on a vertical slice of the domain.	44
4.5	The mesh resulting from the refinement strategy presented in this subsection with $t_{\langle F_m \rangle} = 0.4$. Note that the cell size in the wake is $\frac{D}{32}$ m.	44
4.6	The variation in mesh size with $t_{\langle F_m \rangle}$ when starting from a mesh of 11 Million cells.	45
4.7	The comparison of the meshes obtained when using a threshold of 0.01 and 0.9 shown on a vertical slice passing through the rotor center for the case of two turbine operating in a line.	45
4.8	The root-mean-square of the level-set showing the extreme position of the wake on a vertical (bottom) and horizontal (top) slice at hub height computed on a mesh with $t_{\langle F_m \rangle} = 0.01$. All the values of $\psi_{RMS} > 0$ are inside the refinement zone.	46
4.9	The root-mean-square of the level-set showing the extreme position of the wake on a vertical (bottom) and horizontal (top) slice at hub height computed on a mesh with $t_{\langle F_m \rangle} = 0.9$	47
4.10	The vertical profile of the stream-wise time-averaged velocity (left), the stream-wise turbulence intensity (center) and the cell size (right) at a distance of 3D downstream of T2, with the different lines corresponding to values of $t_{\langle F_m \rangle}$. The solid black line highlights the upper limit till where the error ϵ_r was computed and the dashed black lines indicate the turbine location.	47
4.11	The vertical profile of the stream-wise time-averaged velocity (left), the stream-wise turbulence intensity (center) and the cell size (right) at a distance of 7D downstream of T2.	48

4.12	The iso-contour of the cell sizes on a vertical slice passing through the rotor centers, showing the difference in the resultant mesh when using the same threshold of 0.9 but for different inflow conditions.	49
4.13	An example of a workflow from start to finish. The slices of the domain are taken on a vertical plane passing through the rotor center.	50
5.1	Top: Side view of the simulated domain showing the turbine separation and relative size of the recycling zone. Bottom: Top view of the same domain.	53
5.2	Top: Side-view of the mesh on a vertical plane passing through the rotor center wherein $u_{ref} = 8m/s$ and $TI_{ref} = 5\%$. Bottom: Top-view of the mesh on a plane at hub-height.	54
5.3	A comparison of the $\langle U_x \rangle$ profile along the z-direction in the wake of T3, at a distance of 1D and 7D from it.	56
5.4	A comparison of the electrical power output (P_{elec}), the rotation speed (ω) and the blade pitch angle (Ψ) for all three turbines for different mesh resolutions. The error bars show the respective standard deviation.	56
5.5	The sample of the time series of the power output of turbine T3 (left) for different mesh resolutions and its Fourier transform over the total physical time of the simulation (right).	57
5.6	The instantaneous velocity field visualized on a vertical plane passing through the rotor center.	57
5.7	The time-averaged velocity field visualized on a vertical plane passing through the rotor center.	58
5.8	The turbulence intensity in the stream-wise direction visualized on a vertical plane passing through the rotor center.	59
5.9	The profile of the time-averaged stream-wise velocity deficit along the z-direction at different stream-wise positions behind T3. Note, the points are sampled at $y = 0$ or along the center-line of the domain.	60
5.10	The profile of the time-averaged stream-wise velocity deficit along the y-direction at different stream-wise positions behind T3. Note, the points are sampled at $z = 105.52m$ or at the hub height.	60
5.11	The profile of TI_x along the z-direction at different stream-wise positions behind T3. Note, the points are sampled at $y = 0$ or along the center-line of the domain.	61
5.12	The time-averaged power output for each turbine under the five inflow conditions, normalized by its rated value. The error bars show the standard deviation.	61
5.13	The evolution of rotor-averaged stream-wise velocity along the stream-wise direction.	62
5.14	The stream-wise evolution of TI_x in the wake.	63
5.15	The time series of y_c as computed by the minimum available power method for the 8m/s and 10% TI case at a location of 3D downstream of T2.	64
5.16	The mean location of the wake center at different stream-wise locations with the error bars denoting the standard deviation for the $u_{ref} = 8m/s$ cases.	65
5.17	The mean location of the wake center at different stream-wise locations with the error bars denoting the standard deviation for the $u_{ref} = 14m/s$ cases.	65
5.18	The Fourier Transform of the y_c at different stream-wise locations.	66
6.1	A representation of the Layout "L1" wherein half-wakes from T1 and T2 impact the same side of T3.	68
6.2	A representation of the Layout "L2" wherein half-wakes from T1 and T2 impact opposite sides of T3.	68
6.3	A Q-criterion iso-surface visualizing the turbulence generated in the wake as well as the helical tip vortices in L2 8m/s case. A value of $Q_{crit} = 0.02s^{-2}$ is used as the threshold.	69
6.4	The instantaneous velocity field visualized on a horizontal plane at hub height.	69
6.5	The time-averaged velocity field visualized on a horizontal plane at hub height.	70
6.6	The turbulent intensity in the stream-wise direction visualized on a horizontal plane at hub height.	70
6.7	The instantaneous and time-averaged inflow on T3 (here highlighted by the black lines) in all of the four cases	71
6.8	The profile of $\langle U_x \rangle$ along the lateral direction at a distance of 1D upstream of T3 in the L1 configuration. The black lines indicate the rotor location of T3.	72

6.9	The profile of $\langle U_x \rangle$ along the lateral direction at a distance of 1D upstream of T3 in the L2 configuration. The black lines indicate the rotor location of T3.	72
6.10	A comparison of the electrical power output (P_{elec}), the rotation speed (ω) and the blade pitch angle (Ψ) for all three turbines for the four cases. The error bars show the respective standard deviation.	73
6.11	The time series for the flap-wise bending moment on blade 1 of T3 and its Fast Fourier Transform for the L1 and L2 8m/s cases	73
6.12	The time series for the edge-wise bending moment on blade 1 of T3 and its Fast Fourier Transform for the L1 and L2 8m/s cases	74
6.13	The azimuthal and radial distribution of the time-averaged flap-wise force on T3. On the left Layout L1 is shown while L2 is on the right.	74
6.14	The azimuthal and radial distribution of the time-averaged edge-wise force on T3. On the left Layout L1 is shown while L2 is on the right.	75
6.15	The azimuthal distribution of the tip deflection in the flap-wise direction on T3. On the left the cases for the 8m/s wind speed are shown while 14m/s is on the right.	76
6.16	The azimuthal distribution of the tip deflection in the edge-wise direction on T3. On the left the cases for the 8m/s wind speed are shown while 14m/s is on the right.	76
6.17	The Damage Equivalent Load in the flap-wise direction at the blade root of T3 expressed as the relative difference with respect to T1	78
6.18	The Damage Equivalent Load in the edge-wise direction at the blade root of T3 expressed as the relative difference with respect to T1	78
6.19	The Damage Equivalent Load in yaw on the tower top of T3 expressed as the relative difference with respect to T1	79

List of Tables

3.1	Boundary conditions and other details for the baseline case	31
3.2	The inflow conditions used in Chapter 5	38
3.3	The inflow conditions used in Chapter 6	39
4.1	Error in the $\langle U_x \rangle$ and $\langle TI_x \rangle$ vertical profiles for different thresholds	48
5.1	The inflow conditions used for the parametric study	53
5.2	Boundary conditions on each wall of the domain	53
5.3	Solver settings and other relevant details of the simulation	54
6.1	The inflow conditions used for the study	68
A.1	Overview of Wall Clock Time, Number of Processors and CPU consumption for the simulations of Chapter 5 and 6.	89
A.2	The Reduced Computational Time (RCT) of the simulation steps.	90

Introduction

The growth in wind energy was the highest among all renewable energy technologies [1] in 2021. While the installed capacity reached 831GW, current projections are not expected to meet the requirements of the net zero scenario by 2050 [2]. This is mainly due to the costs of offshore wind which is expected to be the dominant wind energy market by 2025. In particular, manufacturing costs account for a significant percentage of the capital costs of a wind turbine [3]. These are often non-optimal due to an over-conservative design approach. Thus, a first-order cost reduction method would be to gain a better understanding of the loads on a wind turbine and subsequently optimize the design methodologies to achieve a trade-off between the costs and the reliability of the system. In other words, a reduction in the uncertainty of wind turbine loads would lead to a more cost-efficient design.

In recent years, the wind turbine wake is largely responsible for the design uncertainty [4]. It is defined as the region of reduced velocity and higher than ambient turbulence downstream of a turbine caused by the extraction of kinetic energy from the free-stream flow. With the growth of wind energy, turbines are becoming clustered in a wind farm. Consequently, the wake from upstream turbines has an increasing effect on the operation of their downstream counterparts. For example, the higher turbulence causes load fluctuations which currently has a wide margin for uncertainty [4]. Engineering models, used in the design and certification process, tackle this uncertainty by being conservative while computing the loads [5]. They cannot replicate all of the phenomena occurring in the wake. This is because in order to handle thousands of design cases, these models are of low to mid fidelity. Hence, a conservative design approach is the current norm.

One of the important topics of wind energy research is the improvement of engineering models to reduce the aforementioned uncertainty and achieve more accurate estimates of wind turbine loads and performance. A method of improving engineering models is to use the insights gathered from experiments or simulation methods of higher fidelity [6]. But, there are two problems that must be addressed in this domain. Any method attempting to replicate wind turbine wakes must include its multi-scale and multi-physical aspects [5].

The multi-scale aspect is due to the presence of a large range of spatial and temporal scales in the flow. Indeed, the spatial scales can range from the Kolmogorov micro-scale ($1e^{-6}m$) to the size of a wind farm ($1e^4m$). Experiments on this scale are infeasible and hence flow simulation is the preferred method [5]. Here, Large Eddy Simulations (LES) provide a partial answer by effectively reducing the range of scales [7]. The largest scales of the flow are resolved while the smaller ones are treated by models. But, given the limits of current computational resources, a LES with a resolved wind turbine geometry is still too expensive. The range of spatial and temporal scales is still too large which means that a solution cannot be obtained in a feasible amount of time.

The multi-scale problem is solved by the use of the Actuator Line Method (ALM) [8]. The turbine geometry is no longer resolved and its effect on the flow field is modelled. This involves computing the lift and drag forces of the turbine based on the local velocity field and the airfoil polars. The computed forces are then introduced as source terms in the momentum equations. This results in the ALM-LES framework which is explained in detail in Chapter 2.

But, the multi-physical aspect is not addressed by ALM-LES. This aspect stems from the structural deformation of the turbine and the imposed control. In order to include these effects, a fluid-structure

interaction simulation (FSI) is necessary. A FSI simulation is obtained by coupling the ALM-LES framework to a servo-structural solver. In this thesis, the coupling between the LES library YALES2 [9], and the servo-structural solver BHawC [10] is used. The YALES2-BHawC coupling provides a method of studying the physics of wind turbine wakes while replicating its multi-scale and multi-physical nature. It is also described in Chapter 2.

As mentioned earlier, the wind turbine wake involves phenomena such as the development and breakdown of tip and root vortices, the recovery of the wind speed by exchange of kinetic energy and momentum with the free-stream flow and wake meandering due to its interaction with the ambient turbulence. Insights gathered by analysing the sensitivity of these phenomena to the change in the turbine layout, inflow conditions, etc, can be used to improve engineering models. This requires a parametric study which are currently difficult to carry out. This is because a coupled ALM-LES involves a number of steps ranging from the convergence of the external flow to mesh adaptation and accumulation of the final statistics. Significant human time can be spent on repeating these steps for all the cases in a parametric study. More importantly, the reliability of the results is questionable since the mesh generated is based on "human-judgement". This is elaborated upon in Chapter 4.

Thus, the aim of this thesis is as follows:

1. Develop a method of stream-lining the setup of coupled ALM-LES to enable parametric studies on a number of topics (such as turbine layout, yaw, inflow conditions). This involves the creation of a workflow by integrating the process of inflow initialization, mesh generation, wake convergence and accumulation of statistics. The mesh generation in particular must be based on the properties of the flow itself to also ensure the reliability of the results.
2. Analyse a three turbine in-line configuration under different wind speeds and ambient turbulence to study their impact on velocity profiles in the wake, wind speed recovery and meandering.
3. Differentiate between the structural impact of different partial-wake interaction scenarios to highlight the importance of modelling the spatial distribution of the wake over the rotor plane.

This report is ordered as follows: Chapter 2 starts from an introduction of wind turbine wakes, providing an overview of Large Eddy Simulations, the Actuator Line Method and Fluid-Structure Interaction simulation, ending with a summary of studies carried out using the same methodology. Chapter 3 provides an investigation into the recycling method for generating turbulence which will then be used to set the inflow boundary condition for all subsequent simulations. Chapter 4 explains the workflow developed for parametric investigation of wind turbine wakes. Chapter 5 investigates a three turbine configuration under different wind speeds and inflow turbulence. Chapter 6 analyses the impact of half-wake superposition on the wind turbine structure. Chapter 7 concludes the report, highlighting the most interesting outcomes while providing recommendations for future studies.

Background and literature review

This chapter aims to provide the background Actuator Line Large Eddy simulations of wind turbines wakes. Starting from an overview of the field, the discussion is orientated towards presenting the methodology used in this project: the CFD library YALES2 and its coupling with the servo-elastic solver, YALES2-BHawC. In addition to the relevant numerical details, a review of past studies in the field is also included.

The chapter is ordered as follows: first, a brief introduction to wind turbine wakes is presented. Next, the methods used for modelling wakes are shown followed by a more detailed discussion of Computational Fluid Dynamics (CFD) and in particular Large Eddy Simulations (LES). Moreover, some features of YALES2 are elucidated upon. Then, turbine modelling methods in CFD simulations are discussed. Herein, the Actuator Line Method (ALM) is explained in detail. The subsequent section presents the YALES2-BHawC coupling, used to carry out Fluid Structure Interaction simulations in this project. Also included is a review of studies which have developed and used similar couplings. Lastly, the conclusions from the literature review are presented along with a reformulation of the research question which will form the final objectives of the thesis.

2.1. An introduction to wind turbine wakes



Figure 2.1: Horns Rev, North Sea, Denmark- Low-hanging fog leads to a picturesque visualization of the wake generated by a wind turbine - *photo by Bel Air Aviation Denmark-Helicopter Services. January 26th, 2016*

The wake of a wind turbine is chiefly characterized by the velocity deficit caused by the extraction kinetic energy from the atmospheric flow. It is also a region of higher-than-ambient turbulence, as was famously

captured in the photograph in Fig. 2.1. From an analytical perspective, the wake can be divided into two parts: the near and far wake region. The former extends up to one or three turbine diameters behind the rotor plane and shows a clear vortex structure as a result of the vortices shed from the blade tip and hub. The latter can extend from three diameters up to ten or twenty diameters behind the turbine and shows increased turbulence intensity along with a recovery in the wind speed deficit. The evolution of the velocity profile and turbulent mixing is shown in Fig. 2.2. The velocity deficit is found to be strongly dependent on the rotor thrust [11] since it is a direct result of the retardation induced in the wind flow by the turbine. It in turn causes a shear layer to develop at the boundaries of the wake. This acts as a source of turbulence, leading to the mixing of the internal and external flow. Consequently, momentum is drawn in from the free-stream and the velocity begins to recover. The nacelle, tower, atmosphere and the breaking of the tip vortices- which are inherently unstable- act as additional sources of turbulence and aid in the recovery process.

One of the distinctive features of a wind turbine wake is the meandering effect [5]. It is defined as the stochastic variation in the instantaneous center of the wake. While the source of meandering is a subject of active research, it has been attributed to large-scale eddies in the atmospheric boundary layer [12]. An example of a CFD simulation on wind farm is shown in Fig. 2.3 demonstrating some of the phenomena discussed here.

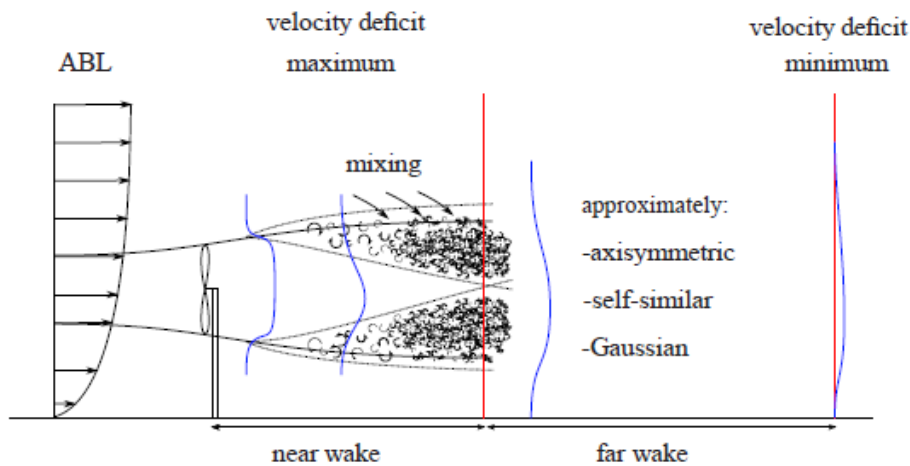


Figure 2.2: Evolution of the velocity profile in the wake- from Figure 6 pg 14. of *Aerodynamics of Wind Turbine Wakes* by B. Sanderse[13]

Due to the economic constraints on land purchasing, wind turbines in a farm cannot be placed at a distance of more than ten diameters from each other [12]. Simultaneously, the velocity deficit in the near-wake is too severe to allow adequate power generation. Thus, wind turbines in a farm are usually present in the far-wake of their upstream counterparts. Despite the recovery of the deficit, the velocity incident on the waked turbines is lower than its free-stream value. Consequently, the power output of the waked turbines is reduced. Due to the wake-generated turbulence, downstream turbines also suffer from significant fluctuations in loads. This high frequency cycling causes fatigue damage. Often, added turbulence intensity of the wake is the biggest determinant of the fatigue life of a wind turbine [14]. Hence, modelling the aerodynamics of wind turbine wakes and accurately capturing its effect on loads and performance is of crucial relevance to the wind industry.

2.2. Numerical modelling of wind turbine wakes

This section describes the methods used in modelling the fluid flow around wind turbines while providing their benefits and limitations.

2.2.1. Computational Fluid Dynamics (CFD)

The basic principle of Computational Fluid Dynamics is solving the Navier-Stokes equations, shown below, on a discretized grid for an incompressible, Newtonian fluid.

$$\begin{aligned} \frac{\partial(\rho u_i)}{\partial x_i} &= 0 \\ \frac{\partial(\rho u_i)}{\partial t} + u_j \frac{\partial(\rho u_i)}{\partial x_j} &= -\frac{\partial p}{\partial x_i} + \mu \frac{\partial^2 u_i}{\partial x_j \partial x_j} \end{aligned} \quad (2.1)$$

These equations are based on the assumption of a continuum and the conservation of mass and momentum. Most implementations use the Finite Volume Method (FVM) wherein the velocity and pressure field are integrated over the control volume surfaces. The resulting discretized equations are then solved using an appropriate numerical scheme. The detailed numerics are not provided here but are well documented in [7]. FVM offers the advantage that it can handle many different mesh structures. Furthermore, using implicit or explicit schemes, the time derivative can be resolved to obtain the temporal evolution of the flow field. The turbulence can be handled in number of ways either by directly resolving up to the smallest scales or by using a model. This forms the subject of the next section.

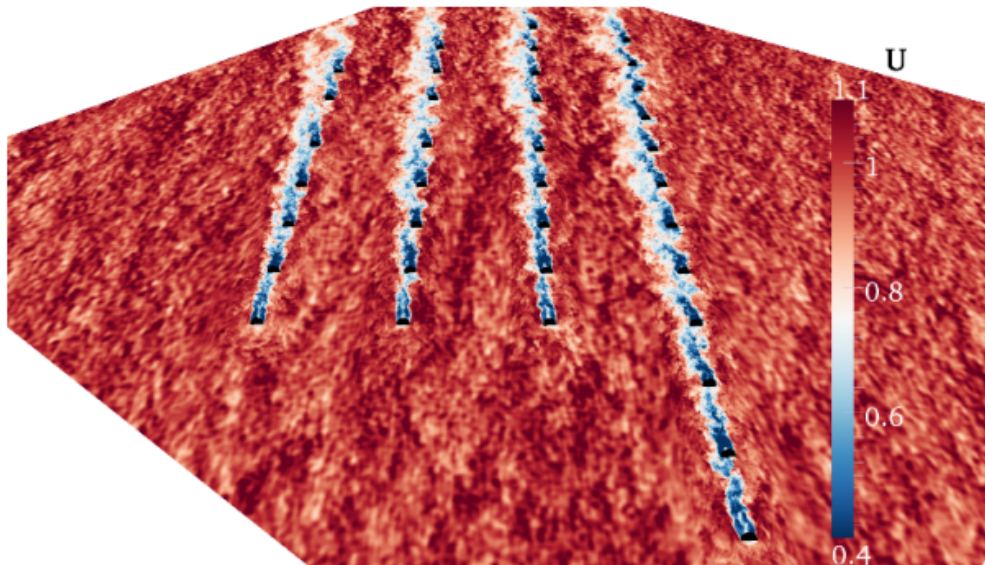


Figure 2.3: A Large Eddy Simulation of a wind farm showing the instantaneous stream-wise velocity contours- from Figure 2a pg. 7 of *A Comparison of the Dynamic Wake Meandering Model, Large-Eddy Simulation, and Field Data at the Egmond aan Zee Offshore Wind Plant* by M.Churchfield et al.[15]

CFD can in theory solve any fluid problem while accurately representing the physics involved. But its limitation lies in the large amount of computational resources required to obtain a solution in a feasible amount of time. The requirements are severe enough to necessitate the usage of a High Performance Computing (HPC) cluster.

2.2.2. Engineering models

The models used in the design and validation of wind turbines which do not capture all the physics of the wake but represent only the most relevant phenomenon are bundled together under the term of Engineering Models. Some use statistics to emulate the stochastic nature of turbulence [16, 17], while others achieve higher fidelity by resolving only the essential physical details of the flow- such as the wake meandering effect [18]. The latter in particular is used in conjunction with Blade Element and Momentum theory (BEM)

for simulating a number of design load cases in the industry. In addition, Free Vortex Methods are another class of models frequently used for wind farm optimization [19]

The advantage of these methods lies in their low computational cost. Unlike CFD, most engineering models can be run in a matter of seconds to minutes, without the need for a HPC cluster. Thus, they are suited for optimization of wind turbine design.

A visual comparison of numerical models used in wind turbine wake analysis is shown in Fig. 2.4. Since the aim of this project is to investigate wind turbine wakes while capturing most of the physical details, CFD is the preferred tool.

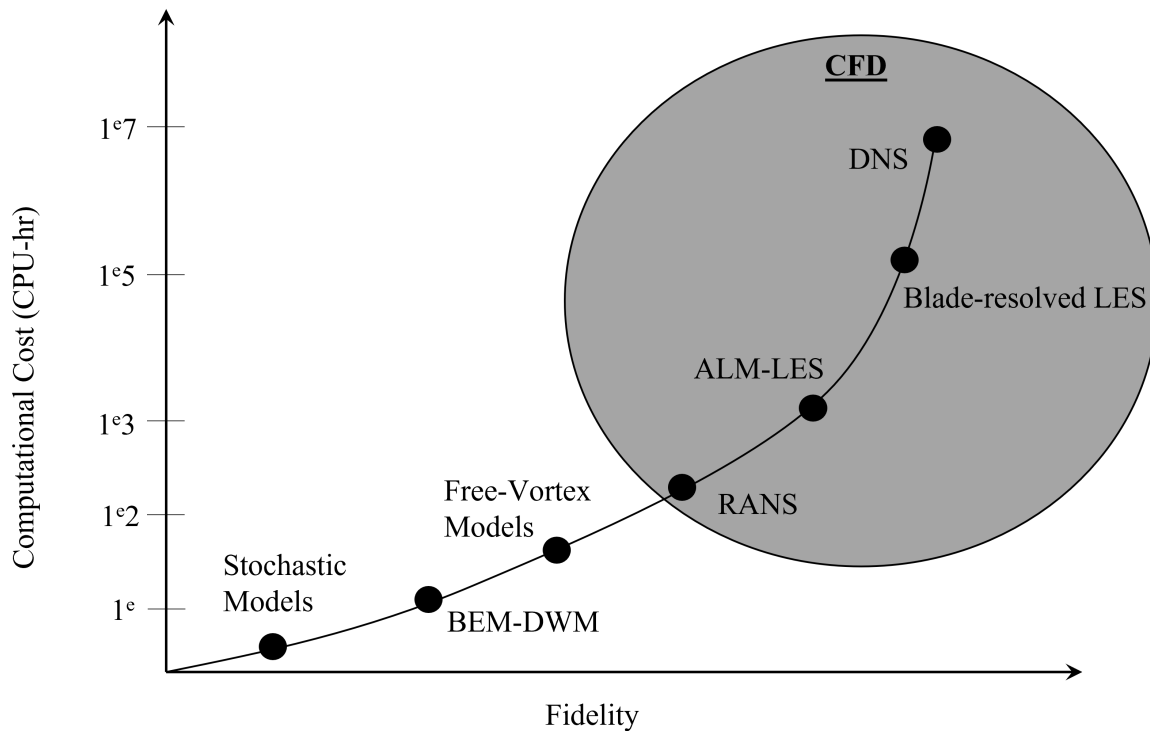


Figure 2.4: Ranking numerical methods in terms of computational cost (measured in CPU-hrs) and fidelity for the simulation of a single wind turbine wake

2.3. Computational Fluid Dynamics

Even within CFD, there are trade-offs between fidelity and computational expense, resulting in a number of different methodologies- as seen in Fig. 2.4. These are differentiated in the manner in which turbulence is handled.

2.3.1. Direct Numerical Simulations (DNS)

In DNS, the Navier-Stokes equations are solved directly without the use of any turbulence model [7]. This requires the resolution of the whole range of spatial and temporal scales. Spatially, the mesh would have to resolve all the scales starting from the integral length scale to the Kolmogorov scale. Even for problems with a small domain size, this would result in a very large mesh. Additionally, the solution time-step is limited by the Courant-Friedrichs-Lewy (CFL) condition [20]. These limitations result in the total number of operations required for a DNS simulation to scale with Re^3 , where Re is the Reynolds number of the flow.

For wind turbine applications, where the Reynolds number is often in the order of 10-100 million, the requirements would exceed the capacity of even the most powerful supercomputers. Thus, DNS simulations are not practical and are currently only used for cases where $Re \approx O(10000)$.

2.3.2. Reynolds Average Navier-Stokes (RANS)

In this method, the Navier-Stokes equations are averaged in time such that the resulting system of equations solves for the mean flow field while the turbulent fluctuations are completely modelled. The Reynolds decomposition forms the basis of this method:

$$u = \langle U \rangle + u', \quad (2.2)$$

where, the time-averaged field is given by:

$$\langle U \rangle = \frac{1}{T} \int_0^T u(t) dt. \quad (2.3)$$

This results in the RANS equations:

$$\frac{\partial \langle U_i \rangle}{\partial t} + \langle U_j \rangle \frac{\partial \langle U_i \rangle}{\partial x_j} = -\frac{\partial \langle P \rangle}{\partial x_i} + 2 \frac{\partial (\nu \langle S_{ij} \rangle)}{\partial x_j} - \frac{\partial (\langle u'_j u'_i \rangle)}{\partial x_j}, \quad (2.4)$$

where S_{ij} is mean strain rate:

$$\langle S_{ij} \rangle = \frac{1}{2} \left(\frac{\partial \langle U_i \rangle}{\partial x_j} + \frac{\partial \langle U_j \rangle}{\partial x_i} \right). \quad (2.5)$$

The last term in Eq. (2.4) is a result of the averaging operation and represents the stresses imposed by turbulence on the mean flow. Since there is no additional relation for the turbulent fluctuations, the system of equations cannot be solved. This is the turbulence closure problem [7] which is addressed using a turbulence model [21].

A modification of the RANS method known as Unsteady Reynolds Average Navier Stokes (URANS) is used to obtain the time evolution of the mean field in applications where a steady state solution is never reached [22]. RANS and URANS are widely used in the industry as the mesh requirements are not too severe and the computational cost is low. Despite their lower fidelity, valuable insights can be obtained about commonly encountered fluid flow problems.

2.3.3. Large Eddy Simulation (LES)

LES applies a spatial filter on the NS equations such that all the scales larger than the filter are resolved while the ones below are modelled using a Sub-grid scale model (SGM). This increases the size of the smallest mesh element hence reducing the computational cost as compared to DNS. Additionally, unlike RANS, it can provide an instantaneous solution and the time-evolution of the flow field while resolving important features of the flow. Thus, LES gives a trade-off between the high fidelity of DNS and the low computational requirements of RANS.

Fig. 2.5 shows the same fluid problem of a high speed jet, solved by different CFD methodologies. The effect of physical resolution and turbulence modelling are clearly seen in the level of detail in the solutions. DNS is able to resolve even the minute turbulent structures while RANS only captures the macroscopic information. Given the trade-off achieved by LES along with the possibility of further reduction in computational cost (by means of the Actuator Line Method), it is the approach used in this project and will be explained in detail in the next section.

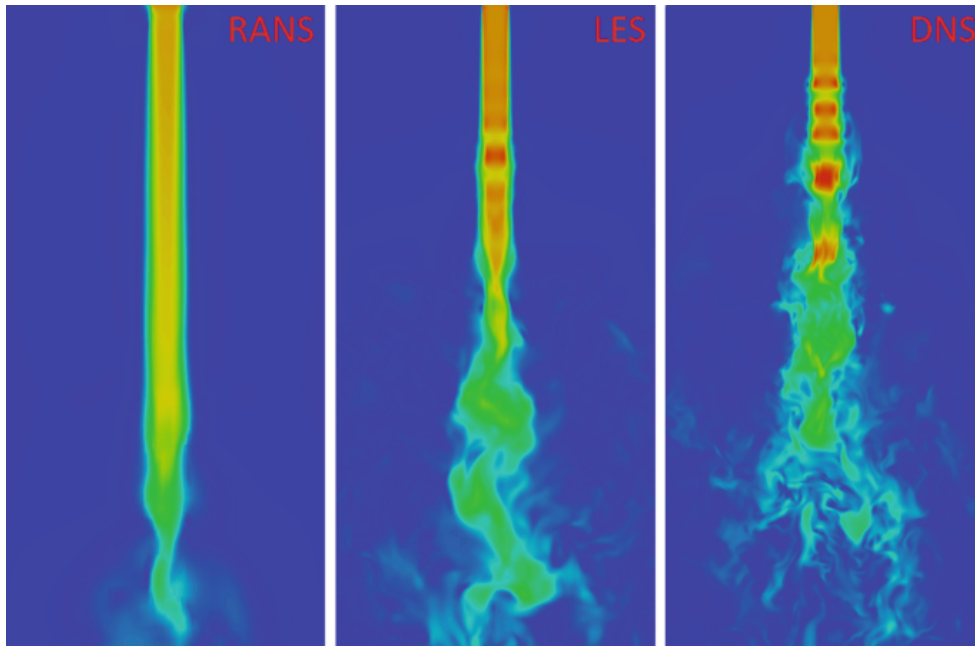


Figure 2.5: Level of fidelity achieved by different CFD methodologies when applied to the same fluid problem: high-speed jet flow- from Figure 5.4 pg 199 of *Applied Computational Fluid Dynamics and Turbulence Modelling* by S.Rodriguez [7]

2.4. Large Eddy Simulation

A Large Eddy Simulation is constructed by applying a filter function, G , on the Navier Stokes equations. The convolutional filter is applied either in the temporal and spatial directions. The operation of the filtered function can be defined as:

$$\overline{\phi(\mathbf{x}, t)} = \int_{-\infty}^{\infty} \int_{-\infty}^{\infty} \phi(\mathbf{r}, \tau) G(\mathbf{x} - \mathbf{r}, t - \tau) d\tau d\mathbf{r}, \quad (2.6)$$

where ϕ is a dummy field and $\overline{\phi}$ is its filtered counterpart. It can also be expressed as a convolution operation:

$$\overline{\phi} = G \star \phi \quad (2.7)$$

And G must be normalized such that:

$$\int_{\mathbb{R}^3} G_{\Delta}(x) dx = 1 \quad (2.8)$$

where Δ is the filter size. Additionally, a Reynolds decomposition can be applied to the field, separating into its filtered and unfiltered (or sub-grid) parts:

$$\phi = \overline{\phi} + \phi'. \quad (2.9)$$

Thus, the filtered Navier-Stokes equations are:

$$\frac{\partial \overline{u}_i}{\partial x_i} = 0, \quad (2.10)$$

$$\frac{\partial \overline{u}_j}{\partial t} + \frac{\partial \overline{u}_i \overline{u}_j}{\partial x_i} = \nu \frac{\partial^2 \overline{u}_j}{\partial x_i \partial x_i} + \frac{1}{\rho} \frac{\partial}{\partial x_i} \underbrace{\tau_{ij}^R}_{(1)} - \frac{1}{\rho} \frac{\partial \overline{P}}{\partial x_j} + \overline{f}_j. \quad (2.11)$$

Here, the term (1) represents the residual stress tensor. It is the stress imposed by the unresolved turbulent scales on the rest of the flow and can be further decomposed as:

$$\tau_{ij}^R = -\rho(\overline{u_i u_j} - \overline{u_i} \overline{u_j} + \overline{u_i u_j'} + \overline{u_i' u_j} - \overline{u_i'} \overline{u_j'} - \overline{u_i' u_j'} + \overline{u_i' u_j'} - \overline{u_i' u_j'}). \quad (2.12)$$

An overview of the significance of each term can be found in [7]. A Sub-grid scale model is used to compute them and close the filtered momentum equation. These models are divided into two main types: [23]: functional models and structural models. Functional models use the Boussinesq hypothesis to express the residual stress tensor in terms of a turbulent eddy viscosity. On the other hand, structural models evaluate the residual stress based on approximations of the filtered velocity field. Functional models have been found to be more stable around complex geometries like wind turbine nacelles and towers [24].

Further, it has been shown that for wind turbine wake simulations when using the Actuator Line Method with a sufficiently resolved mesh and proper choice of the mollification kernel (Fig. 2.12), the type of sub-grid scale model used is not crucial [25]. This is also illustrated in Fig. 2.6. Thus, preference is given to that model which has lower computational demands. This condition is fulfilled by the Smagorinsky model [26]. Herewith its mathematical description.

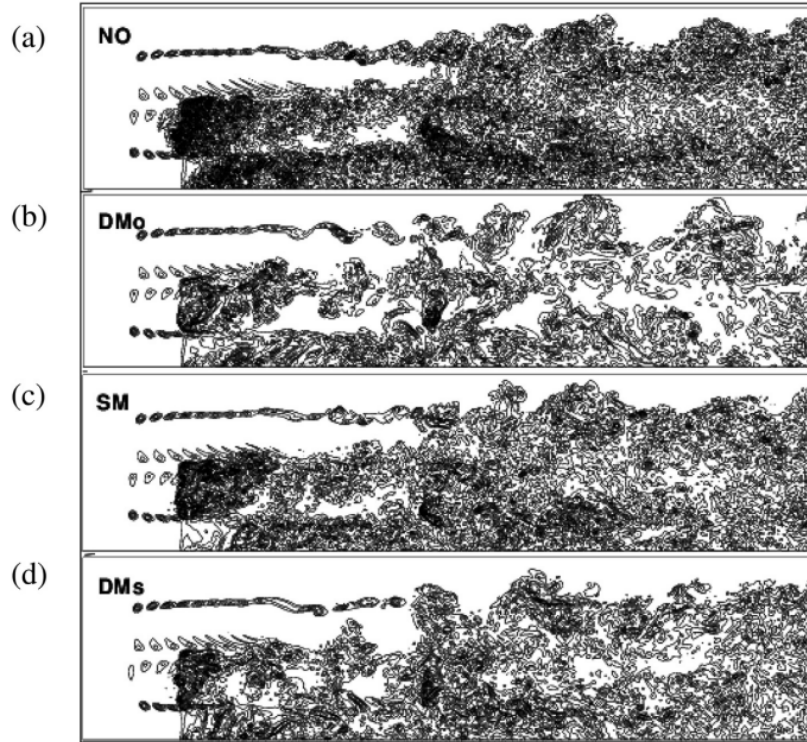


Figure 2.6: Snapshots of iso-vorticity in the whole domain for different sub-grid models. NO stands for no sub-grid model, DMo for Dynamic Mix - ω model, DS for Dynamic Smagorinsky model and DMs for Dynamic Mix-S model. All four predict the destabilization of the vortices equally well but in the NO model due to a lack of dissipative terms, smaller eddies are seen - from Figure 14 page 396 of *Role of subgrid-scale modeling in large eddy simulation of wind turbine wake interactions* by H.Sarlak et al.[25]

Using the Boussinesq eddy viscosity assumption [27], the residual stress tensor is expressed as:

$$\tau_{ij}^R = \rho \nu_t \left(\frac{\partial \bar{u}_i}{\partial x_j} + \frac{\partial \bar{u}_j}{\partial x_i} \right). \quad (2.13)$$

Now, the problem is reduced to only modelling the turbulent kinematic viscosity ν_t . In the classical Smagorinsky model [28], the turbulent viscosity is given by:

$$\nu_t = (C_s \Delta)^2 \bar{S}, \quad (2.14)$$

and,

$$\bar{S} = \sqrt{2S_{ij}S_{ij}}. \quad (2.15)$$

Where C_s is the Smagorinsky constant and $\overline{S_{ij}}$ is the strain rate:

$$\overline{S_{ij}} = \frac{1}{2} \left(\frac{\partial \overline{u}_i}{\partial x_j} + \frac{\partial \overline{u}_j}{\partial x_i} \right). \quad (2.16)$$

But this model suffers from the drawback that the near wall stresses are not captured well. Thus, an improvement was proposed wherein C_s is not constant over the entire grid but is locally determined. The resulting dynamic model provides better treatment of steep stress gradients [26]. It has another advantage that in the presence of inflow turbulence, C_s does not affect the wake development [29].

2.5. YALES2

YALES2 [9], a library of LES and DNS solvers was developed by CORIA Lab (a unit within the university of Normandy) for two-phase combustion problems on unstructured meshes to be solved on massively parallel clusters. The LES framework was extended to solve low-Mach number flows of constant and variable densities. Herewith follows a brief discussion of the manner in which some of the challenges of a wind turbine wake LES are handled in YALES2.

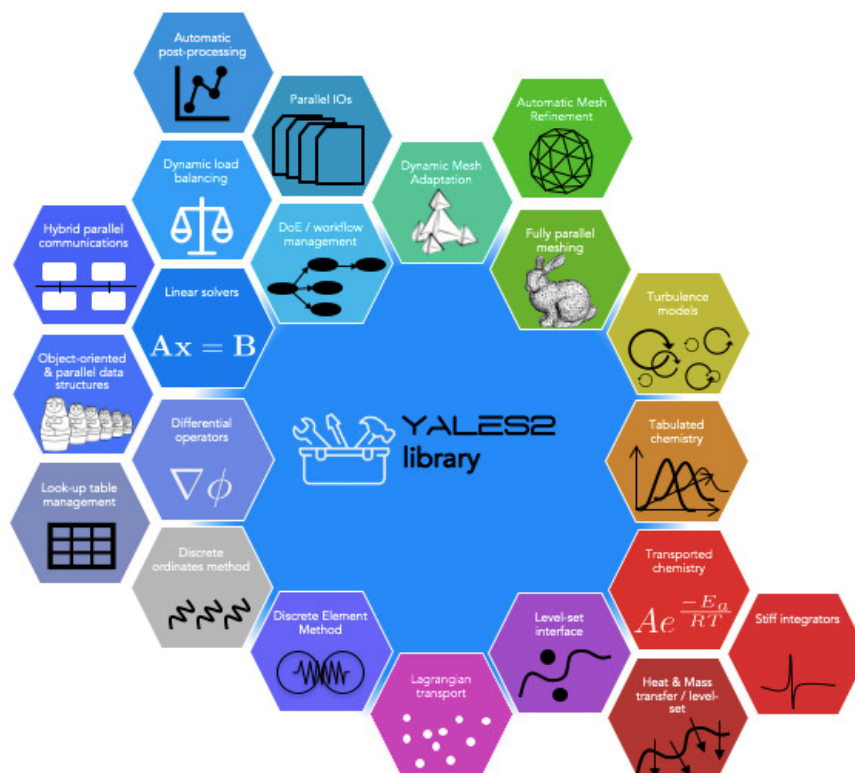


Figure 2.7: An overview of the features of YALES2 - taken from the YALES2 public wiki [30]

As alluded to before, one of the main challenges of a CFD simulation is its computational cost. In order to obtain a solution in a feasible amount of time, the problem must be solved in parallel over a cluster of computers. This often requires the re-formalization of the problem to ensure proper communication between the different nodes in the cluster. Message Passing Interface (MPI) [31] addresses this issue by synchronizing the activities of the nodes. However, this is not a complete solution. If the mesh is not optimally distributed in terms of memory requirements, then the parallelization will be ineffective. In this regard, YALES2 uses METIS [32] and double domain decomposition (DDD) as means of achieving optimal computational performance (refer Fig. 2.8).

Generation of a mesh that resolves the required scales of the flow while also being within the memory limits is another challenge that needs to be addressed. Around complex geometries like wind turbine nacelles, only unstructured meshes are possible. YALES2 allows for generation of tet-based meshes with

scope for adaptive refinement. To this end, external libraries like MMG [33] can be called to improve the quality of pre-generated meshes.

When solving time-dependent flow phenomena using explicit schemes, the CFL condition must also be satisfied [20]:

$$C = \frac{u\Delta t}{\Delta x} < 1, \quad (2.17)$$

where u is the flow velocity, Δt is the time-step and Δx is the smallest grid size. It means that over one time-step, a fluid particle must not travel a distance of more than one cell. Such a criteria ensures the numerical stability of the solution. Now, in the case of a wind turbine simulation with a resolved blade, the grid size will be very small to capture the blade tip geometry. Thus, to keep C less than 1, the time-step will have to be reduced. Now, if the wake has to be studied, then the solution must be run for a large amount of physical time to allow all upstream flow information to be convected at least once through the computational domain. The domain itself can be as long as a few kilometers in case of a wind farm. Thus, the wall-clock time of such a simulation would be prohibitively large. Hence, in YALES2 and other CFD libraries, the turbine is not resolved but modelled using an actuator disk or line. These methodologies are explained in detail in the next section.

Other smaller but significant challenges include interface tracking for two-phase flows, dynamic load balancing and high-order filtering which are not pertinent to this project but are well addressed in YALES2. For a deeper dive in YALES2 and its capabilities please refer [9, 34, 35, 30, 36]

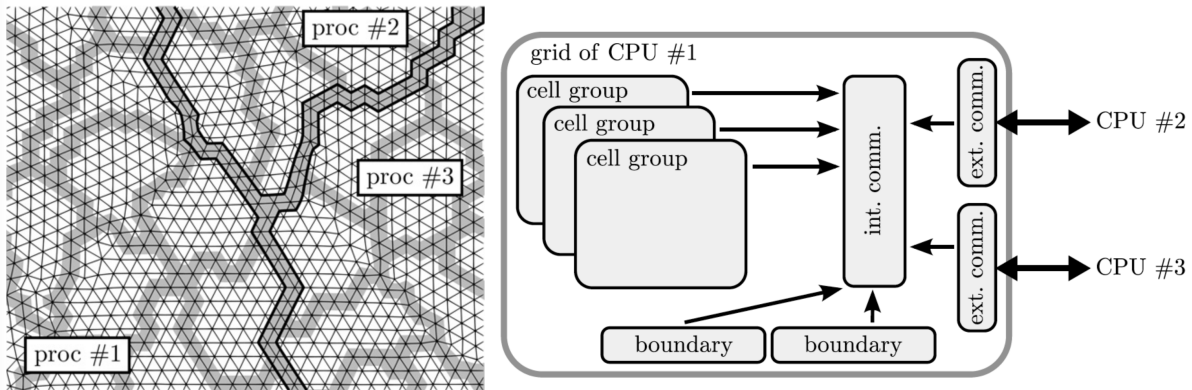


Figure 2.8: Depiction of Double Domain Decomposition (left). Cells are divided once between processors and again for preconditioning as shown by the light grey highlights. The cells within the black outline facilitate communication between processors. The communication schematic is shown on them right- from *Figure 3 and 4, pg. 144 of Design of a massively parallel CFD code for complex geometries by V.Moureau, P.Domingo and L.Vervisch [9]*

2.5.1. Incompressible Constant Density Solver (ICS)

Before presenting the numerical details of the solver, it is important to mention that a 4th order scheme is used for spatial and temporal integration. For the latter the TFV4A scheme is used [37]. ICS is the method of choice for open-field wind turbine simulations and 3D jets where the Mach number is low and density fluctuations are insignificant. First, the solution method developed by Chorin is explained. Then, the YALES2 prediction-correction implementation is presented. Lastly, the numerical linear algebra involved in solving the Poisson equation is touched upon.

The method developed by Chorin [38] uses the Hemholtz-Hodge decomposition and considers a hypothetical field u such that:

$$u = u_{\text{sol}} + u_{\text{irrot}} = u_{\text{sol}} + \nabla\phi. \quad (2.18)$$

Where u_{sol} is a divergence-free field and the required solution of the Navier-Stokes equations- by virtue of the incompressibility condition. Further, taking the divergence of u gives a Poisson equation:

$$\nabla \cdot u = \nabla^2\phi. \quad (2.19)$$

The solution procedure is as follows: once u is known, the scalar field ϕ can be obtained and then, the divergence-free field is given by:

$$u_{\text{sol}} = u - \nabla\phi. \quad (2.20)$$

Now, in the method of Chorin, first an intermediate field u^* is computed by solving the following equation:

$$\frac{u^* - u^n}{\Delta t} = -(u^n \cdot \nabla) u^n + \nu \nabla^2 u^n. \quad (2.21)$$

Where u^n is velocity at the n th time step. This is the prediction step of the algorithm. But, as the pressure gradient term is ignored, u^* is not the required field. In the correction step, the pressure gradient is added to yield the velocity field at the next time step:

$$u^{n+1} = u^* - \frac{\Delta t}{\rho} \nabla p^{n+1}. \quad (2.22)$$

Since the pressure field itself is not available, it must be computed by the Poisson equation where u^* corresponds to u in Eq. (2.19):

$$\nabla^2 p^{n+1} = \frac{\rho}{\Delta t} \nabla \cdot u^*. \quad (2.23)$$

It should be noted that the pressure term and all other scalars are computed on a staggered time-step. Thus, the equation can be corrected to:

$$\nabla^2 p^{n+1/2} = \frac{\rho}{\Delta t} \nabla \cdot u^*. \quad (2.24)$$

The same is true for the correction equation. Additionally, in YALES2, the pressure in the $n - 1/2$ time step is also used in the prediction-correction steps. This yields a better prediction of u^* and helps reduce numerical errors. Thus, the modified prediction equation is:

$$\frac{u^* - u^n}{\Delta t} = -(u^n \cdot \nabla) u^n + \nu \nabla^2 u^n - \frac{\Delta t}{\rho} \nabla p^{n-1/2}, \quad (2.25)$$

and correspondingly the correction step becomes:

$$\frac{u^{n+1} - u^*}{\Delta t} = -\frac{1}{\rho} \nabla (p^{n+1/2} - p^{n-1/2}). \quad (2.26)$$

Lastly, the following Poisson equation is solved in YALES2:

$$\nabla^2 (p^{n+1/2} - p^{n-1/2}) = \frac{\rho}{\Delta t} \nabla \cdot u^*. \quad (2.27)$$

Solving the Poisson equation is extremely costly since it requires the pressure values to be evaluated at every node, for every time-step. In case of ICS, it is the most computationally expensive step. Further, the Laplacian operator (∇^2) is a symmetric singular matrix, requiring the linear system of Eq. (2.27) to be solved iteratively using PCG or BICGSTAB [39]. Often, the system is ill-conditioned [40], resulting in a large number of iterations before convergence is achieved. Therefore, preconditioned methods have been implemented in YALES2, in conjunction with DDD.

2.6. Turbine modelling

LES of a completely resolved wind turbine is not computationally feasible given that the range of scales is still too large [6]. Thus, a number of models have been developed to simulate the behaviour of a wind turbine without capturing its geometry. In this section, the relevant models will be discussed after which the Actuator Line Method, will be explained in depth. Lastly, some important studies concerning the usage and development of ALM will be elaborated.

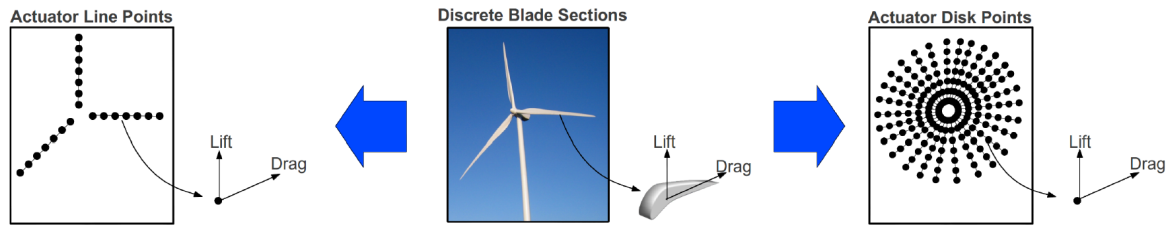


Figure 2.9: Geometrical modelling involved in the Actuator Disk and Actuator line models- from Figure 1 pg 3 of *A Comparison of Actuator Disk and Actuator Line Wind Turbine Models and Best Practices for Their Use* by L.Martínez et al.[41]

2.6.1. Methodologies

Wind turbine models also differ in terms of their fidelity and computational requirements. Of the lowest fidelity and thus minimal computational needs are models such as BEM and VM (Vortex Method). The latter is based on Prandtl's lifting line theory [42] and computes the induced velocities from the circulation around the wind turbine blade. Here, focus will be directed on actuator methods. These model the wind turbine by inducing body force source terms in the momentum equations. They compute the lift and drag forces from the local velocity field and then project these forces on the fluid mesh. The forces are computed from either the power curve of the turbine or tabulated airfoil data. The different approaches are explained below.

Actuator Disk Method

In this method, the turbine geometry is not resolved and its effect is emulated by a disk of diameter equal to that of the rotor. An average force is computed from the flow field and the turbine operating point. The forces are then mapped over annular rings, while attempting to replicate the force distribution over the actual blades. A detailed mathematical treatment of this method can be found at [43]. Corrections can also be included for tip loss and dynamic effects. Sørensen et al. [44] found correspondence between experimental data and unsteady loads predicted by ADM. Further, a rotating actuator disk model was observed to improve the prediction of turbine power under unsteady conditions [45]. But a thorough comparison of the actuator disk with the actuator line [41] found that while development of the far wake and power production are well predicted by both the methods, the actuator disk cannot induce tip and root vortices in the wake. Thus, if the near wake structure is to be studied, then the actuator disk model is not a viable option.

Actuator Line Method

Here, the low-level geometry of the turbine is captured by representing the blade as a line [44]. It is further discretized into sections where the local velocity and inflow angle are used to compute the lift and drag forces from the tabulated airfoil data. A better geometrical representation of the turbine results in a higher level of fidelity in the wake where tip and root vortices can be observed. Indeed, the Actuator Line Method can well approximate the turbine power curve while emulating the helical tip vortices, as shown in Fig. 2.11 and Fig. 2.10. Thus, this method has become the industry standard for LES of wind turbines wakes.

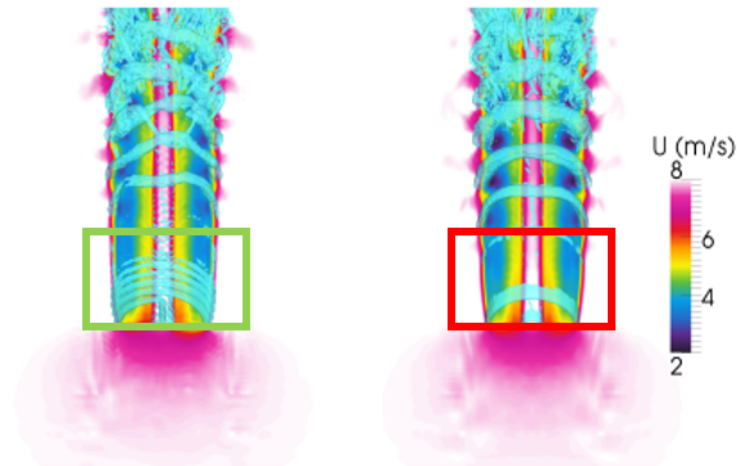


Figure 2.10: Comparison of the streamwise velocity contours on the isosurface of the second-invariant of velocity gradient tensor as computed with the Actuator Line (left) and Actuator Disk Method (right). The difference in the near wake is visible wherein the Actuator Line Method produces the helical vortices- from Figure 2 pg 3 of *A Comparison of Actuator Disk and Actuator Line Wind Turbine Models and Best Practices for Their Use* by L.Martínez et al.[41]

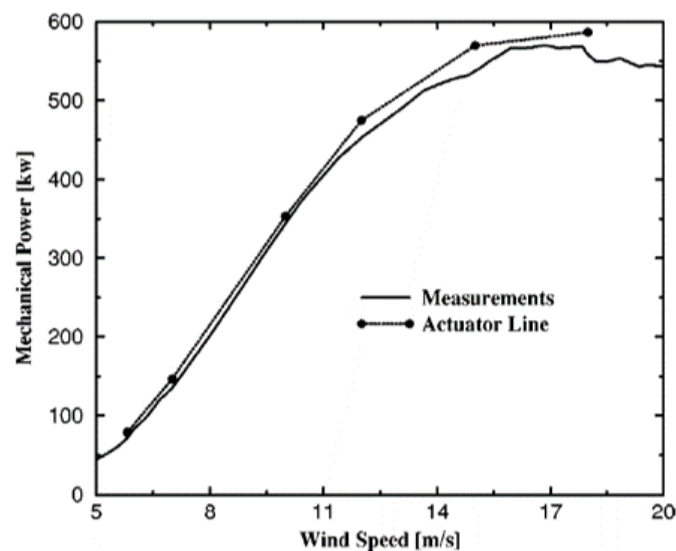


Figure 2.11: A comparison of the measured power curve of the Nordtank 500/41 wind turbine with its Actuator Line Model- from Figure 4 pg. 397 of *Numerical Modeling of Wind Turbine Wakes* by J. Sørensen et al. [8]

Actuator Sector Method

The Actuator Sector Method goes a level deeper in terms of fidelity by representing the turbine as an actuator surface defined by the blade length and chord [46]. The sector is mapped onto the mesh which is of area equal to that covered by the blade element in one time-step. Thus, the force distribution is closer to that achieved by a blade-resolved simulation. This results in better treatment of near-wake vortices but the computational cost is higher than that of ALM [47]. Additionally, force projection requires extra attention introducing another level of complexity.

Given the high-fidelity achieved by the Actuator Line method, its relatively simple implementation and scope for computational optimization, it is the preferred method for modelling wind turbines in this project.

2.6.2. Actuator Line Method

Herewith follows a step-wise description of the Actuator Line Method, part of which is also illustrated in Fig. 2.12:

Step 1: Blade discretization

The blade is divided into a number of sections, each representing an airfoil of chord c and width w . These quantities along with the airfoil properties depend on the geometry of the actual blade. The orientation of the chord and thickness axes, e_c and e_t , which depend on the section twist and blade deformation, is also considered as it affects the local inflow angle.

The number of sections or elements should be carefully determined. If the blade discretization is coarser than the surrounding mesh, there will be discontinuities in the projected forces. This will lead to a divergence of the solution. Thus, it must follow the relation:

$$N > L_{blade}/h_{max}, \quad (2.28)$$

where N is the number of sections of the actuator line, L_{blade} is the length of the blade and h_{max} is the maximum grid size in the vicinity of the blade.

Step 2: Velocity evaluation

In order to compute the lift and drag forces at each section of the discretized blade, the local velocity is required. This can be determined from the section blade velocity u_{blade} and the local gas velocity u_{gas} . The former depends on the angular velocity of the rotor, θ , and the blade deformation (if an elastic blade is considered as in Subsection 2.7.2). The latter is interpolated from the fluid mesh after correcting for the inflow angle corresponding to that section of the blade. In case the gas velocity is directly projected and its span-wise contribution is ignored, then the relative velocity at the i -th section, $u_{rel,i}$, is given by:

$$u_{rel,i} = u_{gas,i} - u_{blade,i}. \quad (2.29)$$

The evaluation of u_{blade} is complicated by the effect of blade deformation and control. It is no longer equal to the product of the section radius and θ . Instead, in YALES2, it is calculated from the following relation:

$$u_{blade,i} = \frac{dx_i}{dt} \simeq \frac{x_i^* - x_i^n}{\tau} = u_{blade,i}^{n,*}, \quad (2.30)$$

where x_i^n is the initial position of the blade, τ is the reduced time step such that $\tau = \frac{\Delta t}{a}$ while $a \geq 1$ and x_i^* is the blade position after τ . The value of a is selected such that the error between the approximate velocity $u_{blade,i}$ and the instantaneous blade velocity $u_{blade,i}^{n,*}$ is minimized. In YALES2, a is set to 100. x_i^* is predicted from the control imposed on the blade as well as the deformation (which can be obtained from a structural solver).

The local gas velocity is interpolated from the surrounding mesh using a linear scheme. Then, the relative velocity at the section is finally given by:

$$u_{rel,i} = (u_{gas,i} \cdot e_c - u_{blade,i} \cdot e_c) e_c + (u_{gas,i} \cdot e_t - u_{blade,i} \cdot e_t) e_t. \quad (2.31)$$

Step 3: Force computation

The lift and drag forces are computed by first determining the angle of attack:

$$\alpha_i = \text{atan}(u_{rel,i} \cdot e_t, -u_{rel,i} \cdot e_c), \quad (2.32)$$

and the chord based Reynolds number:

$$Re = \frac{\|u_{rel}\| c}{\nu}. \quad (2.33)$$

Then the lift and drag coefficients can be obtained from the airfoil properties. The following relation is used for the 2D force on the section:

$$F_{2D,i} = \frac{1}{2} \rho \|u_{rel,i}\|^2 c (C_L(\alpha_i) e_L + C_D(\alpha_i) e_D). \quad (2.34)$$

Additionally, in YALES2, the induced moment on the section is also calculated as follows:

$$M_{x_i} = \frac{1}{2} \rho \|u_{rel,i}\|^2 w c^2 C_M(\alpha_i) e_s. \quad (2.35)$$

The equations presented above do not take into account the 3D aerodynamic effects or the unsteady behaviour of the air flow. Thus, a number of corrections have been implemented in YALES2 to account for tip loss, dynamic stall and 3D stall delay.

Step 4: Blade displacement

Before projecting the forces on the fluid mesh, the blade is displaced to its final position at the end of the time-step. In YALES2, the force-projection is implemented based on the element reference frame. Thus, force-projection must occur after blade displacement to account for the new element orientation.

Step 5: Force mollification

In the final step, the forces are projected as body source terms in the fluid mesh. In order to prevent any singularities in the momentum equations, the projection must be regularized by a mollification kernel. The mollified force is obtained by the following convolution:

$$F_{\epsilon,i} = F_i * \eta_{\epsilon}, \quad (2.36)$$

where η_{ϵ} is the mollification kernel and is expressed as:

$$\eta_{\epsilon}(d) = \frac{1}{\epsilon^3 \pi^{3/2}} \exp[-(d/\epsilon)^2], \quad (2.37)$$

while ϵ is the mollifier width and d is distance between a grid point and the actuator element. ϵ must be selected such that the ϵ/h ratio is normalized over the entire grid. This ensures that the projected forces are conservative. In YALES2, ϵ/h is set to 2. The body force source term in the momentum equations is then obtained as follows:

$$f(x) = -\frac{1}{\rho} \sum_{i=1}^N F_i \eta_{\epsilon}(\|x - x_i\|). \quad (2.38)$$

N is the number of actuator points in the vicinity of the grid node as per the mollifier width. The mollification kernel presented in Eq. (2.37) is isotropic in nature as the forces are projected symmetrically in all directions. This implementation is preferred in YALES2 as the resulting grid resolution requirements are not too severe.

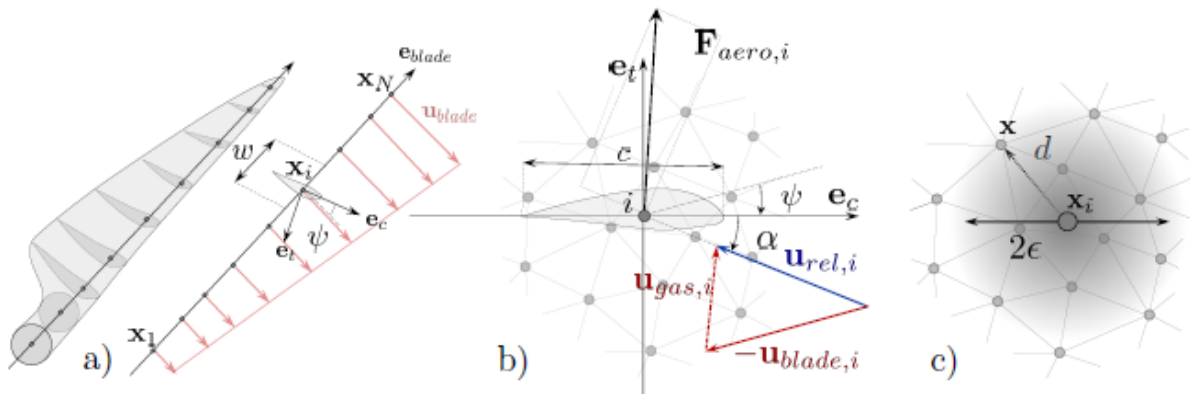


Figure 2.12: Schematic representation of the steps involved in ALM- from Figure 2.9 pg. 38 of *Investigations of yawed offshore wind turbine interactions through aero-servo-elastic Large Eddy Simulations* by F. Houtin-Mongrolle [36]. In a) the discretization of the blade is shown along with the axes orientations of the elements. b) depicts the velocity evaluation as the sum of the local gas and blade velocities. And in c) the force mollification is shown, where the kernel approximates a Gaussian distribution.

2.6.3. Review of ALM-LES studies

In this section, a number of important studies in the domain of ALM-CFD are presented. the discussion is focused towards the developments in ALM and insights garnered about the wake flow properties.

ALM was initially developed by Sørensen and Shen [8] wherein the performance of a single turbine was evaluated and compared with BEM. It was observed that ALM-LES was closer to measurements than BEM. But based on these comparisons, ALM gave an over-prediction of thrust, especially tip loads [24]. Hence subsequent studies aimed at improving either the velocity interpolation or the force mollification to address this problem.

For example, higher order schemes were used for the velocity interpolation [48]. Additionally, an anisotropic mollification kernel was used in this study based on an airfoil shape as seen in Fig. 2.13. It led to a more realistic force distribution on the fluid mesh allowing for better predictions of wake vorticity. In Fig. 2.14 it can be also be observed that the anisotropic kernel produced a more well-resolved wake with finer structures being clearly captured. The level of fidelity is closer to that of blade-resolved simulations. But, the computational costs were high due to the requirement of a more resolved mesh and a smaller time-step needed to meet the CFL condition.

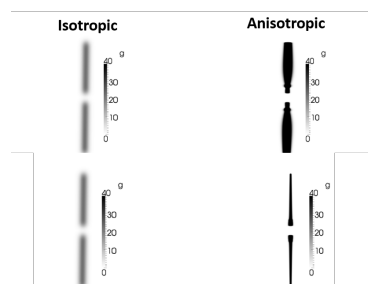


Figure 2.13: The body force projection as viewed from upstream (top row) and the side (bottom row) for the two different mollification kernels. It can be observed that the anisotropic kernel yields a shape similar to the blade profile- *from Figure 1 pg. 5 of An Advanced Actuator Line Method for Wind Energy Applications and Beyond by M. Churchfield et al.[48]*

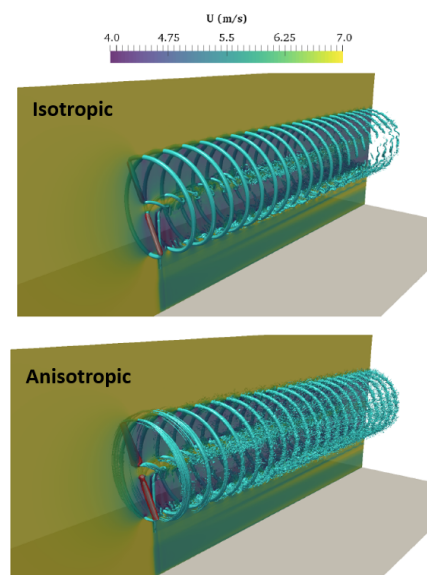


Figure 2.14: Q-criterion isosurfaces showing the difference in the wake structure for the two mollification methods - *from Figure 1 pg. 5 of An Advanced Actuator Line Method for Wind Energy Applications and Beyond by M. Churchfield et al.[48]*

Another approach used a Filtered-Actuator Line model [49] where a correction to the downwash was

applied before computing the sectional lift and drag forces. This allows the mollification kernel width (ϵ) to be larger resulting in a coarser grid. The resulting rotor thrust was closer to measurements of the NREL phase VI turbine while no difference was observed in the flow field generated by ALM and F-ALM (as seen in Fig. 2.15). But while F-ALM was able to reduce the computational cost this method requires further validation for different inflow conditions.

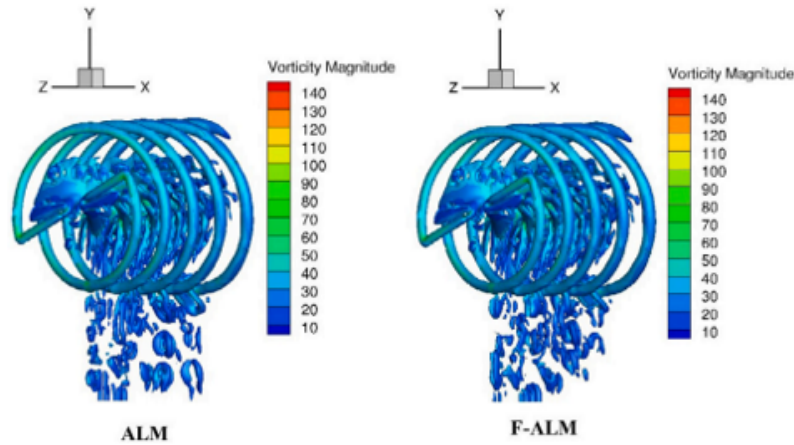


Figure 2.15: Comparison of the vorticity isocontours for the classical (left) and filtered (right) Actuator Line Methods showing similar wake development- *from Figure 12 pg. 10 of Large-Eddy Simulation of a wind turbine using a Filtered Actuator Line Model by R.Stanly et al.[49]*

Initial implementations of ALM did not account for effect of the tower and nacelle. This produced a wake which was unrealistic as it had a distinctive high-speed jet in the center. In a study by Churchfield et al. [50], a simple tower and nacelle model was developed to observe its effect on the wake development. Out of the four models studied, the C_p -based model was found to provide the best agreement with velocity profiles generated in wind tunnel tests. Fig. 2.16 shows the difference in the wake generated with and without a tower-nacelle model. It can be seen that the former produces an asymmetric wake due to the drag force induced by the tower. As expected, no speed-up is seen in the core of the wake as the nacelle produces a velocity deficit. The tower wake interacts with the tip vortices leading to an earlier destabilization of the latter. The authors also conclude that the tower wake influences the meandering in the far downstream region. Although the models do not perform as well as a simulation with a body-fitted mesh, the increased fidelity obtained for a small rise in computation cost means that these models can be included in the simulation setup of this project.

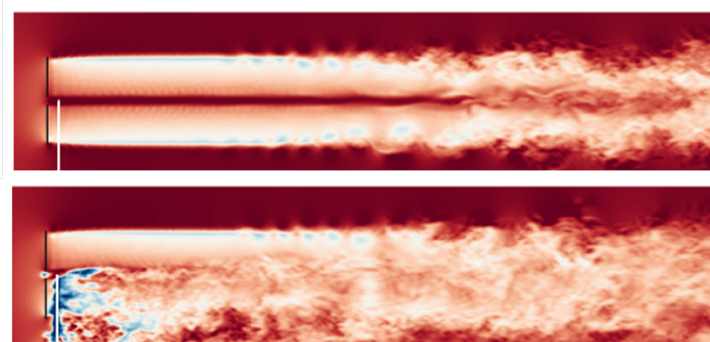


Figure 2.16: Instantaneous stream-wise velocity contours on a plane passing through the turbine center showing the differences between a wake produced with (bottom) and without (top) a tower and nacelle model. Here the only the C_p model is shown -*from Figure 5 pg. 10 of Modeling Wind Turbine Tower and Nacelle Effects within an Actuator Line Model by M. Churchfield et al.[50]*

Ji et al. [51], developed a hybrid Actuator Line Immersed Boundary (AL-IB) methodology. The nacelle of the NTNU B1 turbine was modelled using IB in a method similar to ALM where the nacelle geometry was not resolved but its influence on the flow was delegated to force-source-terms. First, the hybrid model was validated with measurements of mean velocity and turbulent kinetic energy in the wake of the B1 turbine. Next, comparisons of AL and AL-IB were carried out and it was observed that the latter was able to capture the nacelle vortices. While ALM suffered from an unphysical high speed region in the near wake core, AL-IB also captured the interaction between the tip and nacelle vortices which led to a faster breakdown of the tip vortex structure. The authors predict that this may lead to higher instabilities in the aerodynamic loads of a waked turbine.

Volker et al. [52] studied two turbines in alignment and yaw with sheared inflow and no turbulence. Yawing resulted in an increase in the total power production of the tandem system. The influence of surface roughness on wake development was analysed by Castellani et al. [53] where it was seen that a complex terrain led to an asymmetric wake, as seen in Fig. 2.17. The velocity deficit recovered faster in the part of the wake closer to the surface.

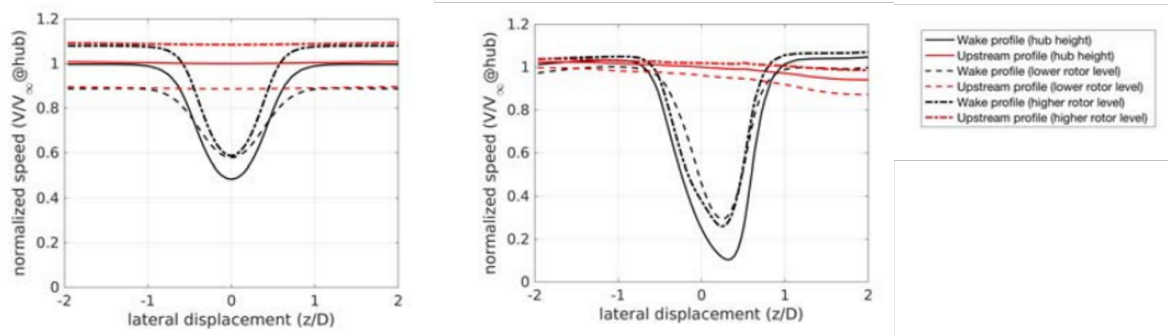


Figure 2.17: The top view of the lateral velocity profile at a distance $2.8D$ downstream. In the flat terrain (left), the wake is symmetric while the complex terrain (right) causes a drift of the computed wake center as well as a much stronger deficit -from page 6 Figure 7 of *CFD three dimensional wake analysis in complex terrain* by F. Castellani et al.[53]

A comparison between DWM, ALM-LES and field data was carried out by Churchfield et al. [15] for the Egmond aan Zee wind farm. Due to the high cost of ALM-LES on a wind farm level, only one case was run. It was found that DWM was not accurate at predicting the blade-root out-of-plane bending moment. The authors suspect that the differences are mainly created by the different inflow used in the LES and DWM cases. The direction of future studies is pointed towards an analysis of the inflow method and the treatment of background turbulence.

This concludes the discussion on standalone ALM-LES. In the next section, the FSI coupling with the structural solver BHawC will be described. This coupling falls in the domain elastic ALM-LES as the blade is no longer rigid.

2.7. BHawC coupling: an elastic ALM-LES implementation

BHawC is an aero-servo-elastic tool developed by Siemens Gamesa Renewable Energy (SGRE) for design and certification of wind turbines [10]. It is similar to other aero-elastic tools such as OpenFAST [54] and HAWC2 [55].

The motivation behind the coupling lies in the necessity to overcome the drawbacks of ALM-LES described in the previous section. By this endeavour, the level of fidelity in the simulation can be further increased with little additional cost. This is because the structural solver has a very low overhead. In this section, the background of BHawC is first provided. It is followed by an overview of the coupling, a more detailed description of which can be found in [36]. The last section is dedicated to a review of elastic ALM studies.

2.7.1. Structural solver

BHawC uses a finite beam element model along with substructure modules for the blades, tower, nacelle and foundation. Two-node Timoshenko beam elements are utilized, with 12 degrees of freedom. The substructures are connected via kinematic couplings. It attempts to achieve the following equilibrium condition:

$$f_{damp}(\Theta_{GB,BH}^{NB}, \dot{x}_s) + f_{int}(x_s, \Theta_{GB,BH}^{NB}) + f_{iner}(x_s, \Theta_{GB,BH}^{NB}, \dot{x}_s, \ddot{x}_s) = f_{ext}(x_s, \Theta_{GB,BH}^{NB}, \dot{x}_s, \ddot{x}_s), \quad (2.39)$$

where f_{ext} is the external force on the structure mainly due to aerodynamic effects and gravity, f_{damp} is the damping force, f_{int} is the internal resistance to elastic deformation and f_{iner} is the force due to inertia. Additionally, x_s is the node position while its derivatives denote the velocity and acceleration. Finally, $\Theta_{GB,BH}^{NB}$ is the node orientation in the coordinate system of BHawC. In standalone BHawC, the aerodynamic forces are provided by an aero-module using BEM. The hydrodynamic and seismic forces are computed by other modules as they also contribute to f_{ext} .

Once the external forces are known, along with element positions and orientations from the previous time step, BHawC attempts to find equilibrium by incrementing the system state and solving the following equation:

$$\mathcal{M}(\Theta_{GB,BH}^{NB}) \delta \ddot{x}_s + \mathcal{C}(\Theta_{GB,BH}^{NB}, \dot{x}_s) \delta \dot{x}_s + \mathcal{K}(x_s, \Theta_{GB,BH}^{NB}, \dot{x}_s, \ddot{x}_s) \delta x_s = \mathcal{R}, \quad (2.40)$$

where \mathcal{M} , \mathcal{C} and \mathcal{K} are mass, damping and stiffness matrices respectively. \mathcal{R} is defined as:

$$\mathcal{R} = f_{ext} - f_{damp} - f_{int} - f_{iner}. \quad (2.41)$$

The Newton-Raphson method is used to solve the system of equations formed by all the elements. Convergence is achieved when \mathcal{R} is 0. For a more detailed treatment of BHawC, kindly refer to [10].

2.7.2. BHawC-YALES2 coupling

The coupling was developed as part of the PhD thesis of F.Houtin-Mongrolle [36] and is presented here in brief. The objective of the coupling was to replace the aerodynamic module of BHawC with YALES2. Thus, YALES2 computes the aerodynamic forces while BHawC provides the deformation of the blades. A loose two-way coupling allows the transfer of forces from YALES2 to BHawC while the deformations are exchanged in the opposite direction.

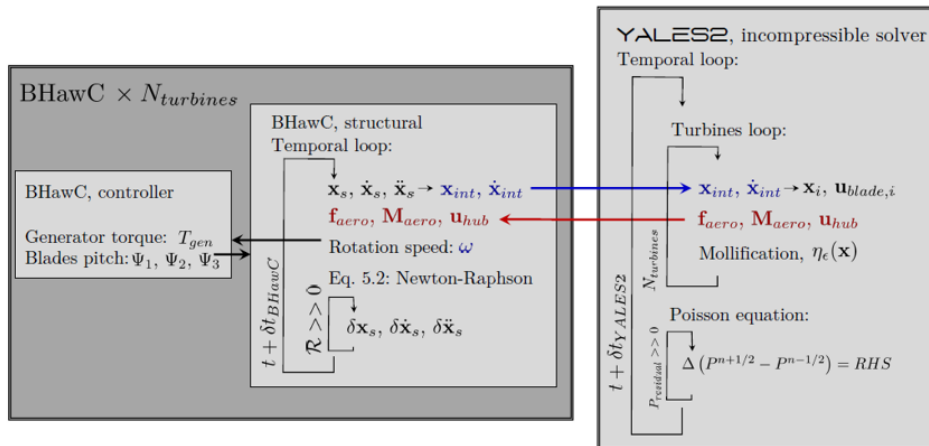


Figure 2.18: YALES2-BHawC coupling strategy - from Figure 5.2 pg. 137 of *Investigations of yawed offshore wind turbine interactions through aero-servo-elastic Large Eddy Simulations* by F. Houtin-Mongrolle [36]. For each temporal loop, force-displacement information is only exchanged once.

The coupling strategy is shown in Fig. 2.18 and follows a Conventional Serial Staggered (CSS) procedure. The communication between YALES2 and BHawC is facilitated by MPI, handling the streams shown by lines red and blue in Fig. 2.18. For each turbine in the domain, one processor is started for

BHawC resulting in $N_{turbines}$ communicators. Additionally, one processor is dedicated for YALES2-BHawC communication. Thus, the total number of processors is $N_{turbines} + 1$ plus those required in the fluid domain.

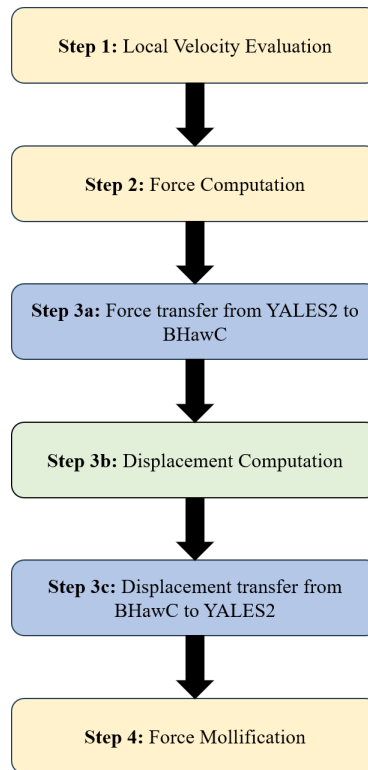


Figure 2.19: A simplified flowchart of the YALES2-BHawC coupling.

The steps followed in the temporal loop are shown in Fig. 2.19. As seen, the workflow diverges from that of rigid ALM (shown earlier) during step 3, when the blade displacement is to be computed. The aerodynamic forces computed by YALES2 are sent to BHawC and after appropriate coordinate and basis transformations, are used to obtain a solution to Eq. (2.40). The incremental displacements are sent back to YALES2 where the step-wise mollification of forces is implemented.

The weak nature of the coupling stems from the lack of recursion between YALES2 and BHawC. The forces computed by YALES2 are based on the displacement of the previous time-step. They are not updated once the actual displacements are known. Thus, information is only exchanged at the start of a fluid/structural time-step. The time-step in BHawC is always fixed at 0.02s, to respect the convergence criteria of the solver [10]. The fluid time-step, dependent on the Courant Flow number, can be varied via the mesh resolution. In this project, the fluid time-step for the coupled simulations is also fixed at 0.02s but this is sub-optimal [36].

2.7.3. Review of wind turbine fluid structure interaction studies

This section presents a number of studies in the domain of Fluid Structure Interactions (FSI) wherein a CFD library has been coupled to a structural solver to carry out a multiphysical simulation of a wind turbine. Simultaneously, the differences with the YALES2-BHawC coupling are illustrated.

One of the first coupled simulations of a wind turbine, including the tower and nacelle, was carried out by Hsu et al. [56]. The fluid domain was solved using an Arbitrary Lagrangian Eulerian (ALE) approach [57] using the variational formulation of the Finite Element Method (VMS-FEM). ALE uses a mesh adaptive strategy wherein the fluid mesh around the turbine follows the rotation of the blades. This approach is a concrete implementation of a blade-resolved simulation as can be seen in Fig. 2.20. But the computational costs of re-meshing at every iteration are quite significant. The structural solver utilized a NURBs based Iso-geometric Analysis (IGA). Although this approach was able to predict rotor performance with higher

precision that standalone ALM-LES, the computational costs and the inability of FEM to capture non-linear wake phenomena meant that large-scale wind farm simulations could not be carried out.

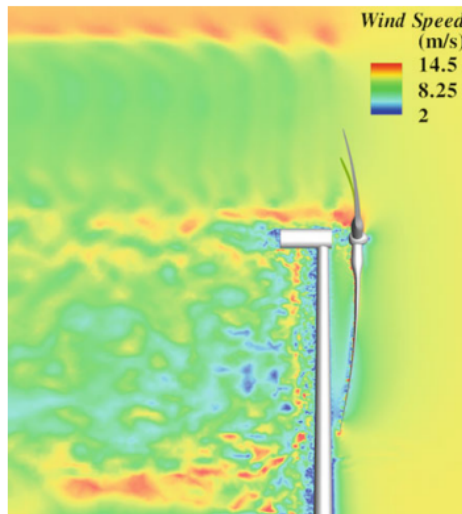


Figure 2.20: The instantaneous velocity contour showing the wake behind the full-resolved geometry of the turbine- from Figure 13 pg. 830 of *Fluid–structure interaction modeling of wind turbines: simulating the full machine* by M. Hsu et al.[56]

Subsequently, a number of coupled modules were developed. The most widely used of which, is NREL's SOWFA (Simulator fOr Wind Farm Applications) [58]. The CFD library OpenFOAM [59] is coupled with OpenFAST. In OpenFOAM, a number of turbine modelling methods are made available, the most commonly used of which is ALM. Additionally, the fluid domain can be solved with LES or URANS. While OpenFAST has a number of modules for handling aerodynamics, hydrodynamics, control and structural response of wind turbines. In a method similar to the YALES2-BHawC coupling, the aerodynamic module is replaced by OpenFOAM. A plethora of studies have been carried out using SOWFA [60, 61] but only the ones focusing on wake analysis have been discussed here.

The advantages of switching from rigid to elastic ALM-LES are underscored by Zheng et al. [62], where a single and two-turbine configuration was analyzed using both frameworks. A LES setup was used with the standard Smagorinsky sub-grid model while the domain was discretized with low-order schemes. While rigid ALM overpredicted the turbine thrust and consequently the power output- particularly for the downstream turbine, elastic ALM gave much more realistic estimations of the turbine performance. This can be seen in Fig. 2.21. It was found that the blade deformation had a strong influence on the near and far-wake structure. As an example of the influence of blade elasticity, the tip vortex rotation speed was found to decrease when switching from rigid to elastic ALM. Moreover, the interference and breakdown of the vortices was delayed into the far-wake region as shown in Fig. 2.22. These changes in the wake behaviour were attributed to the lower aerodynamic thrust resulting from the spatial configuration of the deformed blades. In conclusion, the authors suggest expanding the scope of FSI to multi-turbine configurations.

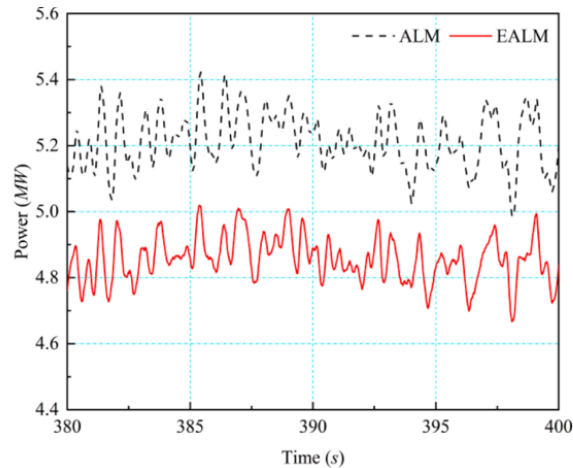


Figure 2.21: The aerodynamic power output computed by OpenFAST for the upstream, unwaked turbine under a turbulent inflow of 4% - from Figure 19a pg. 16 of *Numerical investigations of coupled aeroelastic performance of wind turbines by elastic actuator line model* by J. Zheng et al.[62]

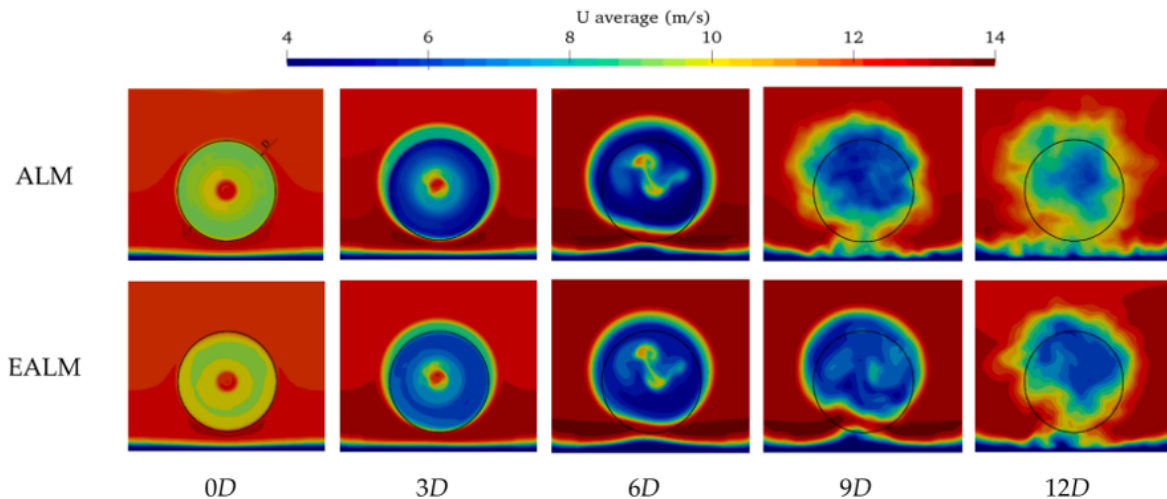


Figure 2.22: The streamwise velocity contours averaged over 20 seconds on a plane perpendicular to the inflow direction at different downstream distances - from Figure 16 pg. 14 of *Numerical investigations of coupled aeroelastic performance of wind turbines by elastic actuator line model* by Zheng et al.[62]

Along these lines, Chanprasert et al. [63] analyzed the effect of directionally sheared inflows on wake development and on the fatigue damage of waked turbines. A four turbine in-line configuration was chosen and subjected to inflow with no directional shear, wind veering (Northern Hemisphere) and wind backing (Southern Hemisphere) at fixed latitudes. The one-equation Deardoff-Lily model was used to compute the sub-grid stresses while second order time and spatial schemes discretized the flow domain. Atmospheric effects were also included. Directional shear was observed to affect wake rotation and radial wake expansion. As seen in Fig. 2.23, the wake was skewed in the direction of veer. Wind veering also reduced wake expansion and the narrower wake caused more damage in the flapwise direction at 1P frequency. But the edgewise damage was unaffected by the directionality of the shear.

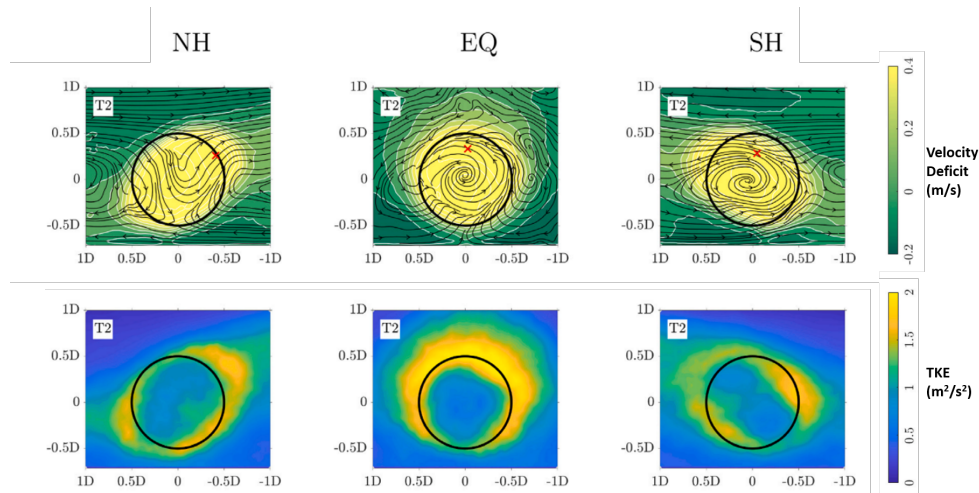


Figure 2.23: The time-averaged axial velocity deficit (top) and the turbulent kinetic energy (bottom) 1D downstream of the second turbine showing how the wake profile is affected by the wind veer- from Figures 8 and 10 pgs. 1101 and 1103 of *Large Eddy Simulation of wind turbine wake interaction in directionally sheared inflows* by W. Chanprasert et al. [63]

An in-depth analysis of fatigue damage under neutral and unstable atmospheric conditions was carried out by Chanprasert et al. [64]. The SOWFA coupling was applied to a four turbine in-line configuration for above and below rated conditions. Additionally, the effectiveness of active yaw control was evaluated. As shown in Fig. 2.24, it was found that in below-rated conditions, atmospheric stability (neutral or unstable) did not affect any of the fatigue channels. But during above-rated operation, the damage equivalent load (DEL) for rotor shaft torque and yaw bearing moment was significantly higher under neutral conditions. The last turbine was the worst affected. The authors also concluded that while active yaw control reduced loads on downstream turbines, there were no power gains.

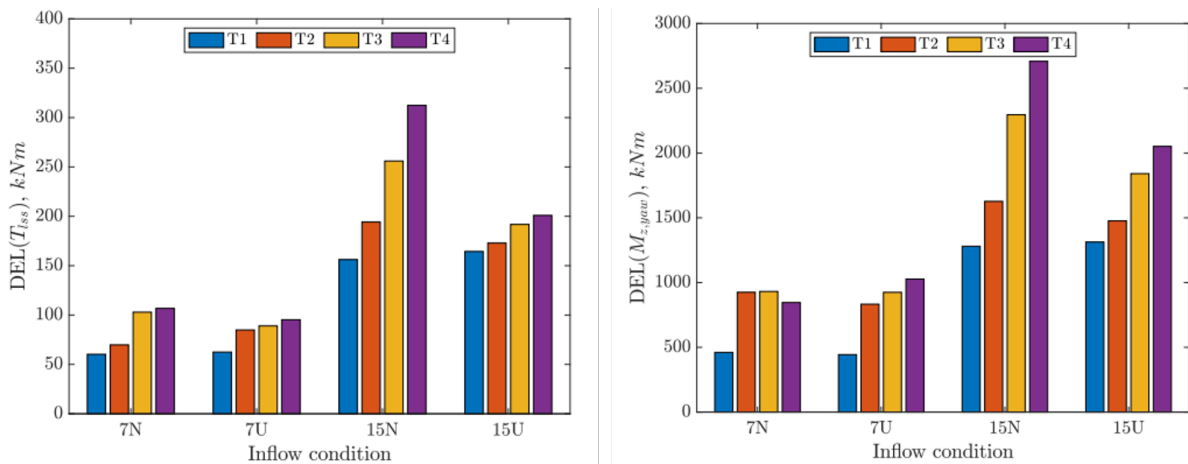


Figure 2.24: Bar plots showing the Damage Equivalent Load (DEL) for the rotor shaft torque (right) and the yaw bearing moment (left)- Figure 9 pg. 217 from *Large Eddy Simulation of wind turbine fatigue loading and yaw dynamics induced by wake turbulence* by W. Chanprasert et al. [64]

HAWC2CFD is another FSI coupling which links the aero-elastic code HAWC2 to the CFD code EllipSYS3D [65]. The former is a state-of-the-art aero-elastic code that uses a multi-body approach to emulate the structural response of a wind turbine. On the other hand, EllipSYS has high-order implementations of RANS, DES and LES. HAWC2CFD has been used to analyze atmospheric flow around a single turbine [66], vortex [67] and stall-induced vibrations [68]

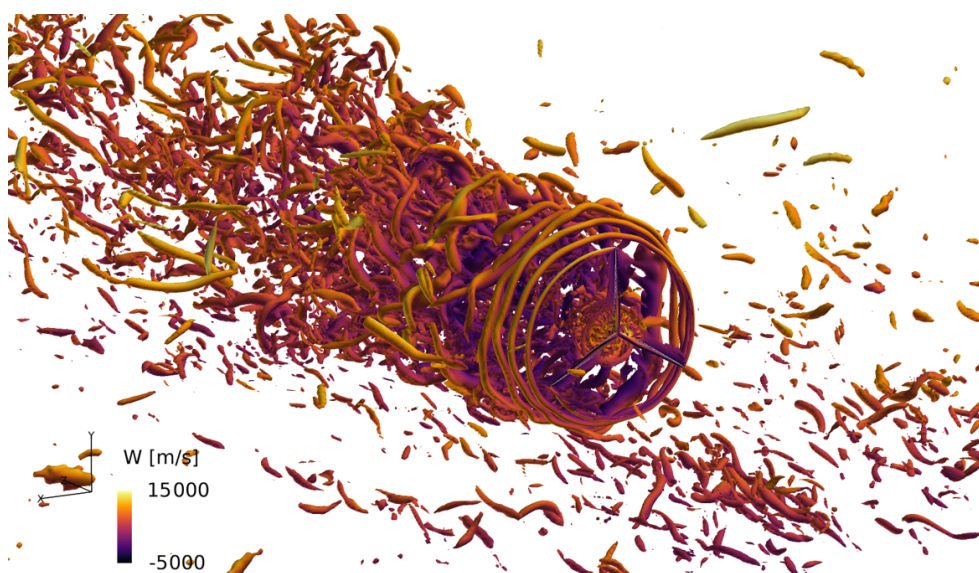


Figure 2.25: The Q-criterion isosurface showing the instantaneous flow velocity behind a 2.3MW turbine as simulated by EllipSYS3D- from Figure 9 of *Wind turbines in atmospheric flow: fluid–structure interaction simulations with hybrid turbulence modeling* by C. Grinderslev et al. [66]

A study by Bromm et al. [69] focused on wake development in directionally sheared inflows. PALM, an open-source LES library was coupled to OpenFAST. Additionally the fatigue damage and power output for the downstream turbine was quantified. The recycling method of turbulence generation [70] was used on a Cartesian grid to obtain a fully-developed boundary layer. The directional shear resulted in a distinctively asymmetric wake while its expansion was skewed resulting in an elliptical profile. The direction of wake propagation was also affected by the shear. Finally, the fatigue damage was found to be the highest when the second turbine was at a lateral offset of $-0.5D$. This was mainly due to the shape of the wake imposing significant velocity gradients on the blade in the partial-wake or half-wake condition.

Despite the advances in elastic ALM, a number of challenges still remain [6, 24]. These have include longer run times, computational costs and the human time spent in the set-up, monitoring and post-processing of simulations. The latter severely limits parametric studies on wind turbine wakes since the number of simulations can become unmanageable. This has restricted the usability of elastic ALM, especially in the wind energy industry.

Examples of more couplings can be found in [71] and [72]. The latter is similar to the YALES2-BHawC coupling in that higher order discretization schemes are used along with the Prediction Correction method. But the coupling with OpenFAST and the subsequently larger structural time-step means that synchronization requires the fluid time-step to be much smaller. This comes with significant computational costs. In a more advanced application, the behaviour of floating wind turbines has been studied using FSI by Xu et al. [73].

Currently, the BHawC-YALES2 coupling has been used to analyse two-turbine configurations with and without yaw [36]. Herein, it was found that for positive yaw, the edgewise fatigue damage on both the turbines was reduced. In the flapwise direction, it was observed that the damage on the yawed turbine increased while on the waked turbine, it decreased. Additionally, the evolution of the wake was studied in terms of the mean kinetic energy and momentum budgets. Four regions of wake recovery were identified based on the vortex structures. Lastly, level-set functions were used to define the wake boundaries. Additionally, the coupling has been validated against field data by Muller et al [74] wherein a good agreement was found. Thus, it can be used for a more in-depth investigation of wind turbine wakes.

2.8. Literature review conclusion

After a review of methods used to study wind turbine wakes and past studies in this domain, it can be summarized that elastic ALM-LES captures the multi-scale and multi-physical nature of wind turbine wakes

while demanding computational resources that can be feasibly obtained. Indeed, the results provide a wealth of information on a number of phenomena. The YALES2-BHawC coupling offers additional benefits of high-order schemes, modelling of blade deformation, realistic control of the turbine and scales well for problems with a large mesh. Lastly, the usage of the coupling within the industrial setting of Siemens Gamesa allows for it to be applied to a number of wake scenarios without the need for additional validation.

Thus, the objective of this thesis is to enhance the knowledge-base of wind turbine wakes while creating a standardized tool that can be re-used for similar studies. This requires the following questions to be answered:

1. What method can generate inflow turbulence for Large Eddy Simulations of wind turbine wakes such that the turbulence itself is fully developed and close to offshore conditions? In particular, what are the required boundary conditions and domain dimensions?
2. Can the usability of elastic ALM-LES be extended to parametric studies? This would involve a reduction in the human-time spent on the different steps of a simulation. Thus, in other words, what methodology can consolidate and automatize elastic ALM-LES of wind turbine wake while ensuring that it is easily adaptable to different user inputs?
3. What is the impact of different inflow conditions, namely wind speed and turbulence intensity, on wake recovery, meandering and power production in a multi-wake situation?
4. How important is it to consider the wake position on the downstream rotor in different partial-wake situations when assessing the fatigue damage accumulated by the blade?

This concludes the discussion on the background and aim of this project. The next chapter addresses the first question of generating turbulent inflow.

Inflow conditions: recycling method for turbulence generation

This chapter presents a method for generating turbulent inflow for the ALM-LES study of wake interaction scenarios that satisfies two criteria: the turbulence profile is fully developed as the flow does not evolve in the stream-wise direction and the turbulence properties are close to those of an offshore environment. For this, a recycling method is used. First, a review of the available methods for generating turbulent inflow in LES is presented followed by an overview of the recycling method used in this project. The next section defines the properties required from the resultant flow field and a sensitivity study is carried out on the domain size and boundary conditions in order to achieve them. Finally, a parametric study on the ground roughness and recycling flow-rate is used to create a database of inputs which can be used to initialize the external flow for subsequent wind turbine wake simulations.

3.1. An introduction to turbulence generation for LES

For any CFD simulation, the type and method of inflow used is critical as it affects the characteristics of the resultant flow field. Particularly, in case of a wind turbine simulation for example, the dissipation and the meandering of the wake is largely determined by the inflow turbulence [29]. The reliability of the Actuator Line Method is also dependent on it [24]. Additionally, for wind turbine design, the IEC-61400 [75] standards require the wind profile incident on the rotor to follow a logarithmic or power law:

$$u(z) = u(z_r) \cdot \frac{\ln(z/z_0)}{\ln(z_r/z_0)}, \quad (3.1)$$

$$u(z) = u(z_r) \cdot \left(\frac{z}{z_r}\right)^\alpha, \quad (3.2)$$

where $u(z)$ is the wind speed at height z , z_r is a reference height above ground used for fitting the profile, z_0 is the roughness height and α is the wind shear (or power law) exponent. For offshore simulations, the power-law profile is used with α equal to 0.13. The importance of a realistic shear profile is underscored by its effect on the ultimate and fatigue loads of the turbine [4].

Thus, the two main methods of generating turbulent inflow in LES are Synthetic Turbulence and Precursor Methods [76]. They are discussed herewith. Note, the following discussion does not touch upon the effects of temperature as these are not currently modelled by the incompressible solver of YALES2. Hence, a neutral atmospheric boundary layer is assumed.

3.1.1. Synthetic methods

In its simplest form, synthetic turbulence generation involves creation of some “white noise” inlet velocity with an amplitude proportional to the turbulent intensity. To obtain a more realistic “white noise”, the spectra of atmospheric turbulence can be used. This approach is used in the case of wind turbine simulations with synthetic turbulence. Here, it is important to first introduce the Frozen Turbulence Hypothesis [77]. Assuming that temporal and spatial variations in the velocity field are identical:

$$\frac{\partial \vec{u}}{\partial t} = U \frac{\partial \vec{u}}{\partial x}, \quad (3.3)$$

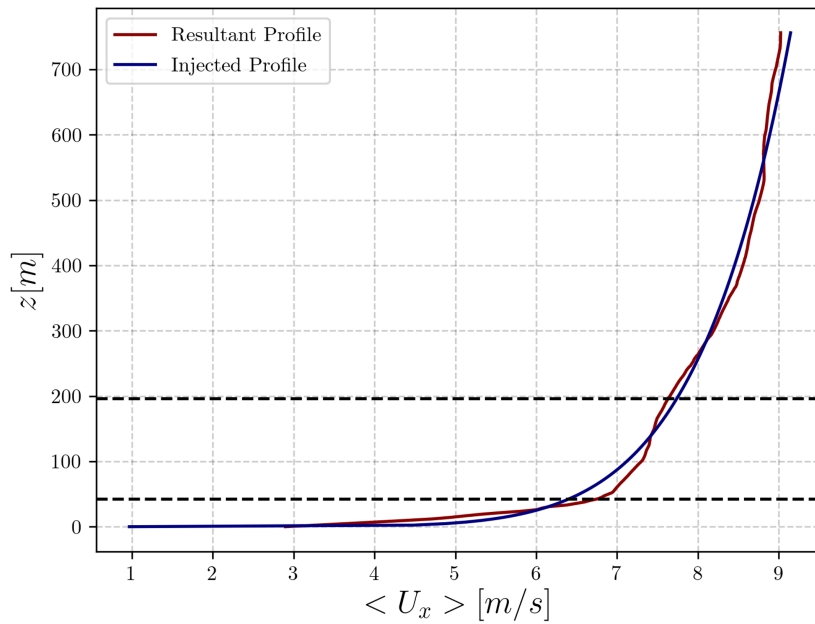


Figure 3.1: The shear profile obtained by synthetic turbulence with the Mann spectra [78] compared with the profile that was injected at the inlet. Note that the resultant profile is sourced from a location 3000m downstream of the inlet.

the time-dependent fluctuations can be obtained by convecting the “wind-box” through the domain at a velocity of U . The “wind-box” is commonly generated by the Mann Method [78] which is now a part of the IEC standards for wind turbine design [75]. A full description of the Mann Method can be found in [78], but the important aspect is that even though the turbulence spectrum is validated against measurement of the atmosphere, for a given case, the velocity profile itself is not fully developed. So as the imposed inlet boundary condition interacts with the ground roughness, more turbulence will be generated. Consequently, the added turbulence will alter the mean shear profile. An example is shown in Fig. 3.1. The effect becomes more pronounced for longer domains as the interaction between the injected turbulence and the ground increases. Hence, in order to carry out the simulation of the three turbine in-line configuration, where the domain will be as long as 7kms, synthetic turbulence generation methods will not conserve the shear profile in the stream-wise direction. For more reference, examples of other spectral methods can be found in [79] and [80].

3.1.2. Precursor methods

The problem outlined in the previous section can be addressed by generating turbulence that is already at an equilibrium with the ground. A precursor simulation can be carried out to allow the turbulence to fully develop while storing the velocity field data which is then prescribed at the inlet of the subsequent simulation. The result is that the turbulence will possess the required spatial and temporal length scales along with an energy spectrum that would be expected under the conditions of the final simulation. One of the implementations of this principle is to generate a library of turbulence data. Then, a solution from the library is mapped at the inlet to produce the turbulent inflow, as shown in Fig. 3.2.

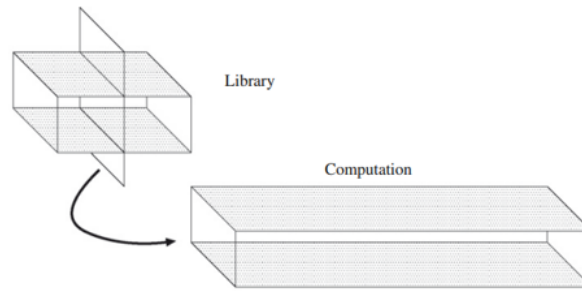


Figure 3.2: Visual Depiction of a Precursor simulation- *from Figure 1 pg. 561 of Inlet conditions for large eddy simulation: A review by G. Tabor et al.[76].*

Although this is a commonly used approach, especially for simulations attempting to include atmospheric effects, another method is used in this thesis. First, the domain under interest is extended in the stream-wise direction. Then, a periodicity can be defined between the inlet and a plane which is a certain distance upstream. After a sufficient amount of time, the resulting flow will be fully developed. This forms the basis of the recycling method and is illustrated in Fig. 3.3. The advantage of recycling is that the memory requirements of storing the library of solutions is avoided.

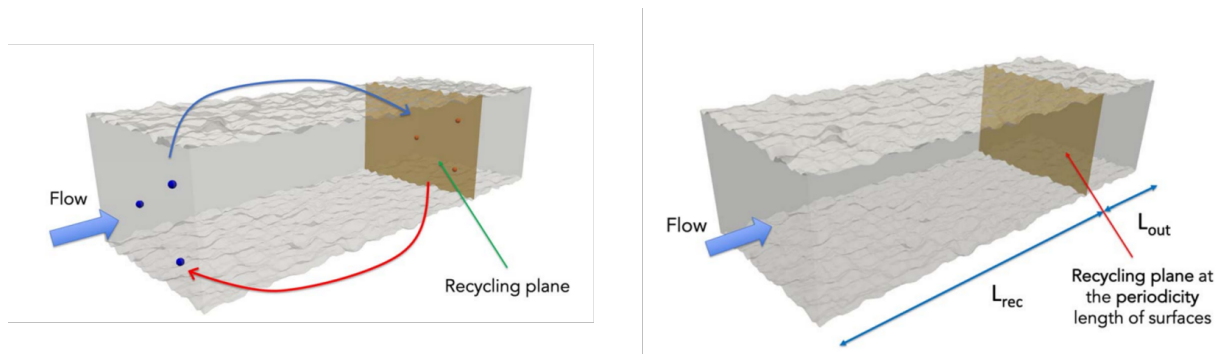


Figure 3.3: Principle of the recycling method showing the definition of the recycling plane (right) and the interpolation of the Lagrangian particles back to the inlet (left) *from Figure 4 and 5 pg. 4 of Roughness-Resolved Large-Eddy Simulation of Additive Manufacturing-Like Channel Flows by S. Meynet et al. [81].*

3.2. Recycling method for turbulence generation

The principle behind recycling is that the velocity field at a certain downstream location is iteratively re-introduced (via interpolation) at the inlet of the domain with the purpose of allowing the turbulence structures to fully develop. After a sufficient number of iterations, a shear profile that is invariant in the stream-wise direction will be obtained. As such a number of different approaches have been developed and are well documented in literature [70]. Most of these methods assume a target profile and rescale/correct the profile at the recycling plane before reintroducing it at the inlet, as shown in Fig. 3.4. An example of a recycling and rescaling method is found in [82]. But, re-scaling introduces an artificial shear profile which may not be at equilibrium with the ground roughness. Outside the recycling zone, the re-scaled profile will evolve leading to the same effect as in Fig. 3.1. Thus, in YALES2, no rescaling is used and subsequently, the target profile is not known beforehand.

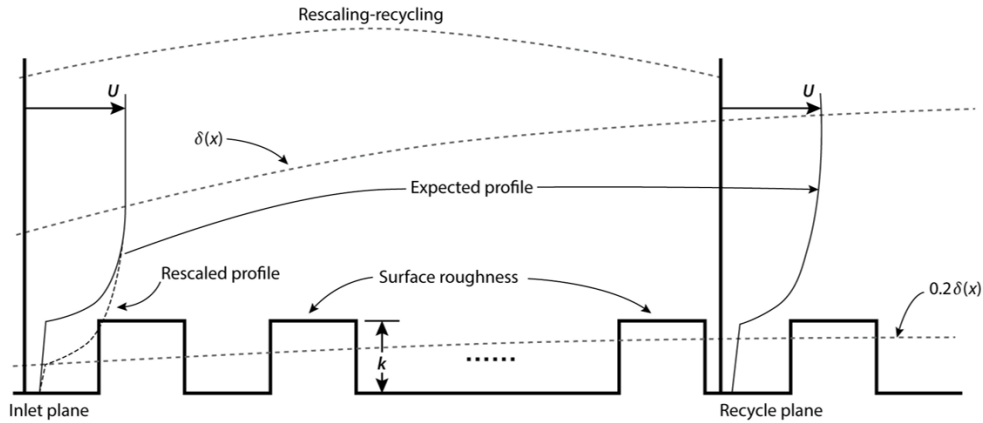


Figure 3.4: Example of recycling and Rescaling method, showing the impact of the development of boundary layer on the recycled profile- from Figure 1a pg. 32 of *Inflow Turbulence Generation Methods* by X. Wu [70].

The recycling method used in YALES2 is based on Lagrangian particles. A flow-rate is defined at the inlet and the recycling is done for $N_{iter} > 1$. The procedure is as follows:

1. Lagrangian particles are defined on the inlet plane and are translated by the imposed flow-rate (blue spheres in Fig. 3.3).
2. At the recycling plane, the velocity field is interpolated for the particles (red spheres in Fig. 3.3).
3. The particles are moved back to the inlet and the field is updated.

The interpolation step is responsible for most of the computational cost of this method. Here, a value of $\Delta t_{recycling} \sim O(e^1)[s]$ is found to give the best trade-off between performance and fidelity [81].

Another parameter of interest is the distance of the recycling plane from the inlet. This must be chosen such that the length scales in the main domain are resolved. But a smaller value would be advantageous in terms of reducing computational costs. A sensitivity to this is shown in the next section along with the investigation of the required domain dimensions and mesh resolution needed to obtain a “realistic” inflow. The exact requirements will also be introduced in the next section.

3.3. Sensitivity study

In order to use recycling as a method of inflow generation for the wake interaction cases, the resulting flow must satisfy the following properties:

- The shear profile must not develop in the stream-wise direction and must be close to the power law.
- The mean stream-wise velocity must be uniform along the lateral or transverse direction, at least over the rotor plane.
- The turbulence intensity must be in the range that is observed in an offshore environment.

It is assumed that these parameters will be affected by the domain size, mesh resolution, boundary conditions and the length of the recycling region. Thus, after defining a baseline case, a sensitivity study to these is carried out. The criteria listed above are quantified and those simulation settings which best satisfy these criteria are chosen for the subsequent cases.

Additionally, it is not known beforehand what shear profile will be obtained via recycling in YALES2. But, for the wind turbine wake simulations it is necessary to know and specify the inflow that the first turbine should be subjected to. Thus, a database of inputs for the recycling boundary condition is needed along with the resultant shear profile. This is achieved through a parametric study detailed in the next section.

3.3.1. Setup of the baseline case

The baseline case is defined with the boundary conditions (BCs) shown in Table 3.1

Table 3.1: Boundary conditions and other details for the baseline case

Metric	Value
Domain (L x W x H)	45D x 10D x 6D, where D = 126 m
Boundary Conditions	Top: Slip wall
	Bottom: Wall law
	Left: Periodic + Slip wall
	Right: Periodic + Slip wall
	Outlet: Constant Outflow
recycling Niter	20
Target wind speed at hub (u_{ref})	7 m/s
Bottom Roughness (z_0)	0.04 m
Length of recycling Region (Lrec)	25D

The recycling zone is kept larger than the domain under study to ensure that all the relevant length scales are taken into account. Additionally, the side walls in the recycling zone are given a periodic boundary condition such that the wind field is free to evolve in the lateral direction, as shown in Fig. 3.5. A slip wall with a law-of-the-wall model is used to specify the shear stress at the bottom of the domain:

$$\tau_w = \rho u_*^2. \quad (3.4)$$

Where u_* is the friction velocity given by:

$$u_* = \frac{\kappa u(z_1)}{\log\left(\frac{z_1+z_0}{z_0}\right)}. \quad (3.5)$$

Such that κ is the Von Kármán constant, z_1 is the height of the first node closest to the ground, $u(z_1)$ is the stream-wise velocity at that node and z_0 is the ground roughness specified by the user. A Dirichlet boundary condition is given at the outlet with a flat velocity profile. This is done to prevent any backflow. As stated in the previous section, it is not possible to define the target profile in the implementation of the recycling method in YALES2. Instead, the recycling inlet boundary condition in YALES2 requires the specification of a constant flow-rate. This was given by integrating the target power law profile over the inlet:

$$Q = \iint u(z) dy dz, \quad (3.6)$$

and,

$$u(z) = u_{ref} \left(\frac{z}{h_{ref}} \right)^\alpha, \quad (3.7)$$

where, h_{ref} is the hub height and α is 0.13 which is the standard for offshore wind turbine simulations [75].

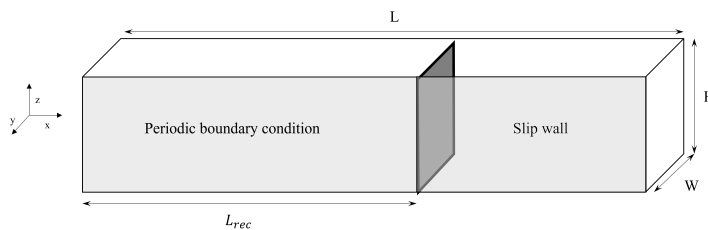


Figure 3.5: A representation of the domain showing the dimensions, the length of the recycling region and the recycling plane (in green). Note, x is the stream-wise direction, y is the transverse or lateral direction and z is the vertical direction.

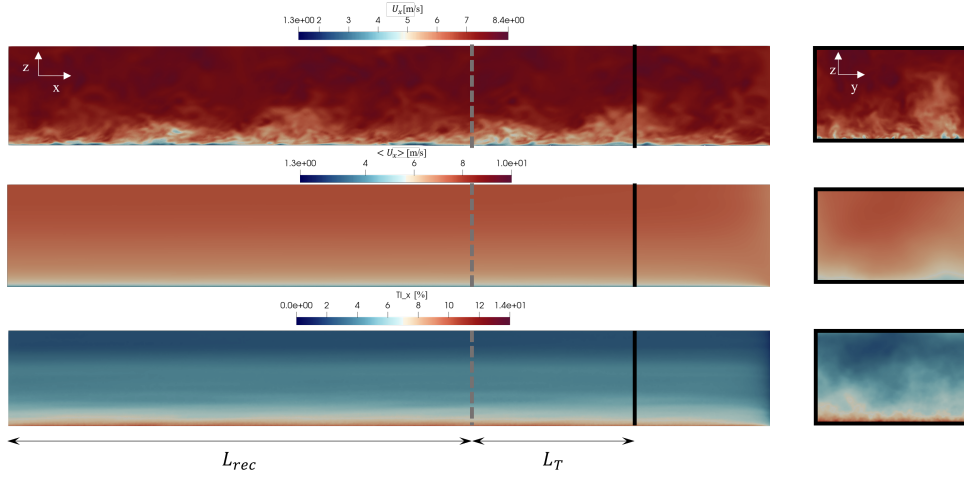


Figure 3.6: From top to bottom: the iso-contour of the instantaneous stream-wise velocity (U_x), the time-averaged stream-wise velocity ($\langle U_x \rangle$) and the stream-wise turbulence intensity (TI_x) on a vertical slice normal to the lateral direction (left) and another slice normal to the stream-wise direction (right). The recycling plane is indicated by the gray line whereas the black line denotes the turbine location in the subsequent simulations.

The mesh was generated using ANSYS Workbench and imported into YALES with a homogeneous grid refinement. This resulted in a cell size of 7.875m ($\frac{D}{16}$) at the bottom of the domain and 15.75m ($\frac{D}{8}$) at the top, with a linear interpolation between these two values. The flow field was found to converge after 13 to 15 flow-through times (t_f) and the time-averaged statistics were accumulated for the same amount of simulated time:

$$t_f = \frac{L}{u_{ref}}. \quad (3.8)$$

3.3.2. Baseline results and definition of the criteria for the resultant flow field

The Fig. 3.6 and Fig. 3.7 shows the iso-contours of U_x , $\langle U_x \rangle$ and TI_x . Here, repeating structures are seen in the slice of U_x which is a result of the periodic recycling. The slices of the time-averaged statistics show a uniformity along the stream-wise direction. Although there are no turbines in the domain, the location of the first turbine in Chapter 5 and Chapter 6 is also indicated by the dark black line. L_T is its distance from the recycling plane for which a value of $5D$ is used since this ensures that the induction effect of the turbine is not recycled.

Fig. 3.7 displays the stream-wise velocity component along the vertical direction showing the resultant shear profile at different stream-wise locations defined with respect to the inlet (a), the stream-wise turbulence intensity also along the vertical direction (b), the stream-wise velocity component along the lateral direction (c) and finally the shear profile at the turbine location fitted to a power law (d). With respect to Fig. 3.7a, it can also be seen that the shear profile does not evolve in the stream-wise direction. Thus, the turbulence is judged to be fully developed. The slight difference for the profile at $40D$ is due to the influence of the outlet boundary condition. Imposing a flat velocity profile at the outlet leads to a reduction in the wind speed at the top of the domain and a slight speed-up closer to the bottom. Thus, results from and beyond $40D$ will not be considered. For the rest, at the hub height, $\langle U_x \rangle$ was found to be 7.35m/s , which is close to the target of 7m/s .

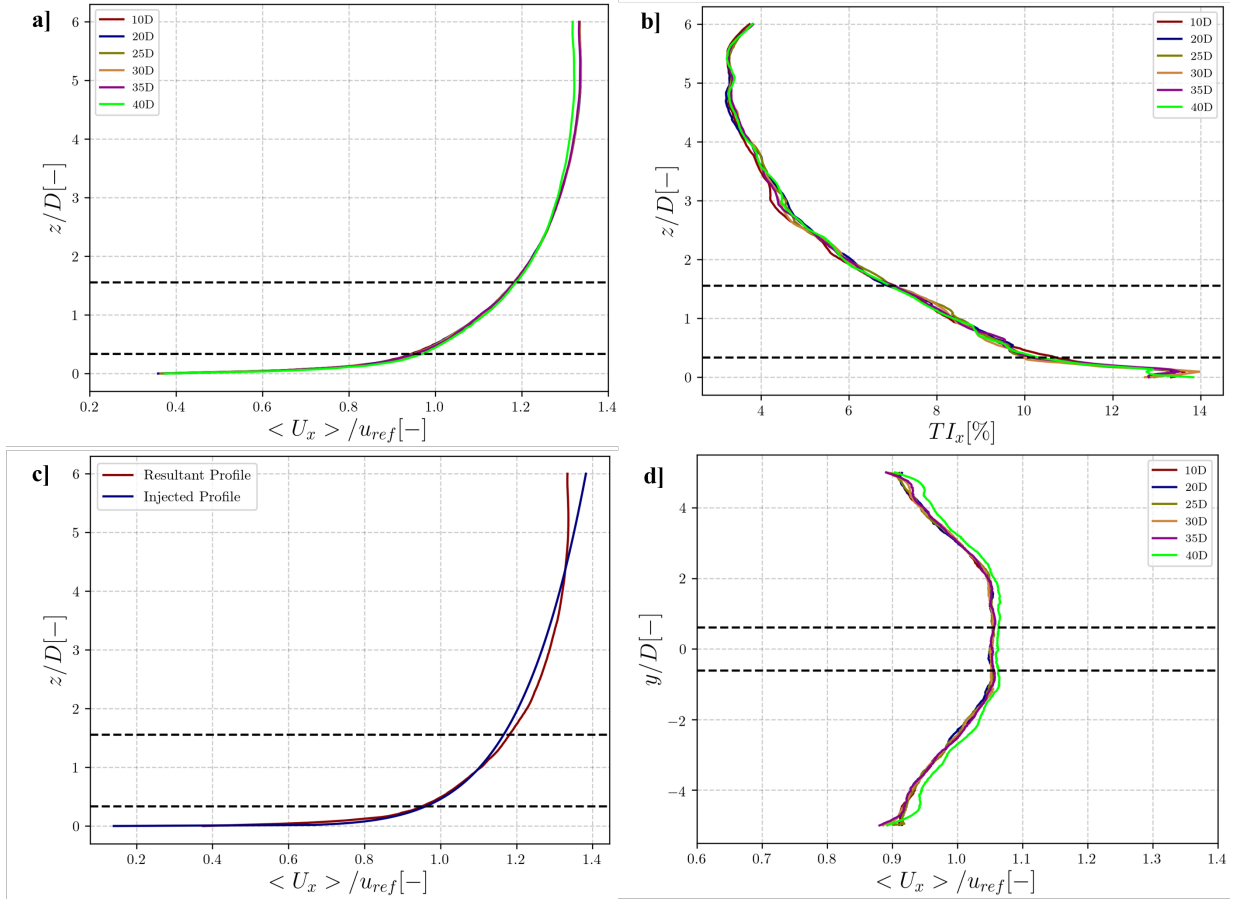


Figure 3.7: Velocity field time averaged statistics for the baseline case. The stream-wise velocity component along the vertical direction showing the resultant shear profile at different stream-wise locations defined with respect to the inlet (a), the stream-wise turbulence intensity also along the vertical direction (b), the stream-wise velocity component along the lateral direction (c) and finally the shear profile at the turbine location fitted to a power law (d). The dashed black lines indicate the rotor plane.

Fig. 3.7b shows the turbulence intensity (TI_x) computed according to the following relation:

$$TI_x = \frac{\sqrt{\langle u'^2 \rangle}}{\langle U_{hub} \rangle} * 100, \quad (3.9)$$

where u' is the velocity fluctuation around the mean. The average stream-wise turbulence intensity over the rotor plane for the baseline case was 9.1%. This is slightly higher than what is observed in LES of neutral atmospheric boundary layers [83] but in the range of measurements carried out at offshore wind farms [84]. In Fig. 3.7c, the shear profile at the turbine location (30D) is fitted to a power law using a least-squares regression method. Although the resultant profile does not perfectly match the power law, the value of α is 0.126 which is close to the target of 0.13. Thus the error from the power law profile (ϵ_r) is quantified as:

$$\epsilon_r = \frac{1}{2D} \int_0^{2D} |\langle U_x^{powerlaw} \rangle - \langle U_x^{resultant} \rangle| dz, \quad (3.10)$$

where the $\langle U_x^{powerlaw} \rangle$ is the profile obtained from curve-fitting and $\langle U_x^{resultant} \rangle$ is the profile obtained at a distance of 30D from the inlet. Here, α for $\langle U_x^{powerlaw} \rangle$ deviates from the value of 0.13. This is judged to be acceptable since $\alpha = 0.13$ is a stringent requirement for design and certification of wind turbines which is not the goal of this project.

It is observed that ϵ_r can be up to 2-3% of the mean velocity at hub-height. This is because, with a law-of-the-wall boundary condition on the ground, it is not possible to obtain a profile that exactly matches

the power law. Indeed, the law-of-the-wall assumes that the domain is within the log-layer of the boundary layer. But, it should be possible to minimize ϵ_r as it was observed to be sensitive to the parameters under study. Thus, in addition to the rotor-averaged turbulence intensity, this was chosen as a criteria for selecting the “correct” domain size and boundary conditions.

Lastly, from Fig. 3.7d it can be seen that the stream-wise velocity has large fluctuations along the lateral direction, with a peak-to-peak difference of 1.2m/s. Although this has been observed in literature [85], a uniform velocity distribution must be obtained, at least over the rotor plane. This is because a non-uniform inflow may introduce spurious features in the wake. For example, it has an impact on the wake recovery and meandering. After running a number of simulations with different domains, meshes and boundary conditions, a completely uniform stream-wise velocity in the lateral direction was never obtained. Thus, for the scope of this project, a less stringent criteria of minimizing the root-mean-square $\sigma_{\langle U_x^y \rangle}$ of the fluctuations in the rotor plane was considered. This criteria can be defined as follows:

$$\sigma_{\langle U_x^y \rangle} = \sqrt{\frac{1}{D} \int_{-D/2}^{D/2} \left(\langle U_x \rangle - \frac{1}{D} \int_{-D/2}^{D/2} \langle U_x \rangle dy \right)^2 dy}. \quad (3.11)$$

3.3.3. Results of the sensitivity study

The results of the sensitivity study are summarized herewith. Fig. 3.8 shows the rotor-averaged TI_x for different cases. Then, Fig. 3.9 depicts the error with respect to the power law profile as computed by Eq. (3.10). Finally, Fig. 3.10 presents the fluctuations along the lateral direction in $\langle U_x \rangle$, as quantified by Eq. (3.11).

Fig. 3.8 shows the rotor-averaged TI_x for different cases. This parameter was found to be independent of the domain width and recycling zone size. But the domain height played a more impactful role. This was a consequence of the hub being relatively closer to the ground and in a more “turbulent” region of the boundary layer. In case of grid refinement, the wind speed at hub was lower (and closer to the 7m/s target), which led to a higher TI . On the other hand, the wind speed at hub was higher in the Cartesian mesh case leading to a rotor-averaged TI_x of 8.4%.

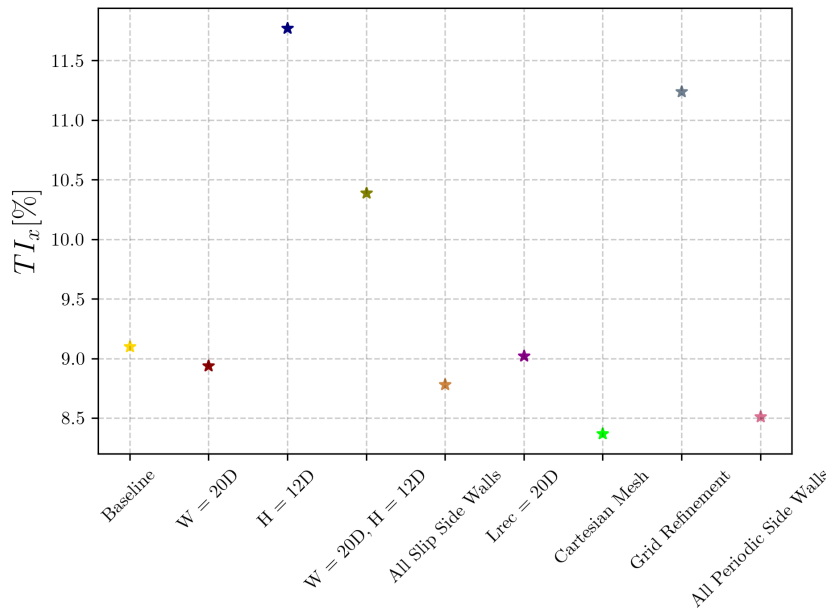


Figure 3.8: The rotor averaged TI_x for different cases

Fig. 3.9 depicts the error with respect to the power law profile as computed by Eq. (3.10). Here, a grid refinement resulting in a mesh size of 196 million elements only slightly reduced the error. Thus, the mesh settings defined earlier are judged to be sufficient in terms of providing the required shear profile. A change

in the recycling length from 25D to 20D also did not have a significant effect. But, a change in domain height was found to be detrimental. This is because the rotor region over which the error is computed is at a lower normalized distance from the ground. Here, the velocity profile tends towards a log-law. But when doubling the domain width, the error is only slightly reduced.

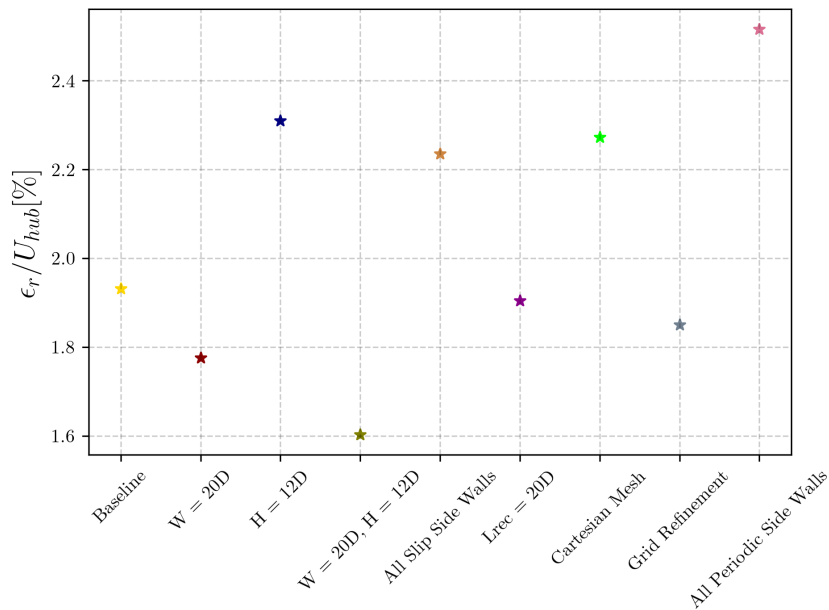


Figure 3.9: The error from the shear profile ϵ_r (refer Eq. (3.10)) for different cases expressed as percentage of the target velocity at hub height (7m/s)

Fig. 3.10 presents the fluctuations along the lateral direction in $\langle U_x \rangle$, as quantified by Eq. (3.11). In this case, changing the domain width was not found to provide any improvements. This is also found to be the case when increasing the domain height. Even with a structured Cartesian mesh, the non-uniformity did not disappear. Thus, it can be said with a degree of confidence that the mesh itself is not responsible for the observed behaviour. The constraintment of the flow due to the slip walls outside the recycling region was also not at fault, since the case with all periodic side walls gave similar results.

While some cases provide acceptable results for the TI_x and ϵ_r , not much improvement is seen over the baseline case for $\sigma_{\langle U_x^y \rangle}$. Curiously, this issue could not be resolved even with a wider box where it was expected that by allowing larger turbulent structures to develop in the lateral direction, the flow would become more uniform. Unfortunately, the physical reason behind the observed trend could not be investigated within the scope of this project. Additionally, neither literature highlighting or addressing this as a possible issue with the recycling method nor studies providing evidence of the contrary have been found. It has already been shown that the mesh is not responsible. Thus, it is postulated that the wall model used at the bottom maybe at fault. Or this could be an artifact caused by the Lagrangian particle based recycling implemented in YALES2. But it is important to highlight that even in the worst case, the fluctuations are limited to less than 2% of the target wind speed at hub. So another hypothesis is that the non-uniformity is physically accurate although this cannot be confidently asserted with the available data.

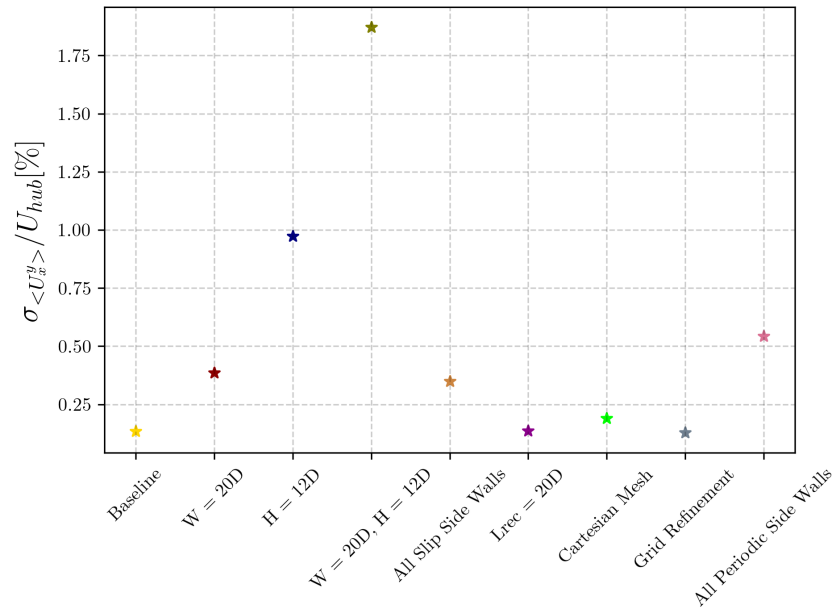


Figure 3.10: The root-mean-square of the fluctuations in the stream-wise velocity along the lateral direction $\sigma_{\langle U_x^y \rangle}$ (refer Eq. (3.11)) for different cases expressed as a percentage of the target velocity at hub height (7m/s)

For the purposes of this thesis, the results obtained with a reduced recycling length are judged to sufficiently meet the criteria. Thus, the total length of the box can also be reduced which is advantageous from a computational point of view. The next section focuses on the dependence of the shear profile and TI on the ground roughness and the imposed flow-rate.

3.4. Parametric study on the ground roughness and inlet flow-rate

The purpose of this parametric study was two-fold: to create a database from which to obtain the desired inflow for the subsequent cases and study the impact of the ground roughness on the rotor-averaged TI_x . For this six target wind speeds (u_{ref}) were simulated wherein Q was computed using Eq. (3.6). The roughness values were in the range of 0.0001 to 0.2m.

Fig. 3.11 displays the iso-contours of the velocity field for the case with $z_0 = 0.17$ and $u_{ref} = 6m/s$. Comparing this with Fig. 3.6, the effect of increasing the ground roughness can be seen. $\langle U_x \rangle$ in this case is lower close to the ground. Simultaneously, there is an increase in turbulence. These are due to the higher shear stress gradient imposed by $z_0 = 0.17$.

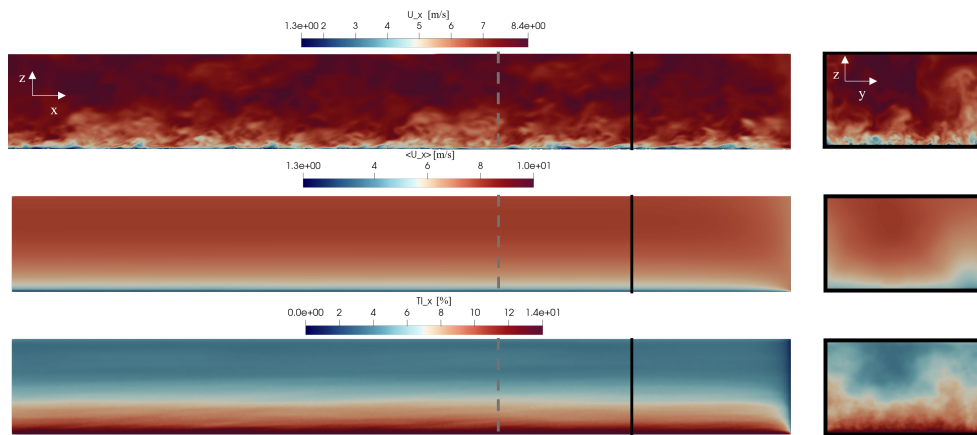


Figure 3.11: From top to bottom: the iso-contour of U_x , $\langle U_x \rangle$ and TI_x on a vertical slice normal to the lateral direction (left) and another slice normal to the stream-wise direction (right), for the case with $z_0 = 0.17$ and $u_{ref} = 6\text{m/s}$. The recycling plane is indicated by the gray line whereas the black line denotes the turbine location in the subsequent simulations.

The relationship between the stream-wise TI_x and the surface roughness for different wind speeds is seen in Fig. 3.12. While the turbulence intensity increases with roughness, the relationship is not monotonic. The same behaviour is observed for the other two components. Thus, based on regression, it is not possible to predict beforehand the resultant turbulence intensity that would result from the recycling method. The correlation coefficient was computed to be 0.6 while a value of 0.2 was observed for an offshore wind farm in [86]. The discrepancy mainly stems from the absence of temperature effects in the recycling method of turbulence generation. Regarding the variation of the TI with the wind speed, no clear trend is observed but for some roughness values, the TI appears to be higher at lower wind speeds in accordance with field data [84]. Additionally, the possibility of varying the turbulence intensity while keeping the wind speed constant is quite advantageous. This will be utilized in the parametric study on the wind turbine wake cases in Chapter 5.

Regarding the resultant wind speed at hub, from Fig. 3.13, it can be seen that values close to the target are obtained. Thus, the method of setting the flow-rate according to Eq. (3.6) will be used for all subsequent cases with the recycling boundary condition. With respect to the data for the shear coefficients, it is approximately in the range of 0.06 to 0.18 for offshore applications [87]. A trend is observed wherein the roughness increases α . This is because larger roughness values will generate more turbulence resulting in a steeper slope of the vertical shear profile which is parameterized by α .

In conclusion, the recycling method provides a turbulent inflow for wind turbine wake interaction simulations that is fully developed and approximates physical conditions if these are desired. The additional advantage is that this method is easy to implement and automatize (as will be shown later). More importantly, it allows for selective control of the properties of the flow field. Some of the solutions from this parametric study will be used to initialize all subsequent simulations, in order to provide the converged, turbulent external flow. The selected cases can be found in Table 3.2 and Table 3.3. The next chapter will focus on the creation of a workflow for automatizing the study of a variety of wind turbine wake simulations.

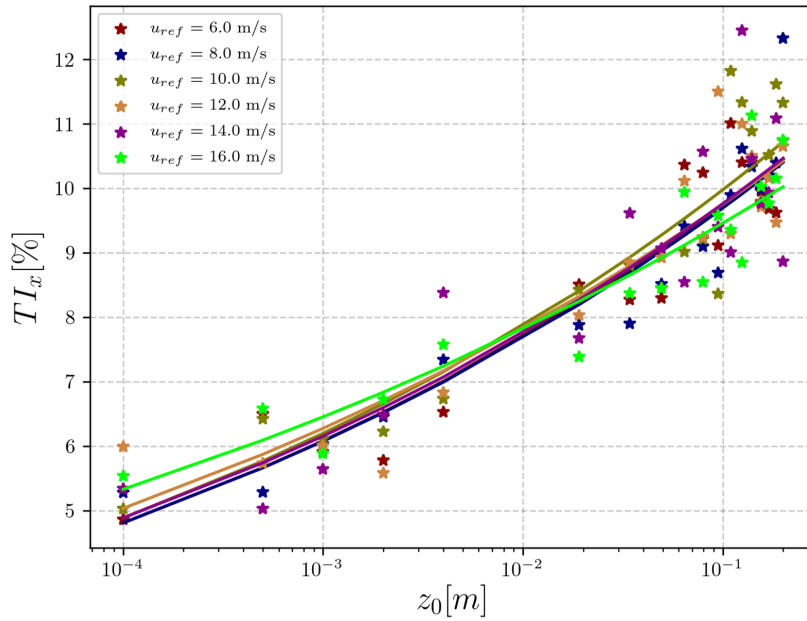


Figure 3.12: The rotor-averaged turbulence intensity as a function of the surface roughness. Note, the data are fit using a function which is of the form: $y = ce^{mx}$.

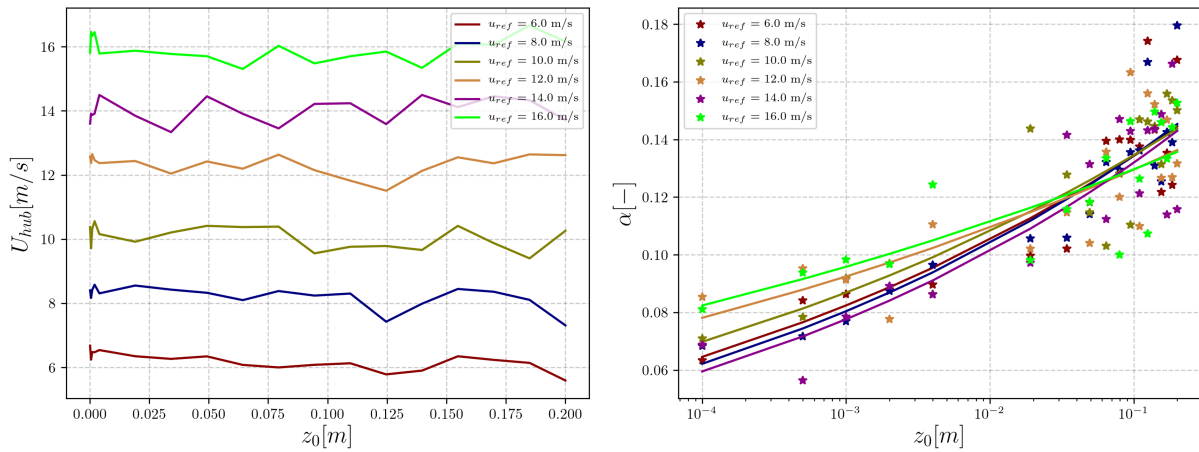


Figure 3.13: Left: the average wind speed at hub in the stream-wise direction obtained at the end of recycling for different roughness and wind speed combinations. Right: the shear coefficient of the fitted power-law profile obtained at the end of recycling for different roughness and wind speed combinations.

Table 3.2: The inflow conditions used in Chapter 5

Case No.	Target $\langle U_x \rangle$ at hub (m/s)	Actual $\langle U_x \rangle$ at Hub (m/s)	Rotor-Averaged $TI_{x,y,z}$ (%)	Shear Coefficient
1	8.0	8.3	5.3, 3.7, 3.1	0.07
2	12.0	12.4	5.7, 3.9, 3.1	0.09
3	14.0	14.3	5.3, 3.7, 3.3	0.07
4	8.0	8.8	10.3, 7.5, 6.1	0.13
6	14.0	14.5	10.5, 7.5, 6.3	0.14

Table 3.3: The inflow conditions used in Chapter 6

Target $\langle U_x \rangle$ at hub or u_{ref} (m/s)	Actual $\langle U_x \rangle$ at Hub (m/s)	Rotor-Averaged TI_x (%)	Shear Coefficient
8.0	8.3	8.5	0.11
14.0	14.4	8.6	0.13

4

Towards a parametric study of wind turbine wakes

This chapter addresses one of the limitations of ALM-LES to develop a methodology that will allow parametric studies of wind turbine wakes to be carried in a more seamless manner while ensuring the reliability of the results.

Simulations using the ALM-LES framework can be tedious to setup, given the requirement of precursor simulations for the external flow, mesh refinement, etc. When adding another layer of complexity in case of a parametric study, the number of simulations can inflate to a point where it is no longer feasible to do the pre-processing manually. Questions can also arise regarding the accuracy of the results given the possibility of inadvertent bugs in the setup. Simultaneously, the availability of computational resources has opened the door for such parametric studies to be investigated. Thus, the goal of this chapter is to develop and implement a workflow that unifies all the steps for carrying out a single study on wind turbine wakes. The steps include convergence of the external flow, wake flagging for mesh refinement and subsequent adaptation, wake convergence and accumulation of statistics on converged flow field. Once this is achieved, the whole process can be automatized to create a pipeline. Herein, just by providing a handful of inputs, a parametric study can be launched at “the press of a button”.

This chapter starts from a discussion of the steps required to setup a wind turbine wake simulation using the ALM-LES framework. Then, the wake flagging method is presented which is based on level-set functions. This is followed by a step-wise description of the refinement procedure and a study on fine-tuning the threshold for selective mesh refinement. Finally, all the steps touched upon previously are integrated into the workflow and a visual illustration of it is presented.

4.1. Steps in a typical wind turbine wake simulation

In order to run Large Eddy Simulations on wind turbine wakes using ALM, typically, the following steps need to be followed:

- The external flow is generated by either synthetic methods or a precursor simulation as discussed in Chapter 3. If a number of inflow conditions are to be studied, then different simulations must be setup for each case.
- The mesh requires special consideration to ensure that the wake region is sufficiently resolved. If the cell size here is not small enough, a number of phenomena, like the helical vortex structure, cannot be simulated. Additionally, the refined region should be optimal such that the wake is completely encapsulated at all times while minimizing the over-refinement.
- After the turbines are added to the domain, the solution must be re-converged. If the time-averaged statistics are required, a new simulation must be launched after discarding the start-up transients. When a number of layouts are to be studied, the previous two steps may need to be repeated each time.

These simulations usually occur on a high performance computing (HPC) cluster. Thus, they are allocated a fixed amount of time for which they can continuously operate on the computational nodes.

Once this limit is exceeded, they may need to be relaunched manually. Thus, it can be inferred that repeating these steps for many different cases can be a tedious task requiring significant amount of human attention. Given the large amount of data and the difficulty of interfacing with HPC clusters, bugs are also unpreventable. This can put the reliability of the results under doubt.

The solution is then creating a workflow that automatically links all the aforementioned steps. The inputs can be provided through a more user-friendly interface and a workflow manager can efficiently relaunch and track all the different simulation runs. Once the workflow is tested for a particular case, all subsequent instances can be judged to provide trustworthy results.

Hence, this chapter aims to develop a workflow which can handle the aforementioned tasks. But first, the issue of wake tracking and mesh refinement needs to be addressed.

4.2. Wake tracking method

In the context of Actuator Line Large Eddy Simulations of wind turbine wakes, a mesh resolution of 64 cells per rotor diameter is set as the minimum requirement for sufficient computational fidelity [24]. The issue then becomes one of achieving this mesh size in the spatial location of the wake. But this is difficult to predict accurately beforehand, given the stochastic nature of wake meandering. A solution is using precursor simulations on a coarser grid to “flag” the wake and then adapt the mesh accordingly. Another solution, which is more commonly used, involves defining refinement zones within which a constant cell size is achieved, as shown in Fig. 4.1. But in order to be confident of enveloping the wake at all time-steps, the refinement zone has to be very wide and this results in an excessively large mesh. On the other hand, with a precursor simulation and a robust wake flagging method, the wake can be enveloped at all times while limiting the number of cells in the mesh. A number of possibilities exist for the choice of the wake flagging method. For example, the mesh can be adapted in the region where the velocity is below a certain threshold or the turbulence intensity is above a certain value. But when using turbulent inflow, the mesh adaptation routine may spuriously “flag” cells outside the wake. Moreover, since the turbulence intensity is highly sensitive to the mesh, the spatial location of wake can be quite different post-refinement, meaning a number of iterations would be required before a “converged” mesh is obtained. Thus to flag the wake in a conservative and robust manner, level-set functions will be used. They have an added advantage of being tested and widely used in YALES2 [88], in the context of tracking the liquid-gas interface in simulations of combustion and spray-atomization. But they also offer an efficient method of tracking wind turbine wakes [89, 36]. Herewith follows a brief discussion of the implementation of level-sets in YALES2.

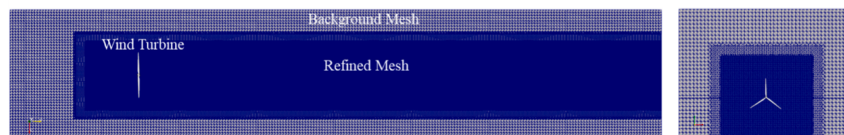


Figure 4.1: Mesh refinement on a structured grid using refinement zones- from Figure 9 pg. 9 of *Numerical investigations of coupled aeroelastic performance of wind turbines by elastic actuator line model* by J. Zheng et al. [62]

4.2.1. A conservative level-set approach

The level-set $L_c(f)$ of a function f is defined as a set on which the function takes up constant values, c , such that:

$$L_c(f) = \{(x_1, \dots, x_n) \mid f(x_1, \dots, x_n) = c\}. \quad (4.1)$$

In the context of fluid simulations, level-sets can be used to rigorously define boundaries and iso-contours. For example, in simulations involving two-phase flows, a level-set can be used to track the gas-liquid boundary. Indeed level-sets can be subjected to the same physics as any scalar field advected by the fluid flow.

The following hyperbolic tangent profile is used to define the level-set:

$$\psi(\mathbf{x}, t) = \frac{1}{2} \left(\tanh \left(\frac{\phi(\mathbf{x}, t)}{2\varepsilon} \right) + 1 \right), \quad (4.2)$$

where $\phi(x, t)$ is the signed distance function:

$$|\phi(x, t)| = |\mathbf{x} - \mathbf{x}_\Gamma|, \quad (4.3)$$

and \mathbf{x}_Γ is the closest point on the interface from \mathbf{x} . The interface itself can be located at a value of $\psi = 0.5$. The profile is defined such that inside the wake, ψ asymptotically reaches 1, while outside, it converges to 0. The level-set is then transported by the fluid field by the classic convection-advection equation:

$$\frac{\partial \psi}{\partial t} + \nabla \cdot \mathbf{u} \psi = 0, \quad (4.4)$$

where \mathbf{u} is divergence-free. But this will result in the distortion of the original hyperbolic tangent profile [88], requiring a resharpening via:

$$\frac{\partial \psi}{\partial \tau} + \nabla \cdot (\psi(1 - \psi)\mathbf{n}) = \nabla \cdot (\epsilon(\nabla \psi \cdot \mathbf{n})\mathbf{n}), \quad (4.5)$$

where τ is pseudo-time, \mathbf{n} is the normal vector to the level-set surface and ϵ is the thickness of the profile. This ensures that the volume within the level-set boundaries is conserved, which is a requirement for accurately tracking the wake. After a sufficient number of fluid iterations, the instantaneous level-set field can be visualized in Fig. 4.2.

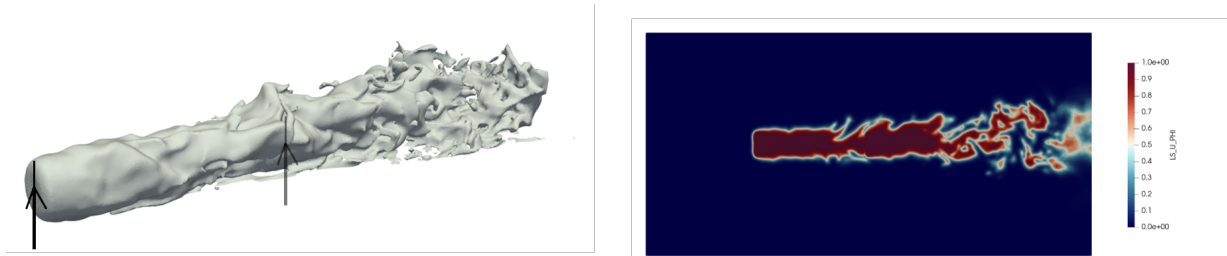


Figure 4.2: Left: iso-contour on the instantaneous level-set field at a value of 0.5 showing its evolution with the flow. Right: Top view of the level-set field on a plane at hub-height.

4.3. Mesh refinement procedure

The goal of flagging the wake using level-sets is to create a parameter which forms the basis of selective mesh refinement. But the field shown in Fig. 4.2 is still not sufficient to achieve this aim. Before an explanation of the procedure to build this parameter, a brief note on the mesh adaptation routine, MMG3d [33], is provided.

The MMG platform is an open-source library of software for mesh adaptation, iso-value discretization and Lagrangian movement algorithms. Mesh adaptation is achieved by importing a coarse initial mesh and specifying the required cell size at each node. Then, the routine interpolates the node-data to the edge and iteratively tries to achieve the user-specified target while respecting the growth-rate between regions of different refinement. The algorithm converges once the error between the actual cell size and the user specified target falls below the defined limit. Thus, MMG is useful in applications where the mesh must be refined using a property of the flow itself. In the present case, the target cell size will be defined using the parameter, Metric Flag (F_m), build using the precursor simulation and the level-set. The mesh before refinement is shown in Fig. 4.3. The cell size at the bottom is $\frac{D}{8}$ m while that at the top of the domain is $\frac{D}{4}$ m with a linear interpolation along the z-direction. The region around the turbines has a finer cell size of $\frac{D}{16}$ m to allow for accurate interpolation of the injected turbulence since a synthetic Mann box is used here. Lastly, the area close to the outlet is coarsened to reduce the total number of elements.

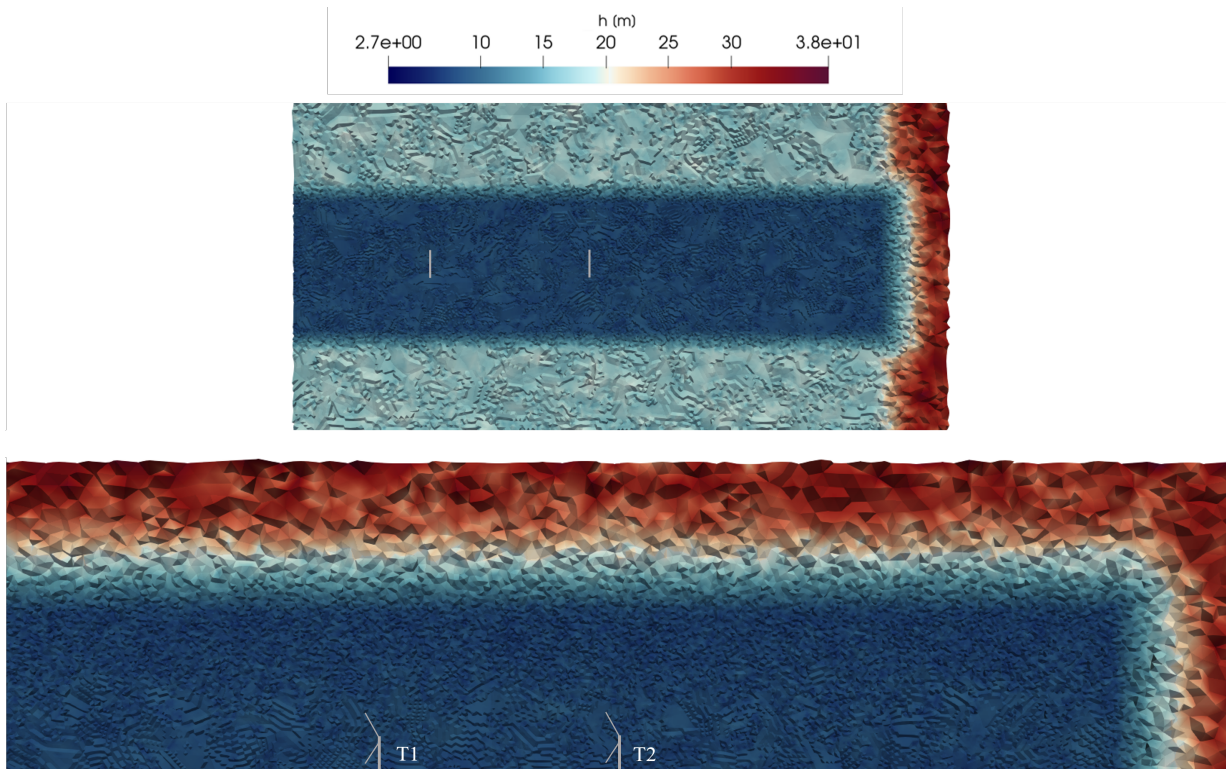


Figure 4.3: The mesh before the refinement procedure is implemented. Top: the iso-contours of the cell size (h) in meters on a horizontal plane at hub height. Bottom: the same but on a vertical plane passing through the rotor centers.

The procedure for mesh refinement is as follows:

- A coarse unstructured mesh (from ANSYS Meshing) is imported and the level-set is initialized from the rotor area.
- The following variable is computed on each node:

$$\phi_*(\mathbf{x}, t) = |\psi + \min(\phi(\mathbf{x}, t), c)| \quad (4.6)$$

where c is less than the turbine radius and ϕ is the distance from the level-set front as computed by Eq. (4.3). The motivation behind computing ϕ_* is to recalculate the distance from the level-set while ensuring the nodes outside the bandwidth have a value set to 0. For the purpose of conservatively enveloping the wake, it is desired to refine the region “inside” the level-set as well as the region within one turbine radius “outside” it. For this, $\phi(\mathbf{x}, t)$ is useful but it is only computed within the vicinity or bandwidth of the level-set. Everywhere else, it is set to 0. Thus, ϕ_* helps filter out the region far-away from the level-set.

- At all nodes, a new variable, F_m , is defined such that:

$$F_m = \begin{cases} 1 & \text{if } 1e^{-6} < \phi_* < \frac{D}{2} \\ 0 & \text{otherwise.} \end{cases} \quad (4.7)$$

- Then, the time-averaged statistics are collected on F_m . This results in Fig. 4.4 where iso-surface of $\langle F_m \rangle$ is shown on a vertical slice passing through the rotor centers.
- The nodes where $\langle F_m \rangle$ is greater than a certain threshold ($t_{\langle F_m \rangle}$) are given a target cell size of $\frac{D}{64}m$. Then, the mesh adaptation routine is called. The final mesh that is obtained with a threshold of 0.4 is shown in Fig. 4.5.

The selection of $(t_{\langle F_m \rangle})$ is addressed in the next sub-section.

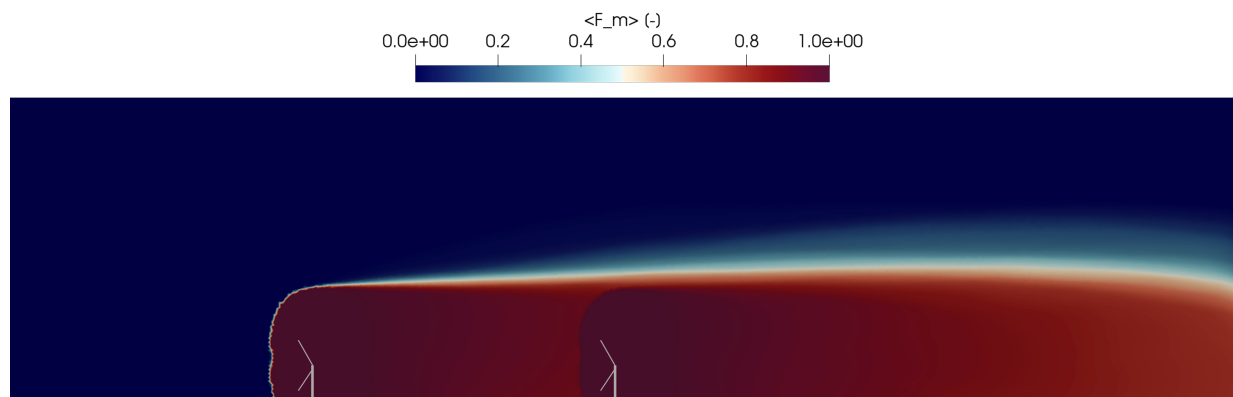


Figure 4.4: The iso-contours on the time-averaged Metric Flag $\langle F_m \rangle$ shown on a vertical slice of the domain.

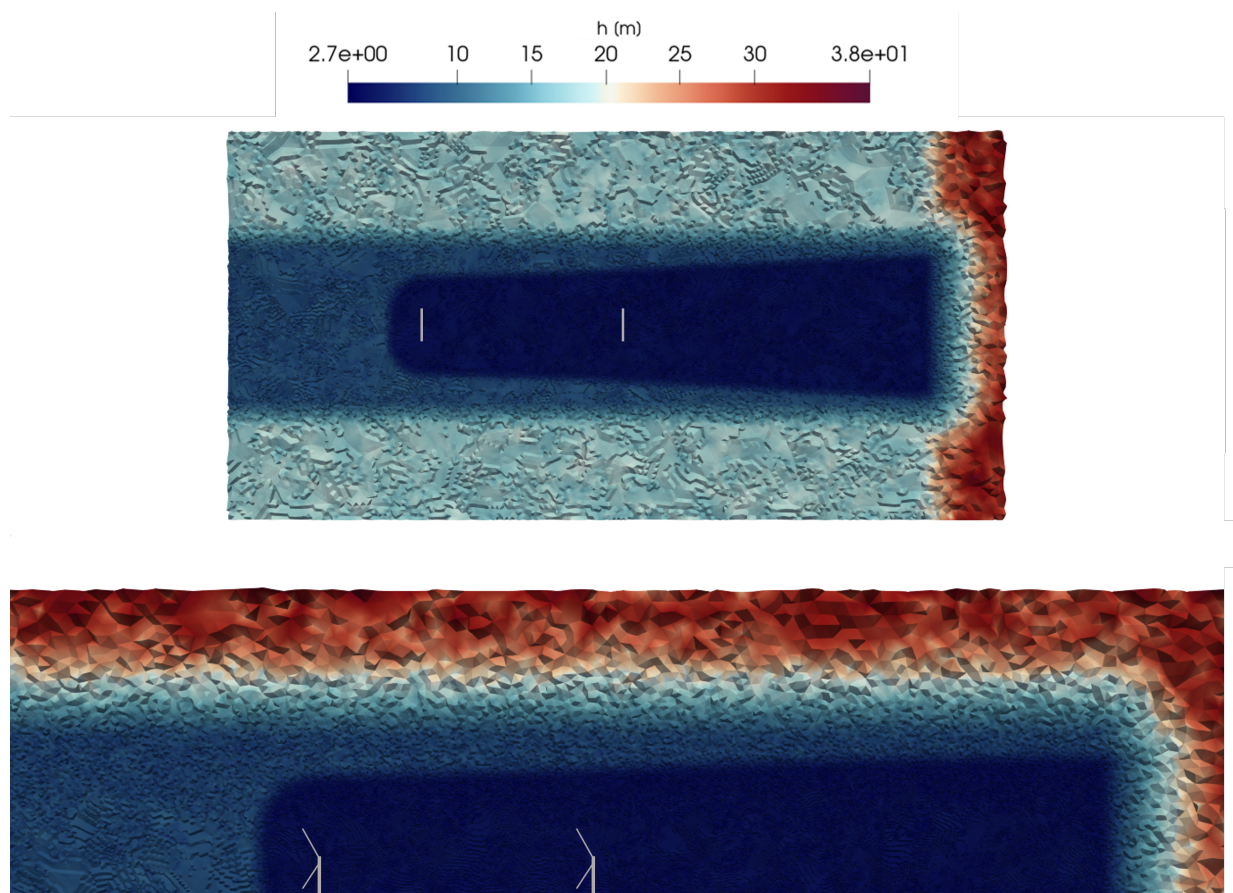


Figure 4.5: The mesh resulting from the refinement strategy presented in this subsection with $t_{\langle F_m \rangle} = 0.4$. Note that the cell size in the wake is $\frac{D}{32}$ m.

4.3.1. Towards an optimal threshold

The exact value of $t_{\langle F_m \rangle}$ has a crucial impact on the mesh size and thus the computational cost of the simulation. This can be verified from Fig. 4.6, where the mesh size and the resulting computational cost is shown for different values of the threshold. With a threshold of 0.01, the mesh size increases by almost

300% after adaptation. The resulting computational cost is approximately sixfold.

Fig. 4.7 shows the mesh obtained from two different values of $t_{\langle F_m \rangle}$. From this, it can be inferred that between a threshold of 0.01 and 0.9, the variation in the refinement zone is quite significant. In case of $t_{\langle F_m \rangle} = 0.9$, there can be instances wherein the wake meanders out of the refined zone. This can lead to discrepancies in the results. For example, if the cell size around the wake is not small enough, the turbulent mixing with the free-stream may not be accurately captured [24]. Subsequently, the wake recovery may be erroneously computed.

Thus, it is necessary to select a threshold value that provides a good trade-off between the computational cost and the reliability of the results. The latter is quantified by the error in the average stream-wise velocity and the turbulence intensity profiles, as compared to a reference case.

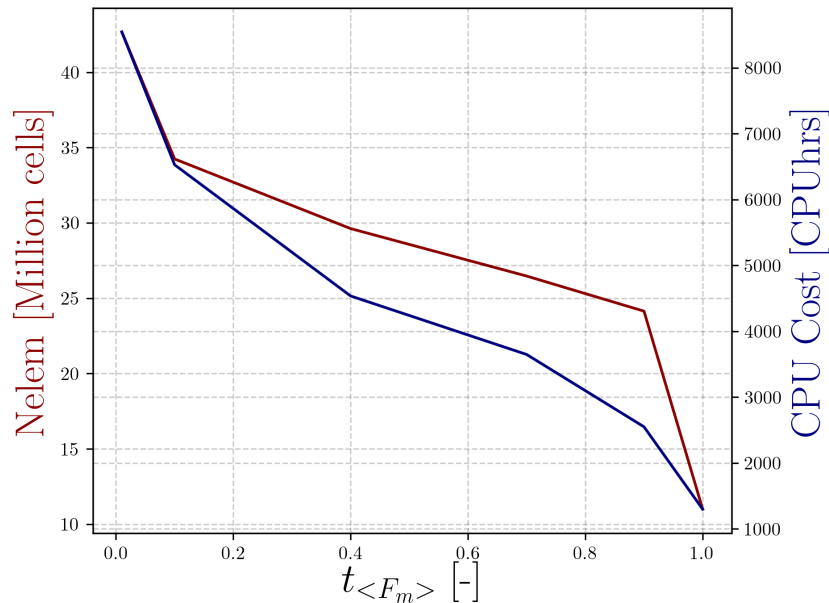


Figure 4.6: The variation in mesh size with $t_{\langle F_m \rangle}$ when starting from a mesh of 11 Million cells.

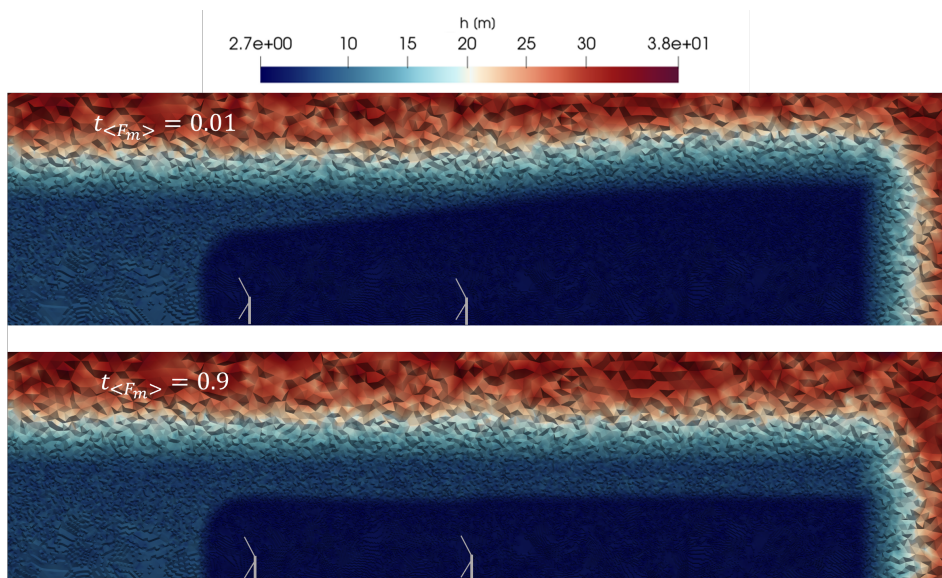


Figure 4.7: The comparison of the meshes obtained when using a threshold of 0.01 and 0.9 shown on a vertical slice passing through the rotor center for the case of two turbine operating in a line.

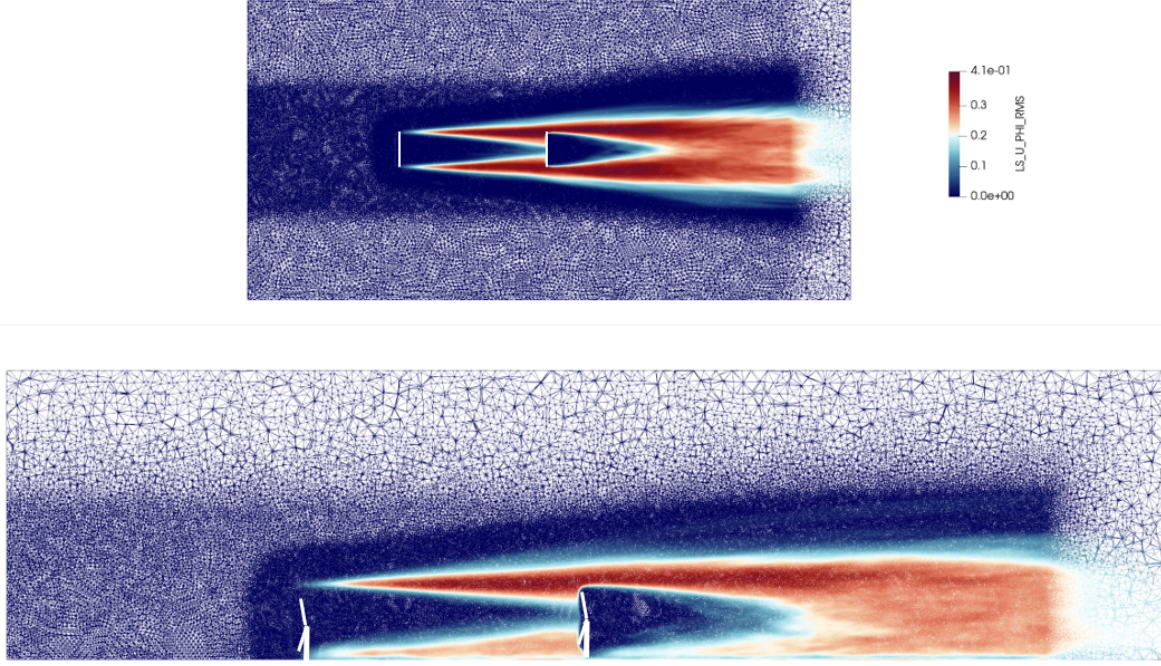


Figure 4.8: The root-mean-square of the level-set showing the extreme position of the wake on a vertical (bottom) and horizontal (top) slice at hub height computed on a mesh with $t_{\langle F_m \rangle} = 0.01$. All the values of $\psi_{RMS} > 0$ are inside the refinement zone.

Here, the case with $t_{\langle F_m \rangle} = 0.01$ is taken as the reference. The choice of using $t_{\langle F_m \rangle} = 0.01$ is justified since the refinement zone is large enough to account for any meandering of the wake. This can be verified from Fig. 4.8 which shows the standard deviation of the level-set. It is judged to be a good indicator of the extent of meandering since all points with $\psi_{RMS} > 0$ would be present inside the wake at a certain time-step. Thus, if the refined region completely engulfs all cells with $\psi_{RMS} > 0$, the wake will be well resolved. This is not the case for $t_{\langle F_m \rangle} = 0.9$ (refer Fig. 4.9).

The stream-wise velocity and turbulence intensity profiles along the vertical direction for different thresholds can be seen in Fig. 4.10 and Fig. 4.11. The former is in the near wake region 3D downstream of turbine T2 while the latter is in the far wake at distance of 7D. The error in the profiles with respect to $t_{\langle F_m \rangle} = 0.01$ is computed using the following relation and the results are present in Table 4.1. It is defined as:

$$\epsilon_r(\langle U_x(z) \rangle, t_{\langle F_m \rangle}) = \frac{\frac{1}{z_r} \int_0^{z_r} \left| \langle U_x^{0.01}(z) \rangle - \langle U_x^{t_{\langle F_m \rangle}}(z) \rangle \right| dz}{u_{ref}} * 100, \quad (4.8)$$

where z_r is the height of the refinement zone when $t_{\langle F_m \rangle} = 0.01$ as highlighted in Fig. 4.10 and u_{ref} is the time-averaged stream-wise wind speed at hub height of T1. Similarly, the error can also be computed for the profile of the turbulence intensity:

$$\epsilon_r(TI_x(z), t_{\langle F_m \rangle}) = \frac{\frac{1}{z_r} \int_0^{z_r} \left| TI_x^{0.01}(z) - TI_x^{t_{\langle F_m \rangle}}(z) \right| dz}{TI_{ref}} * 100, \quad (4.9)$$

where TI_{ref} is the stream-wise turbulence intensity averaged over the rotor-plane of T1.

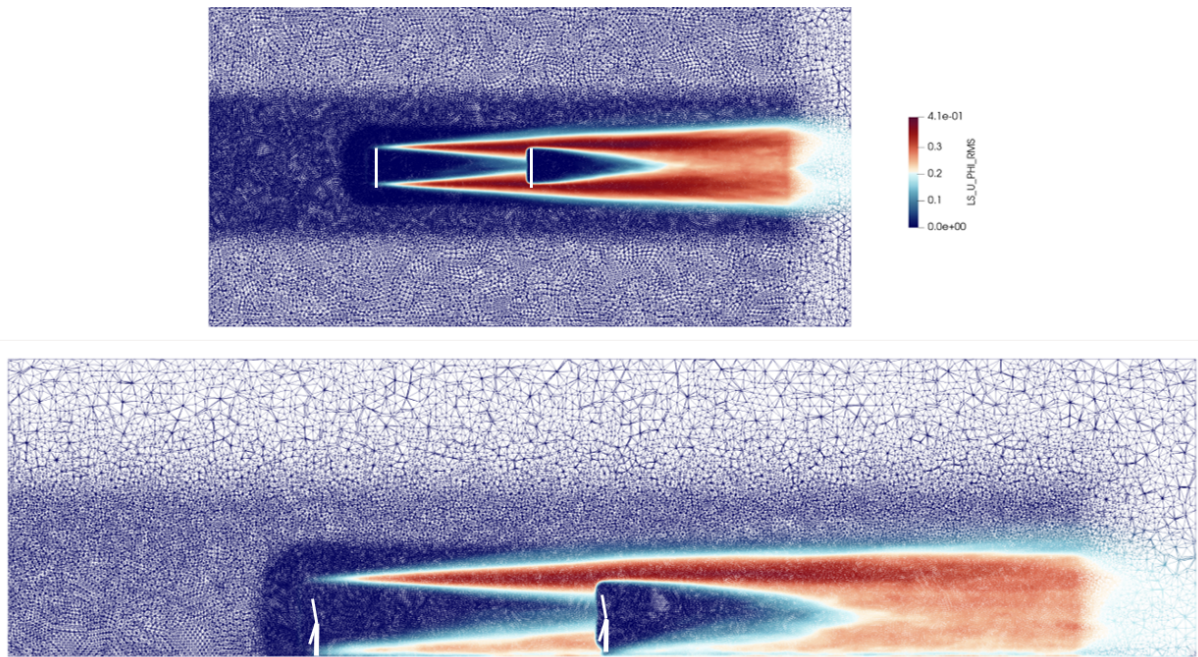


Figure 4.9: The root-mean-square of the level-set showing the extreme position of the wake on a vertical (bottom) and horizontal (top) slice at hub height computed on a mesh with $t_{(F_m)} = 0.9$.

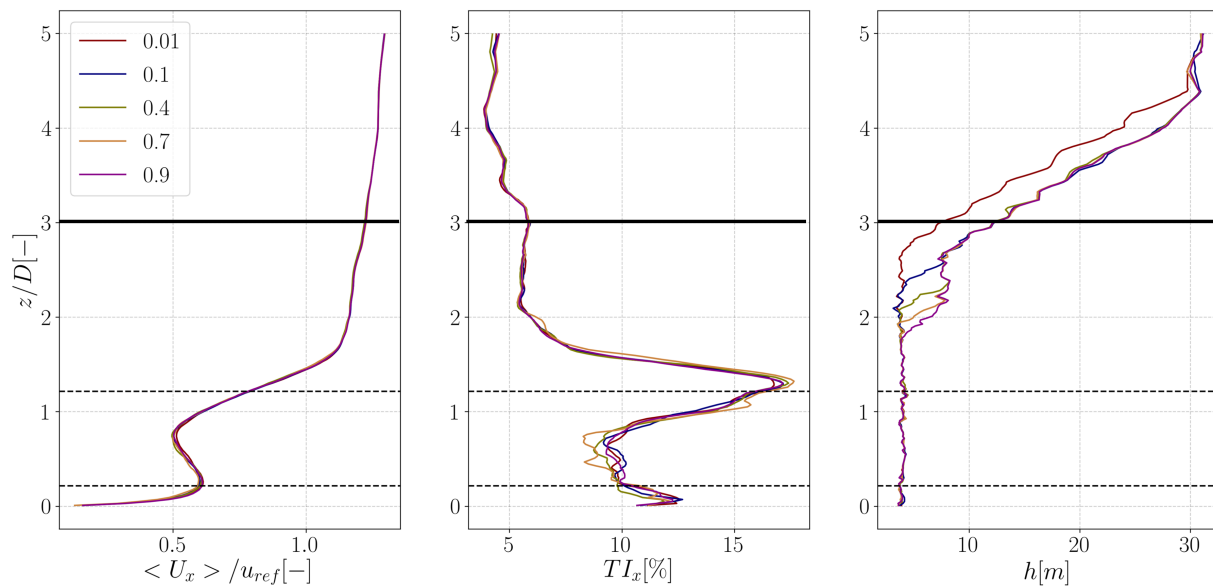


Figure 4.10: The vertical profile of the stream-wise time-averaged velocity (left), the stream-wise turbulence intensity (center) and the cell size (right) at a distance of 3D downstream of T2, with the different lines corresponding to values of $t_{(F_m)}$. The solid black line highlights the upper limit till where the error ϵ_r was computed and the dashed black lines indicate the turbine location.

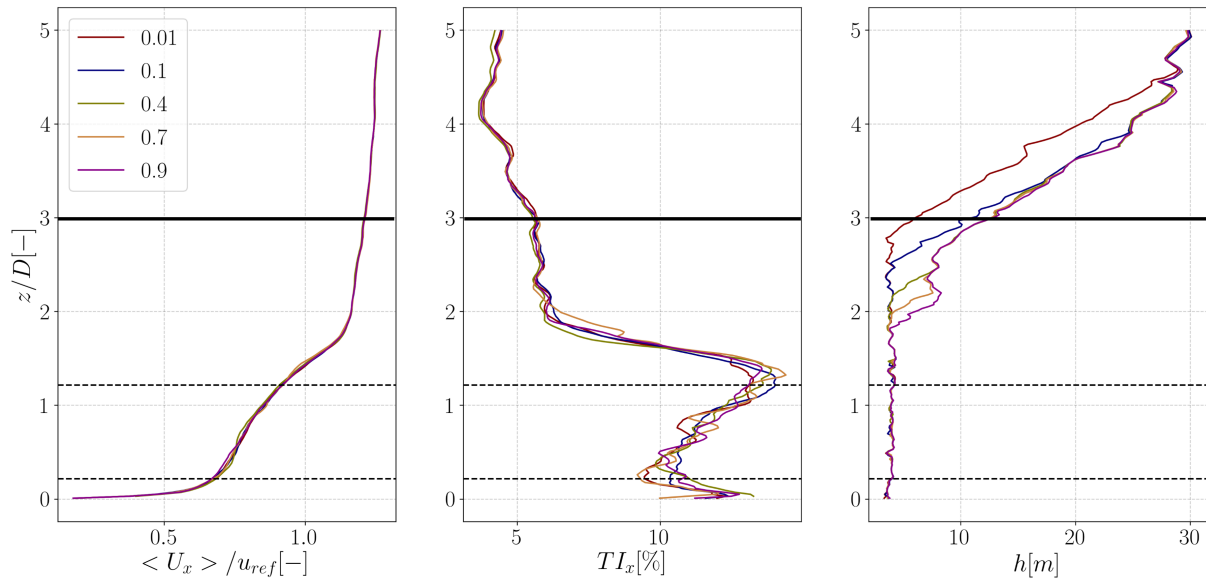


Figure 4.11: The vertical profile of the stream-wise time-averaged velocity (left), the stream-wise turbulence intensity (center) and the cell size (right) at a distance of 7D downstream of T2.

Table 4.1: Error in the $\langle U_x \rangle$ and $\langle TI_x \rangle$ vertical profiles for different thresholds

$t_{\langle F_m \rangle}$	$\epsilon_r(\langle U_x \rangle)$ [%] at 3D	$\epsilon_r(\langle U_x \rangle)$ [%] at 7D	$\epsilon_r(\langle TI_x \rangle)$ [%] at 3D	$\epsilon_r(\langle TI_x \rangle)$ [%] at 7D
0.1	0.67	0.71	4.9	5.9
0.4	0.76	1.41	5.2	6.0
0.7	0.78	0.96	7.9	7.2
0.9	0.82	0.92	6.4	7.9

From the results presented above, it can be concluded that the threshold value does not have a significant influence on the vertical profiles of the time-averaged statistics under consideration. The turbulence intensity does fluctuate more than the stream-wise velocity since the former is more sensitive to the mesh resolution. Additionally, ϵ_r is larger in the far wake region since the difference in the volume of the refinement zone, as compared to the reference case, is more at locations further downstream. For all five threshold values under consideration, the cell size in the “core” of the wake is the same. The difference exists in the peripheral region where the relevant physical phenomenon is the mixing of the wake with the free-stream flow. But as seen in the profiles in Fig. 4.10 and Fig. 4.11, the velocity field recovers at a similar pace for all thresholds, implying that on average, the turbulent mixing is sufficiently resolved even with a coarser mesh.

Now, as far as the choice of the optimal threshold is concerned, Table 4.1 suggests that even $t_{\langle F_m \rangle} = 0.9$ would provide adequate accuracy. But this is misleading. Firstly, the sensitivity study presented here is only carried out at one wind speed. Here, the turbines are operating in the above rated region where the thrust is low. Consequently, the difference in wind speed between the wake and free-stream flow is not as large leading to a faster recovery of the wake. But when operating at below-rated conditions, the increase in thrust delays wake recovery. This means that the same value of F_m will be less “spread-out” in the stream-wise direction for the below-rated wind speed than for the above-rated one, as is seen in Fig. 4.12. Thus, selecting a smaller value of $t_{\langle F_m \rangle}$ provides more robustness when different inflow conditions are to be simulated.

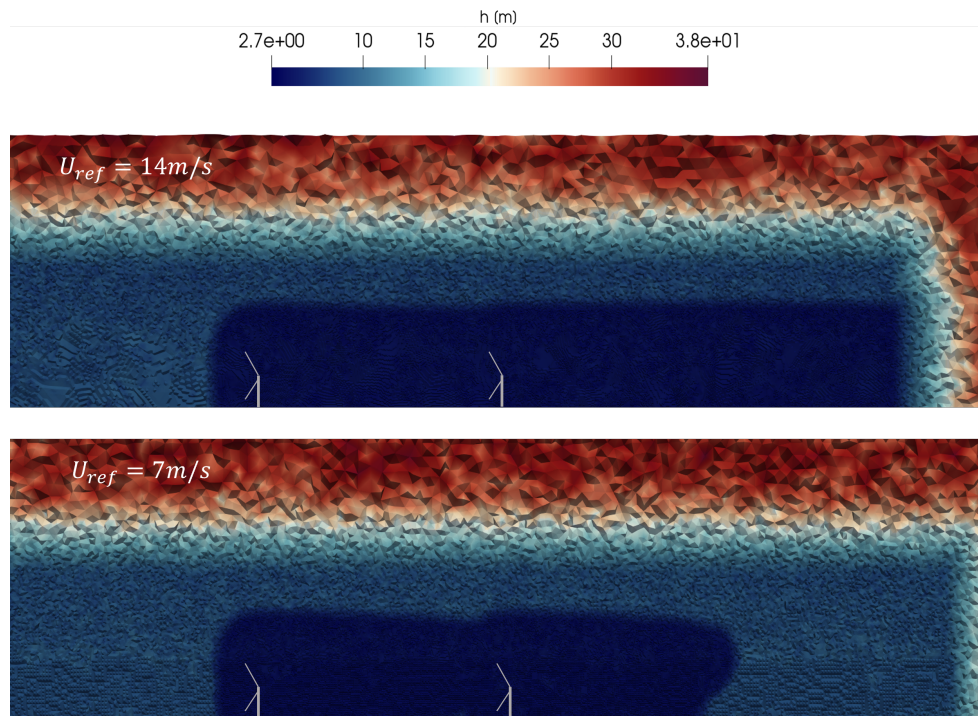


Figure 4.12: The iso-contour of the cell sizes on a vertical slice passing through the rotor centers, showing the difference in the resultant mesh when using the same threshold of 0.9 but for different inflow conditions.

Secondly, it is also important to mention that while in the scope of this project only the profiles of the time-averaged statistics were compared, the impact on higher-order turbulence characteristics or the wake properties such as the movement of the wake center would also be necessary for selecting the optimal threshold. Additionally, the impact on the instantaneous flow could be significant. Thus, considering the aforementioned points as well as the overarching requirement of carrying out an accurate and reliable simulation, a threshold of 0.1 is conservatively selected for all subsequent cases.

4.4. Workflow for studying wind turbine wake interactions

Now, all the steps required for obtaining the instantaneous and time-averaged solution from coupled ALM-LES can be integrated into a workflow, which is shown in Fig. 4.13. Here, the workflow is applied to the case of three turbines in-line.

The steps are as follows:

- 0) The initial and boundary conditions are specified along with the numerical settings of the solver, turbine type, layout, etc.
- 1) The external flow is initialized using the recycling method of turbulence generation. Here, a previously computed solution is used and hence the target wind speed and turbulence intensity can be selected.
- 2) A precursor simulation is started to flag the wake while the turbines are introduced into the domain as actuator lines. Level-set functions initialized from the rotor plane are used to identify the spatial and temporal location of the wake.
- 3) After the wake flow is converged, F_m is computed on all the nodes and its time-averaged statistics are accumulated to flag the mean wake location.
- 4) The mesh is refined within the flagged region based on the value of $t_{\langle F_m \rangle}$ and user-specified cell-size. In this case, it is $\frac{D}{64}$.
- 5) The wake is re-converged with the new mesh and the coupling is turned on.
- 6) The final time-averaged statistics are accumulated.

It is important to underscore that the user only needs to provide the inputs such as the turbine model, layout, inflow conditions, yaw offsets, level of refinement, etc before launching the workflow. Everything else is accomplished automatically. Moreover, the mesh strategy ensures the reliability of the results since the wake is sufficiently refined even when changing the layout or yaw offset.

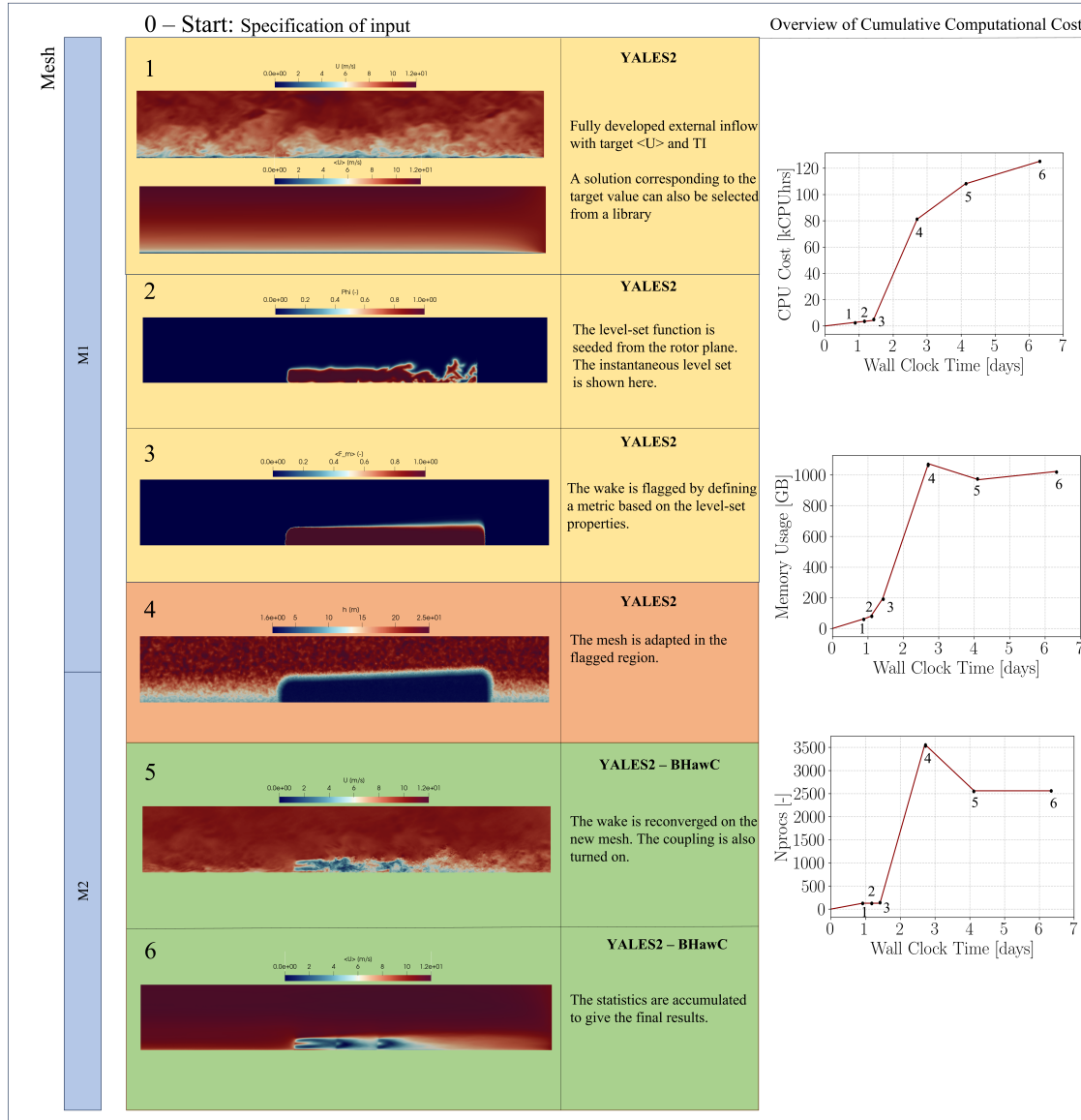


Figure 4.13: A example of a workflow from start to finish. The slices of the domain are taken on a vertical plane passing through the rotor center.

From right hand side of the figure, it can be observed that external flow generation and wake-flagging are relatively inexpensive as compared to the subsequent steps of the workflow. Indeed, most of the computational costs are incurred during and after mesh refinement as the cell count increases significantly. In terms of the wall-clock-time, steps 5 and 6 require around 3 days to complete. This is mainly due to the reduction in the time-step caused by the coupling.

The advantage of using the workflow is also evident from the steady rise in the consumption of the CPU resources. Here, each subsequent simulation is started as soon as its predecessor is finished without any loss of human-time. Thus, the requirement of continuous setup and monitoring inherent in many LES

studies is nullified. Now, with adequate computational resources, parametric studies of wind turbine wakes are achievable. This forms the topic of the subsequent chapters.

Impact of inflow on multi-wake interaction

This chapter is dedicated to a study of the three turbine in-line configuration under varying inflow conditions with the aim of analysing the impact on wake recovery, meandering and power production. The workflow shown in Chapter 4 is used for automatically setting up cases for three different wind speeds and two turbulence intensities selected from the parametric study of Chapter 3. The chapter is ordered as follows. First, the domain setup and boundary conditions are presented to provide an overview of all the simulated cases. Next, the results for different wind speeds and turbulence intensities are shown. The discussion focuses mainly on characterizing the properties of the wake. This includes the time-averaged velocity and turbulence intensity profiles, power production, the wake recovery distance, wake center position and meandering frequency.

5.1. Simulation setup

5.1.1. Industrial wind turbine model

In this study, the SWT-6.0-154 wind turbine will be used. It is an offshore turbine with a rated power of 6MW and a rotor diameter of 154m. The turbine is installed in a number of offshore wind farms in Europe and Asia. While the hub-height is site-dependent, in this study a value of 105.52m will be used. The rated wind speed is approximately 12m/s. Due to confidentiality reasons, the blade, nacelle and tower geometries are not given. All the results are also normalized. The control behaviour is same as that of the actual turbine, as a result of the coupling with BHawC.

5.1.2. Domain and turbine configuration

The domain and turbine configuration under study is shown in Fig. 5.1. The domain size is the same as that used for the parametric study from Chapter 3 such that: $L_x \times L_y \times L_z = 49D \times 10D \times 6D$. The turbines are separated by a distance of 4D. The recycling region is 21D in length while the outlet is 15D from the last turbine. The center of the first turbine is at (0, 0, 105.52m). The recycling plane is kept 5D upstream of the first turbine to ensure that the induction effects are not recycled as well.

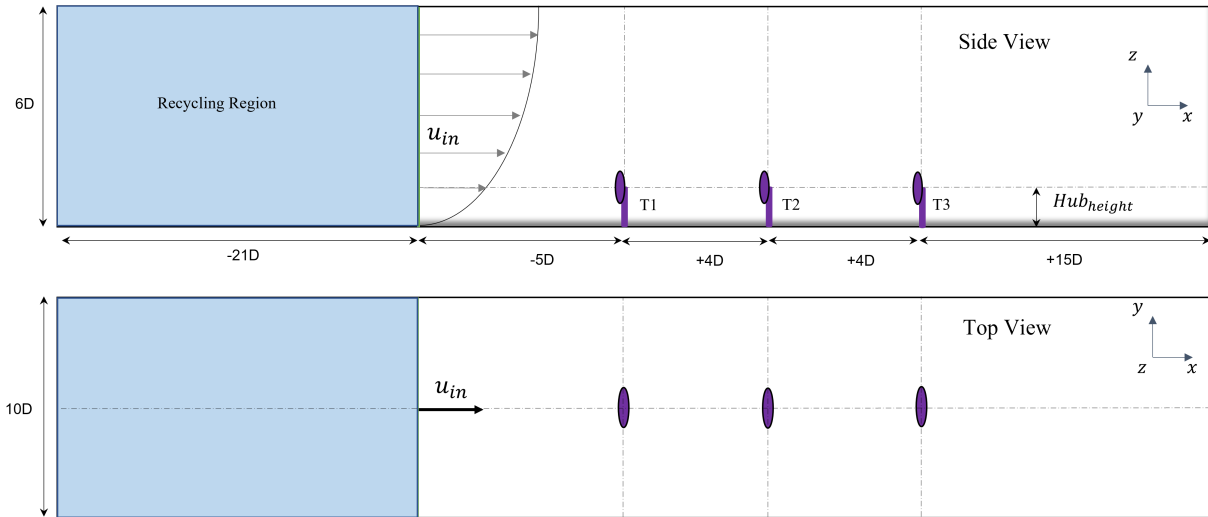


Figure 5.1: Top: Side view of the simulated domain showing the turbine separation and relative size of the recycling zone. Bottom: Top view of the same domain.

5.1.3. Boundary conditions and solver settings

For three wind speed and two TIs, the six combinations of inflow conditions selected from the recycling parametric study are shown in Table 5.1.

Table 5.1: The inflow conditions used for the parametric study

Case No.	Target $\langle U_x \rangle$ at hub (m/s)	Actual $\langle U_x \rangle$ at Hub (m/s)	Target TI_x (%)	Actual Rotor-Averaged $TI_{x,y,z}$ (%)	Shear Coefficient (-)
1	8.0	8.3	5	5.3, 3.7, 3.1	0.07
2	12.0	12.4	5	5.7, 3.9, 3.1	0.09
3	14.0	14.3	5	5.3, 3.7, 3.3	0.07
4	8.0	8.8	10	10.3, 7.5, 6.1	0.13
6	14.0	14.5	10	10.5, 7.5, 6.3	0.14

The wind speeds correspond to below-rated, rated and above-rated operation of the turbine while a large TI range is selected, such that its impact can be clearly observed. The variation in the wind speed at hub as compared to the target values are small and are not expected to have a significant effect. Note, in the subsequent sections, the cases will be referred to by the target wind speeds and TIs.

The boundary conditions on the domain walls are shown in Table 5.2. The numerical details of recycling are not shown here as they are well covered in Chapter 3. The solution is initialized with the data from the last time-step of the corresponding run in the parametric study of Chapter 3. Thus, the external flow is assumed to be converged. The flow-rate and the ground roughness are also unchanged from the respective run of the parametric study.

Table 5.2: Boundary conditions on each wall of the domain

Wall	Boundary condition
Inlet	recycling with Q and z_0 based on the required inflow
Outlet	Constant Outflow
recycling Zone Side Walls	Periodic
Actual Domain Side Walls	No-Slip
Bottom Wall	Wall Law
Top Wall	No-slip

Finally, the YALES2 Incompressible Flow Solver settings are shown in Table 5.3. The fluid density (ρ) is equal to 1.225 kg/m^3 while the kinematic viscosity is $1.1517 \times 10^{-5} \text{ m}^2/\text{s}$, which are close to their respective ambient values. The mesh size corresponds to the final two runs of the workflow shown in Fig. 4.13. The time step is equal to 0.02s to ensure that the structural solver does not diverge. For the YALES2 standalone runs of the workflow, it is determined by the CFL limit. The time integration is achieved with the TFV4A scheme [37]. A cell size of $\frac{D}{64}$ results in 32 mesh elements per blade which is sufficient to meet the guidelines for the Actuator Line [24]. The blade is itself defined by 75 actuator points. The resulting mesh is shown in Fig. 5.2. The Dynamic Smagorinsky model is used since the YALES2-BHawC coupling has been validated using this sub-grid model [74]. The wake is converged in a time of $\frac{30D}{u_{ref}}$ sec since this is the length of the actual domain (without the recycling region). The statistics are accumulated for $1.5\times$ longer than the convergence time.

Table 5.3: Solver settings and other relevant details of the simulation

Metric	Value
Spatial Integration	4^{th} order
Temporal Integration	4^{th} order
Sub-Grid Model	Dynamic Smagorinsky
Mesh Elements per Blade	32
$\frac{\epsilon}{h}$	2
Mesh Size (M2 in the workflow)	400 - 550 Million
Convergence Time	$\frac{30D}{u_{ref}}$ sec
Statistics Accumulation Time	$\frac{45D}{u_{ref}}$ sec

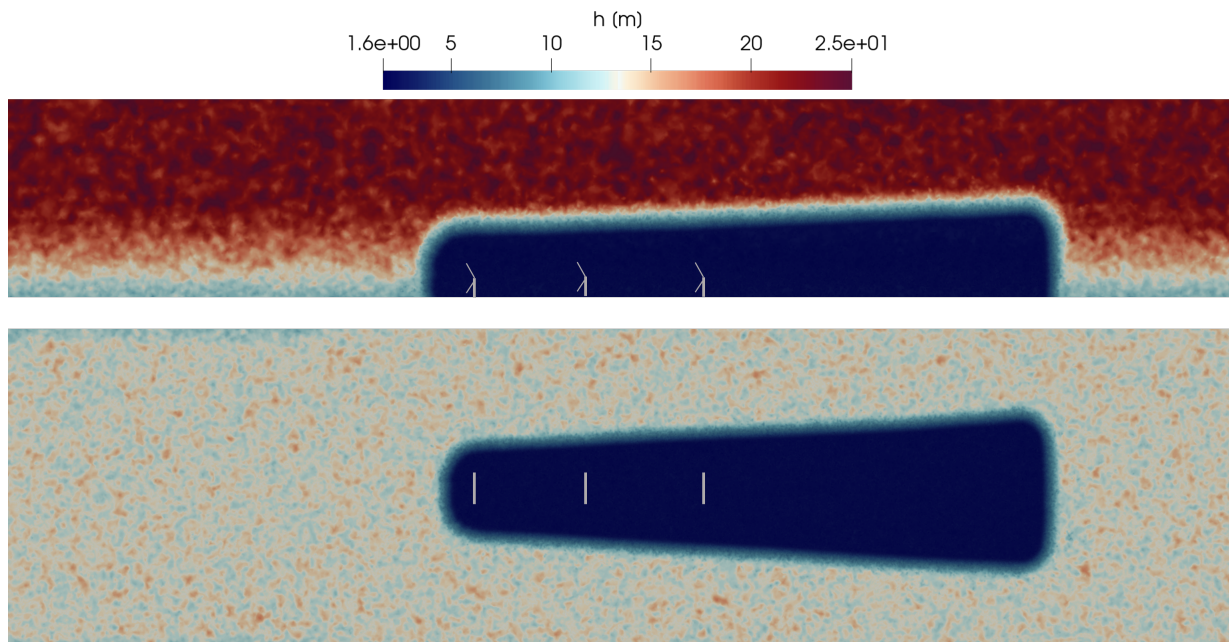


Figure 5.2: Top: Side-view of the mesh on a vertical plane passing through the rotor center wherein $u_{ref} = 8 \text{ m/s}$ and $TI_{ref} = 5\%$. Bottom: Top-view of the mesh on a plane at hub-height.

Since a constant outflow boundary condition is used, it must be ensured that there is no backflow at the outlet. This is achieved by the use of a sponge layer within which a damping term is introduced in the local momentum equations. As a consequence, any vortices approaching the outlet are consequently damped out. Additionally, the outlet is sufficiently far post-processing region and outlet boundary condition is not expected to introduce errors into the results shown here.

The influence of the tower and nacelle is modelled in a manner similar to that of the Actuator Line Method for the blades. The tower geometry is represented by actuator points where the drag force is interpolated from a lookup table. For this, the incident velocity slightly upstream the actuator element is used, to avoid induction effects. In this case, the tower modelling methodology differs from that of Churchfield et al. [50]. The resultant force is then mollified on to the mesh using a 3D isotropic Gaussian kernel with $\frac{\epsilon}{h} = 2$. A slightly different approach is used for the nacelle wherein the force is divided into two parts corresponding to the front and side of the nacelle. The tower and nacelle are themselves treated as rigid bodies and the computed forces are not transferred to the structural solver. More information regarding the tower and nacelle modelling can be found in [36].

With respect to BHawC, the mesh is composed of 19 elements per blade. 8 elements and 15 nodes are used to define the tower, nacelle and hub. Gravity is enabled with an acceleration of 9.82 m/s^2 . During the first 200s of the simulation, damping is used to reduce the initial transient fluctuations. This prevents divergence of the solver when extreme flow variations are incident on the turbine structure. All the results presented here and in Chapter 6 are from the last simulation of the workflow. This corresponds to the accumulation of the final statistics.

5.2. Results

This section discusses the results of the parametric study. First, a comparison with a lower mesh resolution is presented to show that mesh independence has been achieved. Next, time-averaged velocity and TI profiles in the wake at various stream-wise locations are shown. This highlights the impact of varying wind speed and TI on the velocity field in the wake. This is further underlined by the time-averaged power output of each turbine which is subsequently presented. The wake recovery is also compared between the different inflow conditions. Then, a discussion on the wake center follows. Herein, the impact of the inflow TI on wake meandering is seen. Moreover, the correlation between the power output and the lateral position of the wake center is computed in the time domain.

5.2.1. Mesh convergence study

To evaluate the influence of the mesh resolution, the results for the inflow condition of 8m/s target wind speed at hub and 10% TI were compared for two different cell sizes in the wake: $\frac{D}{32}m$ and $\frac{D}{64}m$. Firstly, the profiles of $\langle U_x \rangle$ along the vertical direction are compared at two different stream-wise locations in Fig. 5.3. The slight mismatch in the profiles emanates from the difference in the number of samples used to obtain the time-averaged values. Due to its lower cost, the case with $\frac{D}{32}m$ was run for 1500s of physical time, while the one for $\frac{D}{64}m$ was run for 650s. The latter corresponds to approximately 100 revolutions of the rotor.

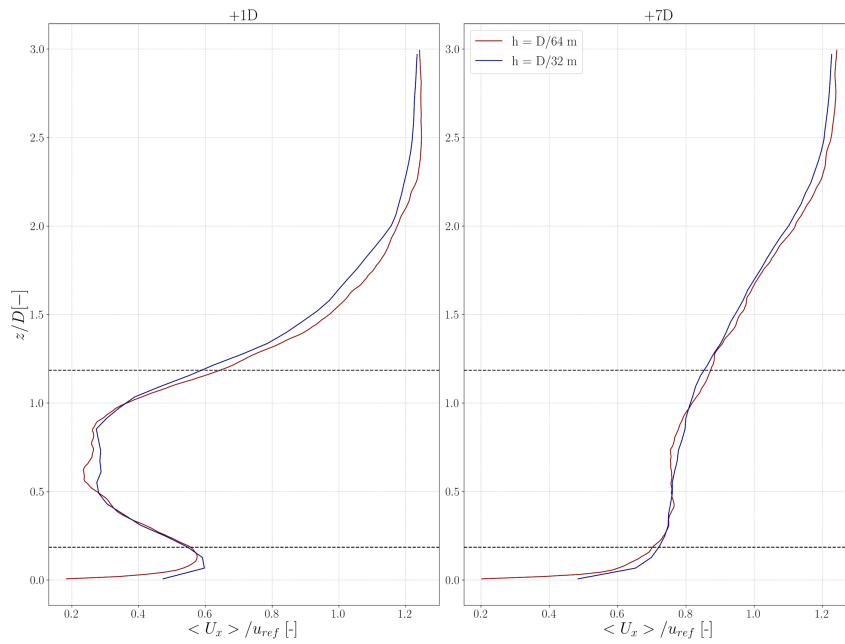


Figure 5.3: A comparison of the $\langle U_x \rangle$ profile along the z -direction in the wake of T3, at a distance of 1D and 7D from it.

Next, some of the output channels of the servo-elastic solver are compared in Fig. 5.4. Herein, the time-averaged results are shown for the electrical power output (P_{elec}), the rotation speed (ω) and the blade pitch angle (Ψ). These are less sensitive to the sample size since the industrial controller limits the fluctuations. In either case, there is good agreement for outputs of T1 which under the given inflow conditions operates at below-rated condition, thus producing around 50% of its rated power. Indeed all three turbines operate in the below-rated region. This is verified by the results for the pitch angle which shows that the blades of the three turbines are pitched in the same direction and approximately to the same value. Additionally, the rotational speed is proportional to the power output of the turbines in order to achieve the same tip speed ratio. These are the characteristics of torque-controlled turbines in partial load conditions.

The overestimation of P_{elec}^{T3} when using a lower mesh resolution is expected since this will reduce the mollification width (ϵ) [24]. Being in the wake of T2 and T3, it also experiences higher turbulence which exacerbates the errors produced by a lower value of ϵ . Fig. 5.5 elaborates on the comparison of P_{elec} for the two cases by providing the time signal and its Fourier transform. As seen in the time series, for the $\frac{D}{32}m$ case, the power output is consistently over-predicted by 15-20%. In the power spectra, the different peaks correspond to the harmonics of the blade passing frequency. These are typically observed as multiples of three for three-bladed wind turbines and are a consequence of the wind shear and tower shadow effects.

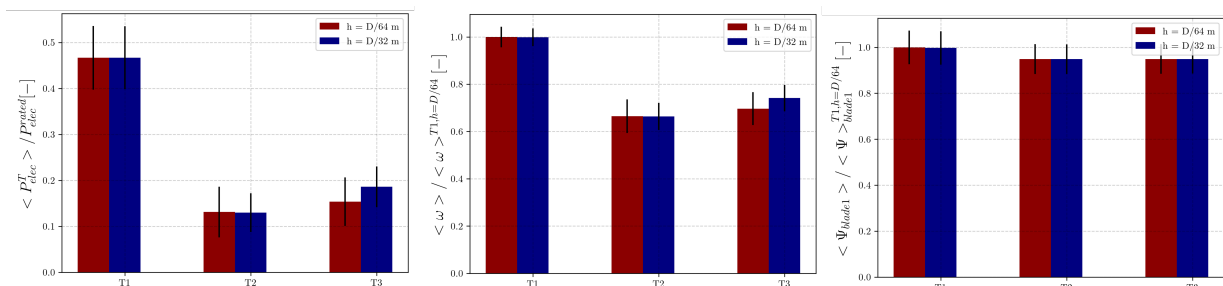


Figure 5.4: A comparison of the electrical power output (P_{elec}), the rotation speed (ω) and the blade pitch angle (Ψ) for all three turbines for different mesh resolutions. The error bars show the respective standard deviation.

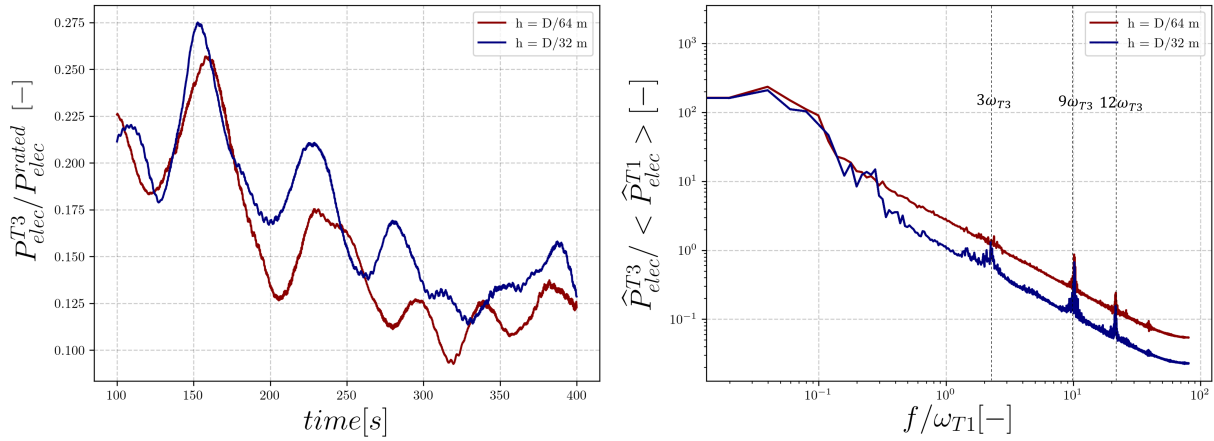


Figure 5.5: The sample of the time series of the power output of turbine T3 (left) for different mesh resolutions and its Fourier transform over the total physical time of the simulation (right).

It should be mentioned that a more thorough analysis would require a cell size of $\frac{D}{128} m$ to also be included. But this would result in a mesh approximately 8 times larger than that of $\frac{D}{64} m$ case. The cost of such a simulation, with more than 3 billion elements, would be prohibitively high. Moreover, given that the $\frac{D}{64} m$ is a standard for ALM-LES, there is a high degree of confidence that additional refinement in the wake is redundant. Thus, the subsequent results, especially with regards to the turbine outputs, are judged to be independent of the mesh.

5.2.2. Flow topology

In Fig. 5.6, the slice of the instantaneous field reveals some important features of the flow. Firstly, the effect of increasing the ambient TI is seen by the presence of stronger gusts. The wake has a coherent structure upto 2D behind T1. This represents the point where the helical vortices breakdown. The downstream turbines show no such structure since they operate in the wake of T3. Moving further downstream, the meandering of the wake starts to increase in amplitude.

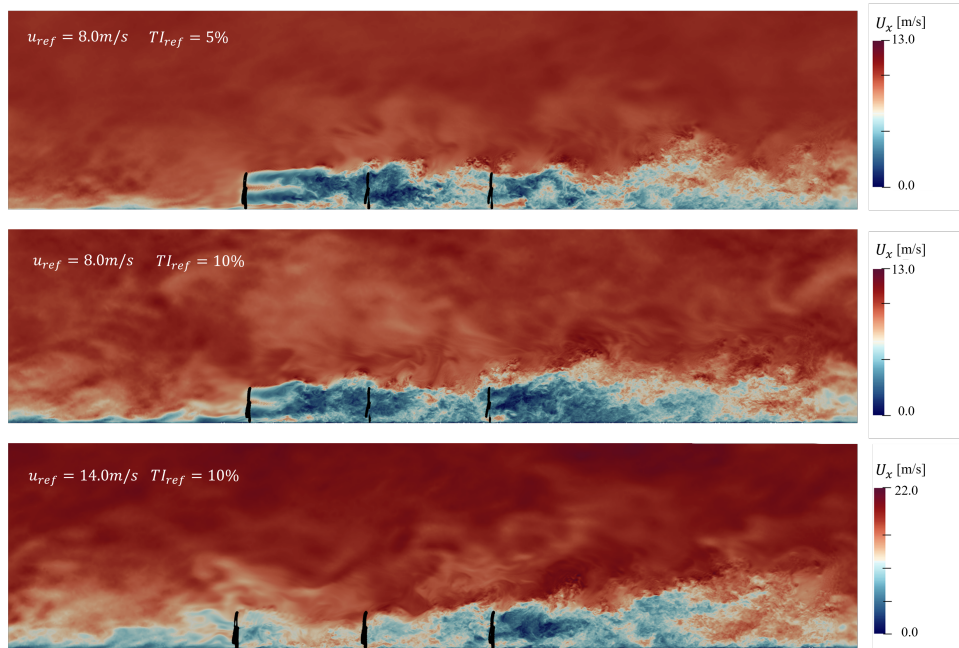


Figure 5.6: The instantaneous velocity field visualized on a vertical plane passing through the rotor center.

Fig. 5.7 shows the slice of the time-averaged velocity field. Here, it can be observed that the velocity in the wake behind T1 is lower for the 8m/s cases. This is due to the turbines operating in the partial load region wherein the thrust is high. The velocity deficit in the wake increases with the downstream distance, before starting to recover. The same trend is seen for the stream-wise turbulence intensity in Fig. 5.8 wherein more turbulence is initially present at the wake boundaries which then mixes with the wake core as the flow progresses further downstream.

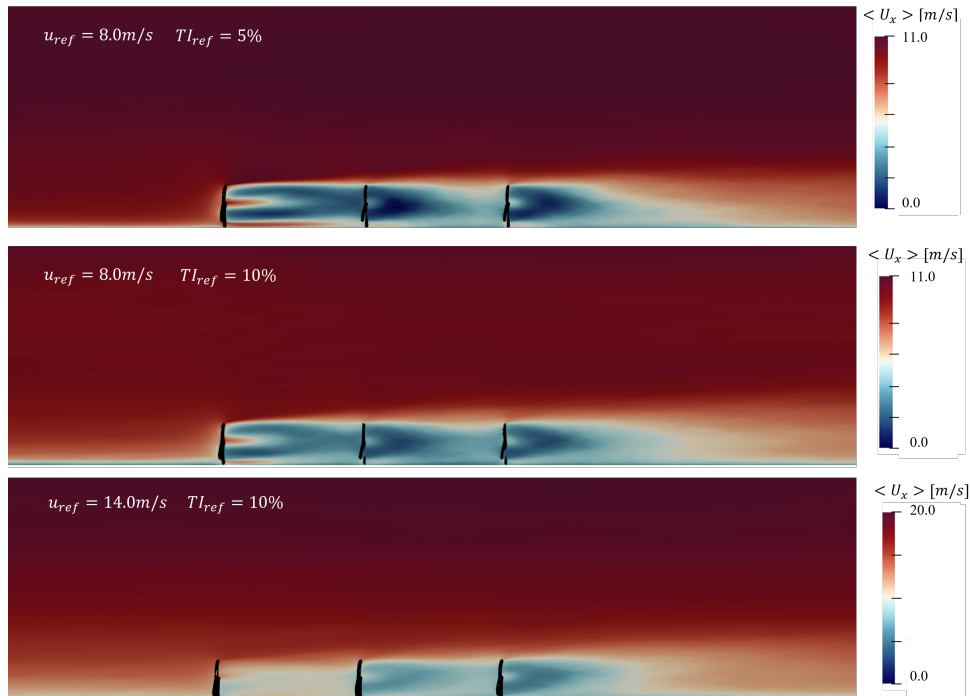


Figure 5.7: The time-averaged velocity field visualized on a vertical plane passing through the rotor center.

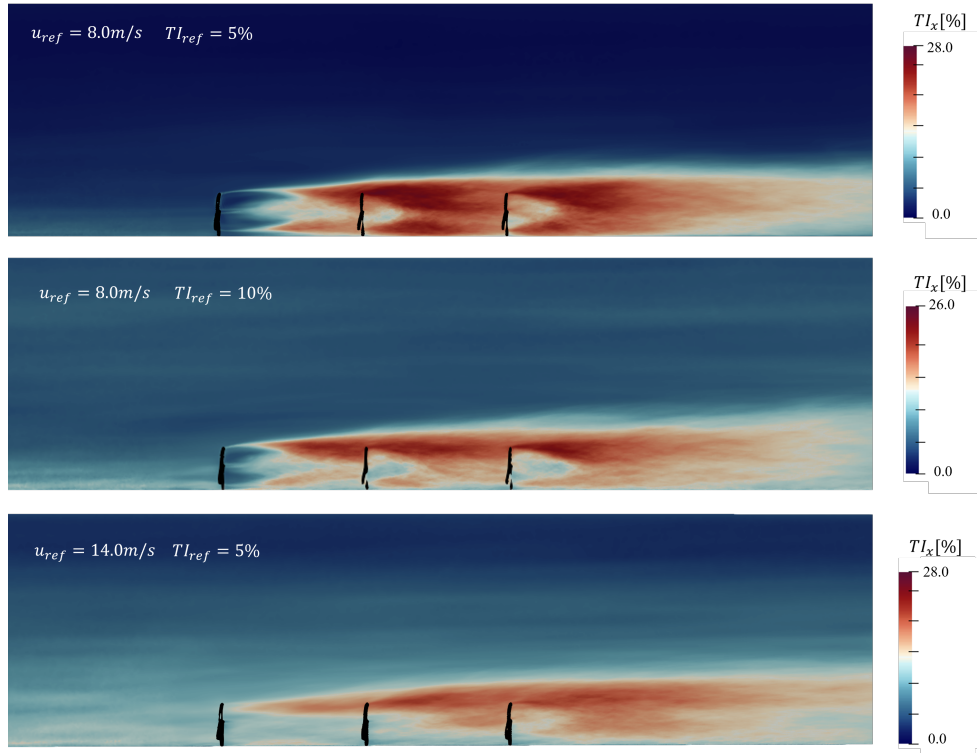


Figure 5.8: The turbulence intensity in the stream-wise direction visualized on a vertical plane passing through the rotor center.

This section also provides the profiles of the time-averaged flow in the wake region. Firstly, the vertical profiles of the time-averaged stream-wise velocity deficit are shown in Fig. 5.9. The deficit is computed with respect to the profile of $\langle U_x \rangle$ at $4D$ upstream of T1:

$$\Delta U_x(z) = \langle U_x \rangle_{x=+4D}(z) - \langle U_x \rangle(z) \quad (5.1)$$

In each case, the values of ΔU_x are normalized by the respective inflow velocity at hub height as stated in Table 5.1. A trend is seen wherein the deficit is highest at a distance of $1D$ from T3 for all inflow conditions. Then, as the wake progresses further downstream, it starts to recover. Simultaneously, the deficit spreads in the vertical direction. At a distance of $9D$ behind T3, the wake extends till approximately $2D$ from the ground. Here, the two TIs can be differentiated. For the 10% TI cases, the wake spreads further along the z -direction than for the 5% TI ones. Comparing the wake boundaries at $9D$ downstream of T3, a 25% increase is observed for the 10% TI cases. This is a direct consequence of more turbulent mixing in the free-stream region. It is seen that in all cases ΔU_x changes by 60% from $+1D$ to $+3D$. But from $+5D$ to $+9D$, the change in ΔU_x is 30%. This is because the rate of recovery is proportional to the amount of deficit. Another important aspect is that the recovery is triggered simultaneously in the top and bottom regions of the wake.

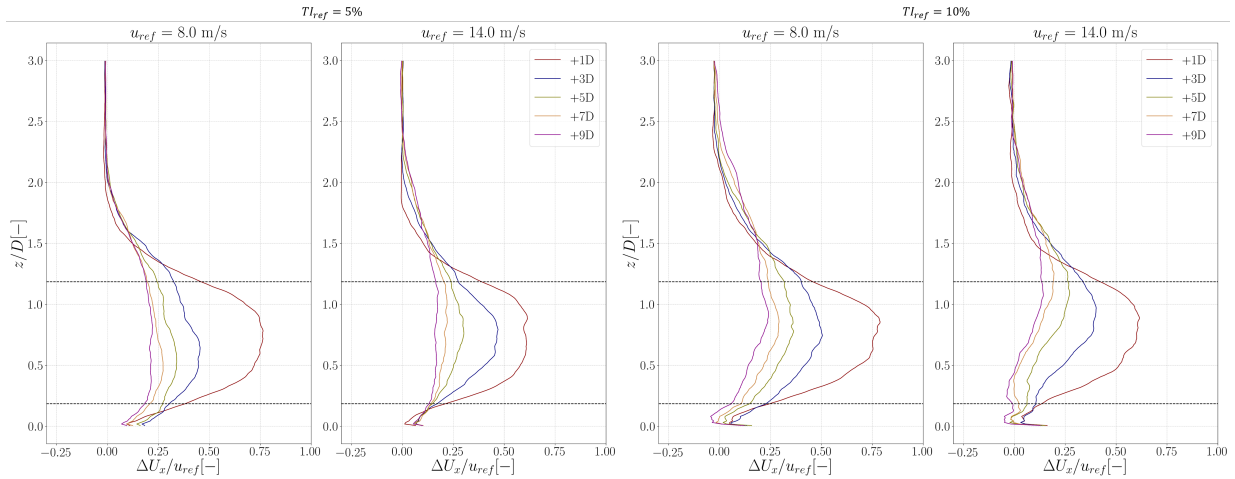


Figure 5.9: The profile of the time-averaged stream-wise velocity deficit along the z -direction at different stream-wise positions behind T3. Note, the points are sampled at $y = 0$ or along the center-line of the domain.

Next, the time-averaged stream-wise velocity deficit is plotted along the y -direction in Fig. 5.10. A slight asymmetry is seen which is an effect of the inflow being non-uniform as discussed in Chapter 3. The spreading of the wake can be easily observed from this view as well. At 9D downstream of T3, the wake has a width of 4D for the 10% TI cases, while it is 3D for the 5% TI cases.

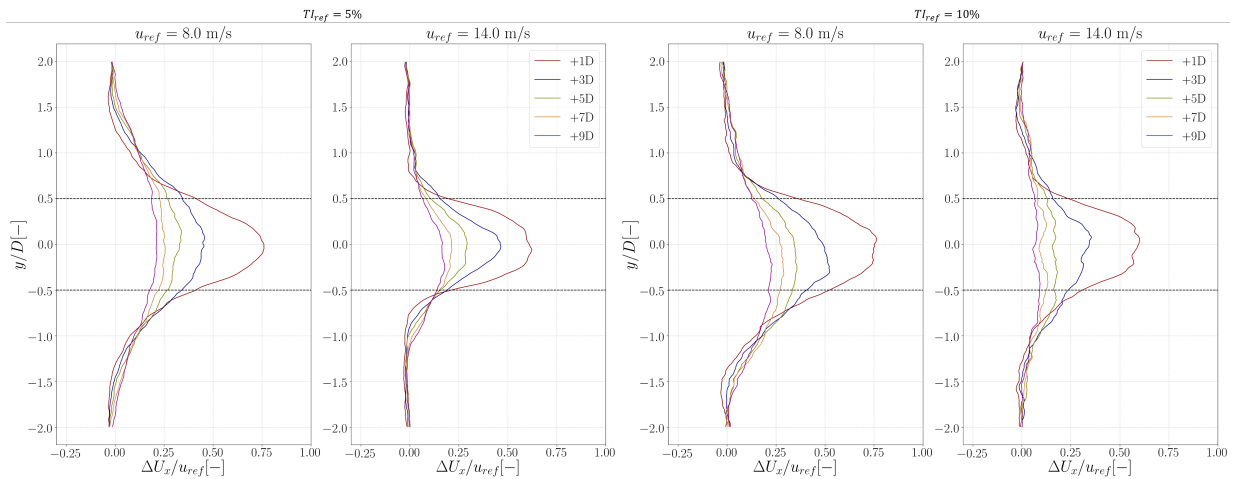


Figure 5.10: The profile of the time-averaged stream-wise velocity deficit along the y -direction at different stream-wise positions behind T3. Note, the points are sampled at $z = 105.52\text{m}$ or at the hub height.

The stream-wise turbulence intensity along the z -direction is also displayed in Fig. 5.11. The data are noisier since the number of sample points were low. This is due to the physical time of the simulation being limited, as mentioned in the previous section. A common trend is observed for all the cases wherein the TI peaks at a distance of 3D from T3, which has also been observed in wind tunnel simulations [90]. The upper region of the wake is more turbulent due to the shear between it and the free-stream flow. This is also responsible for the sharper peak in TI seen for the 8m/s cases. The TI maxima is higher for 8m/s and 5% TI case, reaching a value of 24%. This plot also shows how the vertical spread of the wake is affected by the inflow TI. For the 10% TI cases, the turbulence intensity is higher than ambient even at a height of 3D from the ground.

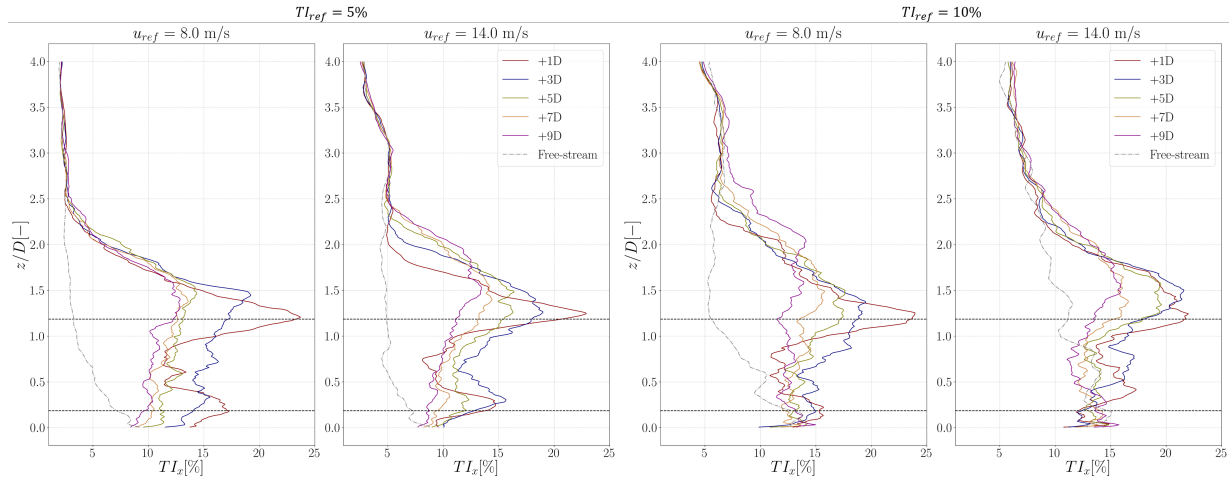


Figure 5.11: The profile of TI_x along the z -direction at different stream-wise positions behind T3. Note, the points are sampled at $y = 0$ or along the center-line of the domain.

5.2.3. Power production

The time-averaged power output of all three turbines is shown in Fig. 5.12. The error bars indicate the standard deviation. All the values are normalized by the rated power of the SWT-6.0-154 turbine. For the 12 and 14 m/s cases, T1 operated at its full-load condition. Thus, the average power output is close to 6MW. In all the cases, T1 has the highest power output with T2 and T3 producing less due to the reduced wind speed in the wake. For the 8m/s cases, an interesting phenomena is observed where P_{elec}^{T3} approximately 25% greater than P_{elec}^{T2} . This aligns with data from wind farm measurements and studies using the RANS method [91, 92]. For the 14m/s and 10% TI case, T2 also operates at rated condition.

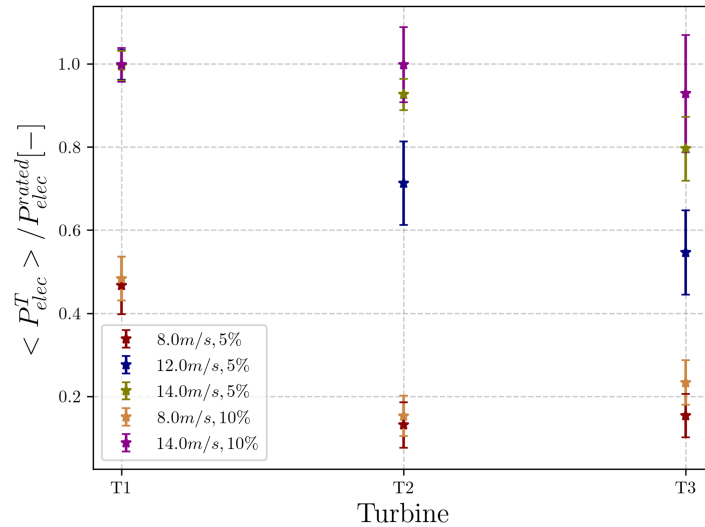


Figure 5.12: The time-averaged power output for each turbine under the five inflow conditions, normalized by its rated value. The error bars show the standard deviation.

5.2.4. Wake recovery

Next, the impact of the inflow conditions on the recovery of wind speed in the wake is investigated. In order to quantify the stream-wise evolution of the wake, the time-averaged velocity field is further averaged over a line of length equal to the rotor diameter:

$$\langle \langle U_x \rangle \rangle^D = \frac{1}{D} \int_{-D/2}^{+D/2} \langle U_x \rangle dz. \quad (5.2)$$

Then, for a particular inflow case, the values are normalized using the following relation:

$$\bar{U}_x^T(x) = \frac{\langle\langle U_x \rangle\rangle^D(x)}{\langle\langle U_x \rangle\rangle^D(x = +4D)}. \quad (5.3)$$

The resulting plot is shown in Fig. 5.13. As a result of the normalization, all the lines start from a value of 1.0 in the region far upstream of T1. This method also allows for a fair comparison of the recovery in case of differing inflow wind speeds. The dashed black lines show the stream-wise locations of the turbines while the red line on the rotor plane shows where the integral in Eq. (5.2) is calculated. Note, the data are sampled only at discrete points which are indicated on the figure.

In all five cases, there is a sharp drop in the velocity as it passes through the rotor, reaching a minima approximately 1D behind T3. From this point on the wake begins to recover reaching more than or equal to 80% of its free-stream value at a distance of 9D from T3. The impact of the inflow wind speed is clear to see as the 8m/s cases experience a sharper drop when passing through the rotors. This is due to the turbine operating in the below-rated region where the thrust force is higher. These two cases also stand out because the inflow on T3 is higher than of T2. This causes P_{elec}^{T3} to be greater than P_{elec}^{T2} , as seen in Fig. 5.12. The wind speed incident on T2 is around 4 m/s which is just above cut-in. Thus, the deficit behind it is severe enough to trigger fast recovery of the wake leading to the observed trend.

It can also be inferred that for the 8m/s cases, it is hard to differentiate between the inflow TIs. The wake appears to recover at the same rate. On the other hand, for the 14m/s cases, the rotor-averaged velocity recovers 30% faster in the 10% TI case.

For 14m/s U_{ref} and 10% TI_x , $\langle\langle U_x \rangle\rangle^D$ reaches 90% of its free-stream value at a distance of 7D from T3. The faster recovery is partly due to the higher ambient TI and partly due to the lower deficit. The latter is because of the fact that T2 is operating at above rated conditions, as seen in Fig. 5.12.

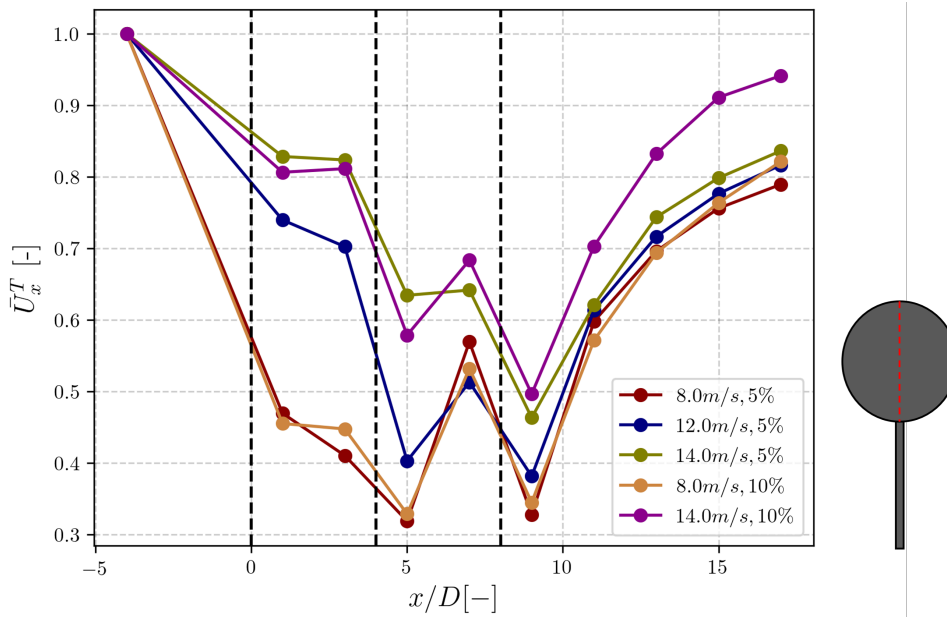


Figure 5.13: The evolution of rotor-averaged stream-wise velocity along the stream-wise direction.

In Fig. 5.14, the stream-wise evolution of the rotor-averaged TI_x is presented after being computed using the following relations:

$$\langle\langle TI_x \rangle\rangle^D = \frac{1}{D} \int_{-D/2}^{+D/2} \langle TI_x \rangle dz. \quad (5.4)$$

$$\bar{TI}_x^T(x) = \frac{\langle\langle TI_x \rangle\rangle^D(x)}{\langle\langle TI_x \rangle\rangle^D(x = +4D)}. \quad (5.5)$$

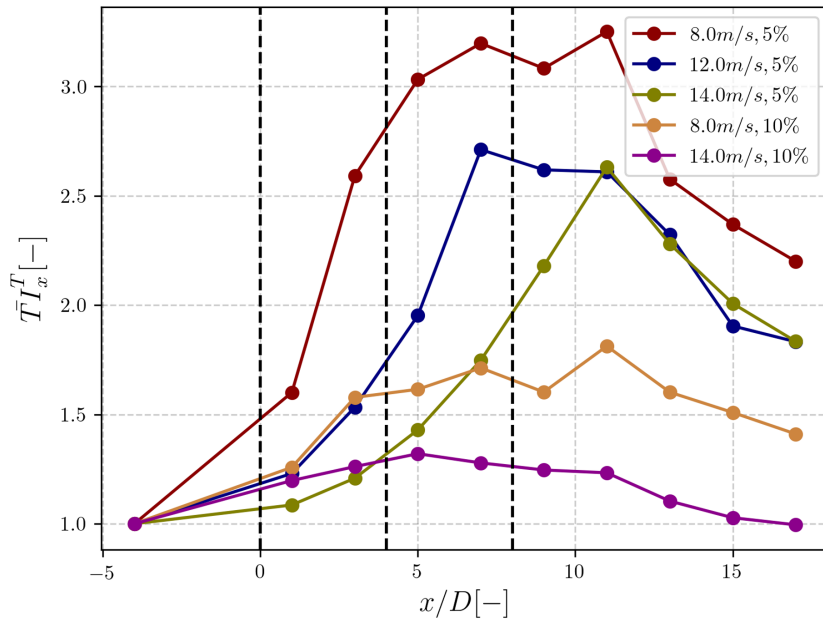


Figure 5.14: The stream-wise evolution of TI_x in the wake.

From this figure, it is seen that when the inflow TI is low, the relative turbulent fluctuations are higher within the rotor plane. Indeed for the 8.0m/s and 5% TI case, rotor-averaged TI_x becomes 3.3 times its ambient value at a distance of 3D downstream of T3. But for the 10% TI cases, the relative increase in $\langle\langle TI_x \rangle\rangle^D$ is 40% less. Thus, it appears that the presence of more turbulence in the ambient flow damps the fluctuations within the wake.

In absolute terms, the turbulence level within the wake is similar in both the 8.0m/s cases. This would explain the similar rate of recovery seen in Fig. 5.13. But, the rotor-averaged TI_x in 14.0m/s cases, is also found to be similar, while the rate of wake recovery is not the same. When, increasing the limits of the integral of Eq. (5.4) to $(-D/2, 2D)$, $\langle\langle TI_x \rangle\rangle^D$ in the 14.0m/s, 10% TI case is 50% higher. Thus, accounting for the increase in TI_x in the free-stream flow close to the wake boundaries explains the difference in the wake recovery for the 14.0m/s cases.

In summary, the results indicate that for a multi-turbine configuration, at low wind speeds, wake recovery is driven by the wake-added turbulence while at higher wind speeds, the ambient turbulence is more significant. But it is important to note that this statement cannot be confidently concluded. Firstly, the data are discretely sampled at a distance of 2D from each other. This may not be a sufficient resolution and certain features of the stream-wise evolution of the flow could be missing. Secondly, for 10% TI cases, the rate of recovery is higher in the 14.0m/s case. But, contradictorily, the rotor-averaged TI_x is lower for this case as compared to the 8.0m/s and 5% TI case. Thus, further investigation is necessary which could not be completed in the time-line of this thesis.

Nonetheless, there is a dependence of wake recovery on the wind speed which means that former is not entirely determined by the ambient TI, particularly when a number of turbines operate in a line. Here, the wake-added turbulence is high and it could play a more important role in triggering wake recovery at low wind speeds.

5.2.5. Wake meandering

This section is dedicated to a discussion of wake meandering and its qualitative dependence on the turbulence in the external flow. First, the method of identifying the wake center is presented. Next, the time-averaged statistics of the wake center are used to quantify the meandering under different inflow conditions. Finally, the correlation between the temporal location of the wake center and the power signal is assessed.

The definition of the wake center and its subsequent computation has been an open question and a number of methods have been developed for this purpose [93]. For this study, the wake center is computed

based on the minimum available power method [94]. Herein, a disk convolution is applied on vertical slices of the instantaneous velocity field and the kinetic power on this disk is calculated. The grid point with the lowest available power is selected as the wake center:

$$(y_c, z_c) = \operatorname{argmin}(p * f_s), \quad (5.6)$$

where,

$$f_s(y, z) = \begin{cases} 1 & \text{if } y^2 + z^2 < \left(\frac{D}{2}\right)^2 \\ 0 & \text{otherwise.} \end{cases} \quad (5.7)$$

such that, $p = \frac{1}{2} |U|^2 U_x$, D is the rotor diameter, y_c is the lateral position of the wake center and z_c is its vertical coordinate.

The motivation behind using this method is that it is based on physical arguments and is easy to implement. Further, due to limitations on time, only y_c is computed in this study. Thus, the drawback of the minimum power method where z_c is spuriously skewed towards the ground, is avoided. Additionally, y_c is chosen for analysis since the wake meanders more in the lateral direction than in the vertical [5].

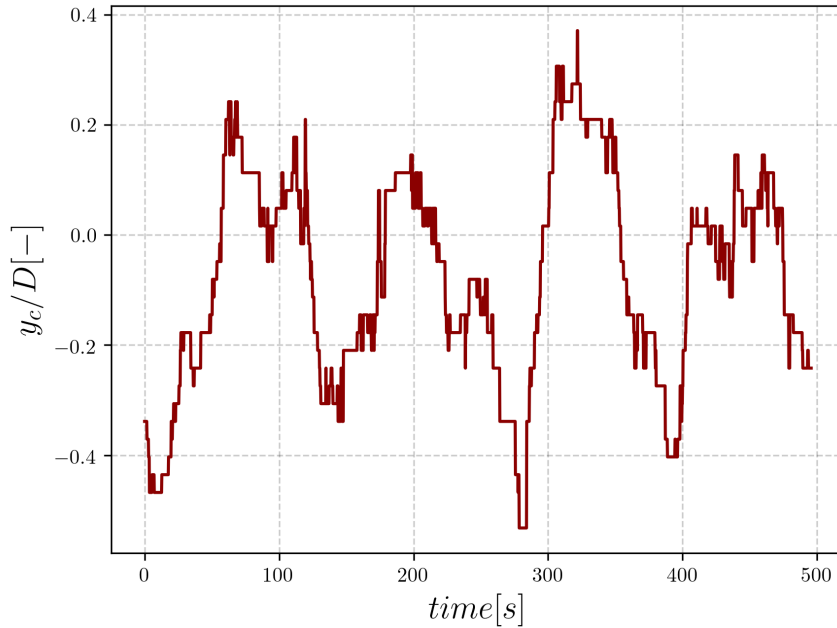


Figure 5.15: The time series of y_c as computed by the minimum available power method for the 8m/s and 10% TI case at a location of 3D downstream of T2.

Next, the wake centers are computed using this method at a time step of 0.2s. This is larger than the time-step of the simulation to reduce the storage requirements of the raw data. Since the wake meanders at a frequency of 0.005 to 0.1Hz [93], any aliasing effects will still be avoided. The time series of y_c is shown in Fig. 5.15. Although there are a few outliers, the average displacement of the wake center between adjacent time steps is 1.1m. This corresponds to a lateral velocity of 5.5m/s which is within the expected limits [95]. The presence of outliers is an inherent part of the wake tracking method, as established in [93]. With a large sample size, the effect of the outliers can be minimized. In this study, around 3000 samples are considered. An even larger data-set would be preferable to also include the lowest frequencies of meandering but this would require the simulation to run for more than two hours of physical time. As mentioned earlier, the time-step inherited from BHawC severely limits this.

The time averaged statistics, that is, the mean and standard deviation of the wake center are also computed and are shown in Fig. 5.16 and Fig. 5.17 for the all the cases.

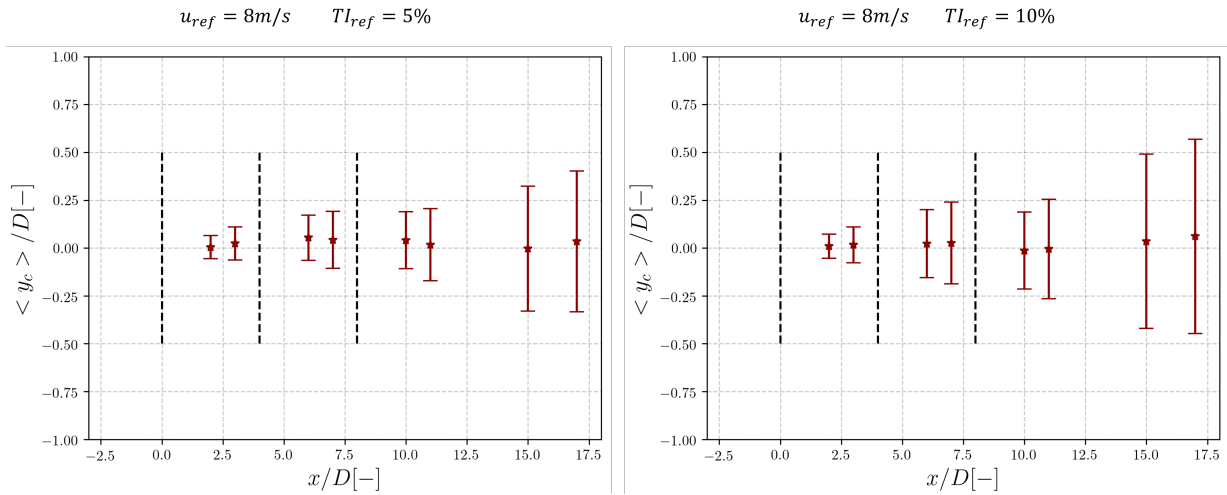


Figure 5.16: The mean location of the wake center at different stream-wise locations with the error bars denoting the standard deviation for the $u_{ref} = 8m/s$ cases.

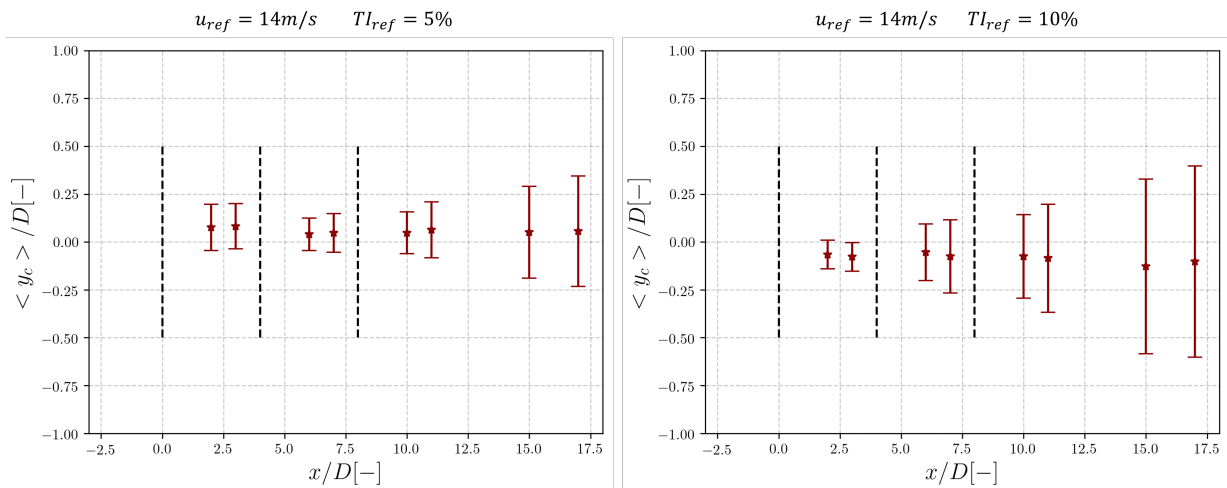


Figure 5.17: The mean location of the wake center at different stream-wise locations with the error bars denoting the standard deviation for the $u_{ref} = 14m/s$ cases.

The mean location of the wake is close to the rotor center given the lack of yaw offset on the turbine. The extent of meandering is quantified by the standard deviation of the wake center. From this, it can be observed that there is more meandering in the 10% TI cases. The standard deviation of y_c increases on average by 60% when the TI in the y-direction changes from 4 to 8%. The amount of meandering also depends on the stream-wise distance from the turbine. At 3D downstream of T3, the range of meandering is 1D while at a distance of 7D it is 2D.

The Fourier Transform of the time signal of y_c is also presented in Fig. 5.18 for the 14m/s cases. The 1st peak in the spectra occurs at a frequency of 0.015Hz for the 5% TI case while for the 10% TI case, it is at 0.009Hz. In the latter case, the second peak is seen at 0.015Hz. Beyond this frequency, both the cases show a number of smaller peaks up to 0.1Hz, as is observed in the literature [93, 5]. The Strouhal number is in the range of 0.1 to 0.4 which is verified by previous studies [95]. Since the spectra from different stream-wise locations coincide, the meandering frequency is said to remain invariant as the wake propagates downstream. There is an upward shift in the amplitude for the +15D and +17D spectra which is due to the larger amount of meandering occurring at these locations. The 8m/s cases show a similar trend and hence the corresponding spectra are not shown here.

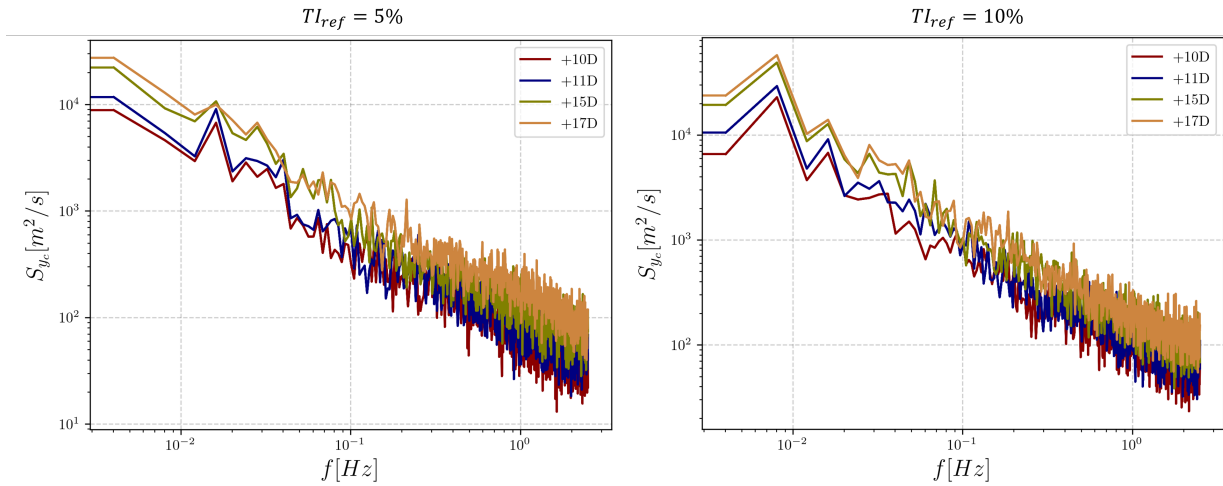


Figure 5.18: The Fourier Transform of the y_c at different stream-wise locations.

Next, the correlation between the wake center of the inflow on the waked turbines and the electrical power output of the turbines is assessed in the time domain. The purpose of this is twofold. It is important to determine whether wake meandering affects the power output of the turbine. Secondly, a number of wake control techniques in use today rely on predicting the location of the wake incident on a turbine using its power output [96, 97]. Here, the Spearman Rank coefficient r_s is used to quantify the correlation [98]. It is a measure of the strength of a monotonic relation between the parameters of interest. If the two variables are perfectly positively correlated, the Spearman rank correlation should be +1. In other words, this measure should aid in determining whether y_c can be predicted from P_{elec} or vice versa.

After averaging the data for T2 and T3 in all the five cases, it is found that r_s is equal to +0.2 with a p-value of 10^{-6} . Thus, the power signal alone does not provide a strong indication of the location of wake center. r_s has a positive sign because when the wake center moves away from the rotor center, the turbine will experience higher wind speeds. On the other hand, when y_c is small, the turbine is likely to be in the wake and correspondingly the power output will be lowered. A correlation of 0.2 suggests that power output is not completely determined by the wake location. Since the former is also dependent on the behaviour of the controller, changes in y_c may not be proportionally reflected in P_{elec} as the controller regulates power production.

To summarize, the effect of increasing the ambient turbulence is observed through an increase in the root-mean-square of the lateral position of the wake center. The stronger and more frequent eddies that come with higher TI in the inflow are responsible for moving the wake to a larger extent. These drive the lateral and vertical motion of the wake. Additionally, the spectra of the wake center show that a higher turbulence intensity introduces more fluctuations at lower frequencies. This effect may be a reflection of the change in the turbulence spectra itself. However, the turbulence added by the wake does not affect meandering. Indeed, the 8m/s and 14m/s cases shown a similar level of meandering even though the wake added turbulence is quite different, as seen in Fig. 5.14. These results further verify the hypothesis that wake meandering is driven by the external flow [95].

This concludes the discussion on impact of the inflow conditions on the properties of the wake. The next chapter focuses on a different study wherein the impact of partial wake incidence on the wind turbine structural response is assessed.

From full wake to half wake interaction: structural impact

The aim of this chapter is to compare the structural impact of two different partial-wake interaction scenarios. Continuing with the three turbine configuration defined in the previous chapter, by introducing a lateral offset on the rotors, the last turbine can be subjected to a wake that is asymmetric over the azimuth. Given the sensitivity of the turbine loads the inflow, it is expected that the response of the turbine will vary between the two scenarios. Thus, this chapter presents a comparison of the forces on the blade, tip deflection and fatigue damage. Two different wind speeds are also investigated. These correspond to the above and below-rated regions of operation. The results of this study are expected to highlight the importance of considering the wake position according to the downstream rotor, especially with regards to low-fidelity wake modelling. Herein, the wake is often assumed to be axi-symmetric and adequate treatment is rarely given to different partial-wake scenarios [99]. The flow field in the wake is often parameterized in terms rotor-averaged velocity and turbulence intensity. This may lead to under-prediction of loads, especially fatigue.

This chapter is ordered as follows. First, the simulation setup is presented along with an overview of the two layouts to be studied. Then, the resultant flow field is visualized in a number of ways to analyse the waked inflow and the operating conditions of the turbine. Next, the flap-wise and edge-wise loads on the blade are shown in terms of the time series, spectra and azimuthal-averaged plots. Finally, the fatigue damage is analysed via the Damage Equivalent Load.

6.1. Simulation setup

The methodology remains the same as in Chapter 5, only the layout of the turbines in the domain is changed along with the inflow conditions. These are shown herewith.

6.1.1. Domain and turbine configuration

Fig. 6.1 and Fig. 6.2 depict the turbine configurations under study. Layout “L1” corresponds to asymmetric wake incidence on T3 since the wake from T1 and T2 impact the same side. Thus, a blade of T3 will on average experience waked inflow for one half of its rotation and free-stream inflow for the other half. But in case of Layout “L2”, T3 will sample wake from T1 during one half of its rotation and from T2 during the other. The turbine separation and domain dimensions are the same as in Chapter 5. Note than only the structural response of T3 will be studied in this chapter.

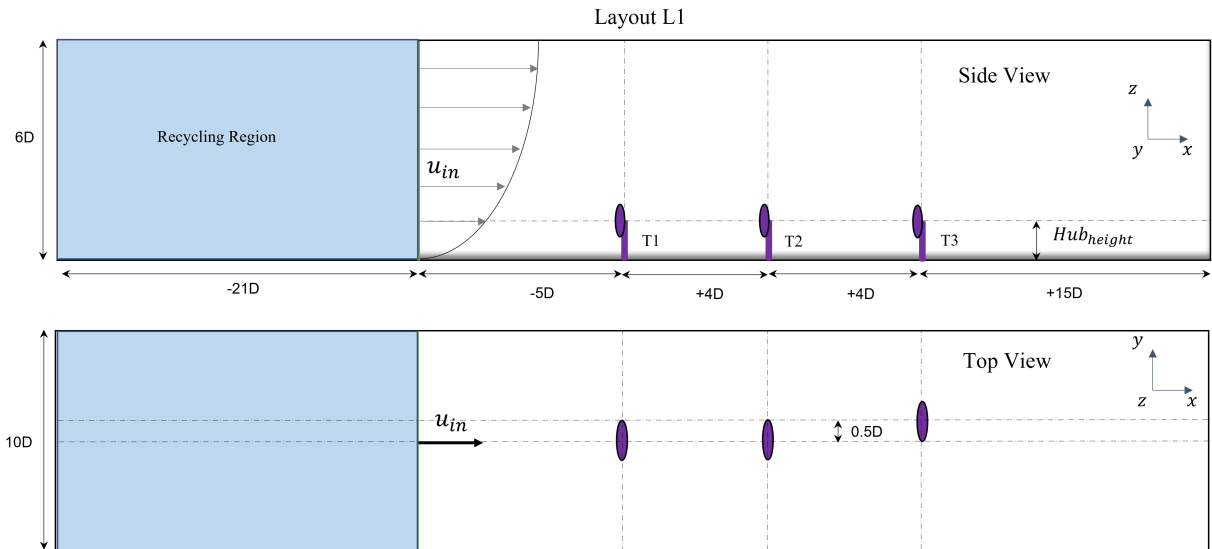


Figure 6.1: A representation of the Layout “L1” wherein half-wakes from T1 and T2 impact the same side of T3.

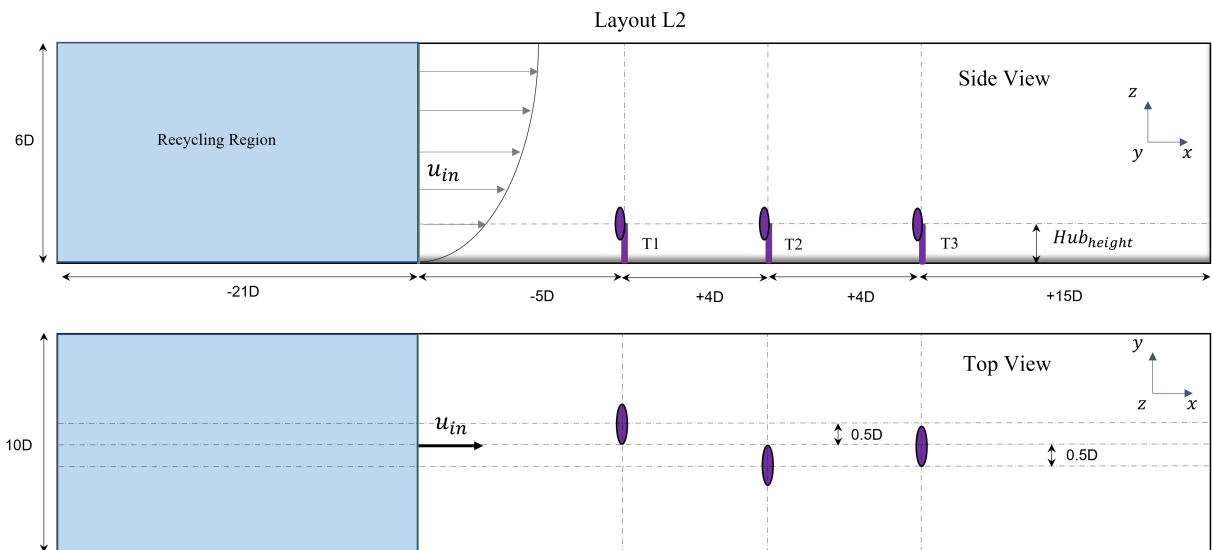


Figure 6.2: A representation of the Layout “L2” wherein half-wakes from T1 and T2 impact opposite sides of T3.

6.1.2. Inflow conditions

The inflow is slightly different Chapter 5 and is shown in Table 6.1. The 8.0 m/s wind speed corresponds to below-rated operation of the turbine while 14 m/s leads to above-rated operation. The TI is kept constant at a value of about 8.5% which is similar to an offshore environment [84].

Table 6.1: The inflow conditions used for the study

Target $\langle U_x \rangle$ at hub or u_{ref} (m/s)	Actual $\langle U_x \rangle$ at Hub (m/s)	Rotor-Averaged TI_x (%)	Shear Coefficient
8.0	8.3	8.5	0.11
14.0	14.4	8.6	0.13

Thus, the four cases that form this study will be L1 8m/s, L1 14m/s, L2 8m/s and L2 14m/s, where L1 8m/s, for example, refers to the Layout “L1” with an inflow wind speed of 8m/s at hub height.

6.2. Results

6.2.1. Flow topology



Figure 6.3: A Q-criterion iso-surface visualizing the turbulence generated in the wake as well as the helical tip vortices in L2 8m/s case. A value of $Q_{crit} = 0.02s^{-2}$ is used as the threshold.

Since the aim of this chapter is to check the effect of the sensitivity of the structural response of the turbine to the wake position on the rotor plane, the inflow on the waked turbines must be determined. This is achieved via Fig. 6.4, Fig. 6.5 and Fig. 6.6 where the flow field is visualized on horizontal plane at the hub-height of the turbines. Note that while analysing the flow topology, only the stream-wise component of the velocity is considered for the sake of simplicity.

It is observed that in case of L1, T3 experiences partial wake conditions. On average, 50% of the rotor plane of T3 is under the wake of T2 and T1 while the rest is under free-stream. But as a result of meandering, at some instances, T3 also experiences fully free-stream inflow. The iso-contours of the TI show that due to the wake turbulence, TI_x over the rotor-plane of T3 is 10.5% when $u_{ref} = 8m/s$.

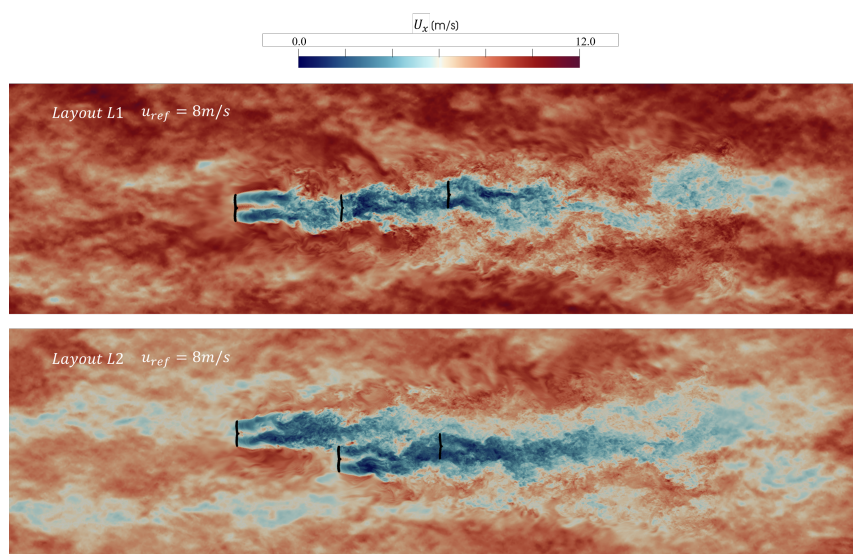


Figure 6.4: The instantaneous velocity field visualized on a horizontal plane at hub height.

In the L2 configuration, T3 is completely under wake of either T1, T2 or both. On average, 80% of the rotor plane of T3 is in the wake of T2 while the rest is in the wake of T1. This more than the expected 50% due to the wakes of T1 and T2 interacting with each other where one slightly deflects the other along the lateral direction. Here, a slight speed-up in the middle is observed. From Fig. 6.6, it is seen that the average TI_x over T3 is also 10.5% for $u_{ref} = 8m/s$. A similar trend is observed in the 14m/s cases although with higher wind speeds in the wake and $TI_x = 8.9\%$.

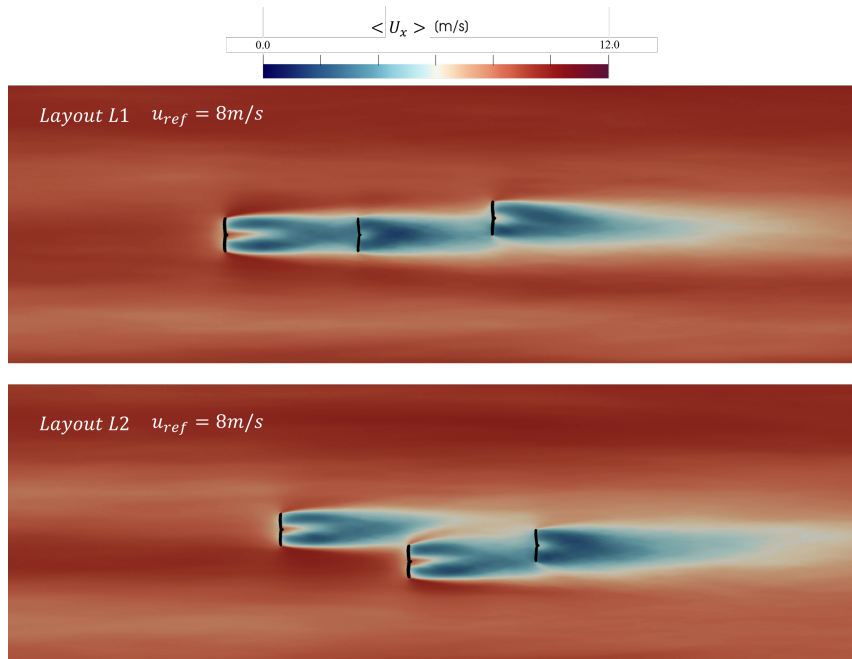


Figure 6.5: The time-averaged velocity field visualized on a horizontal plane at hub height.

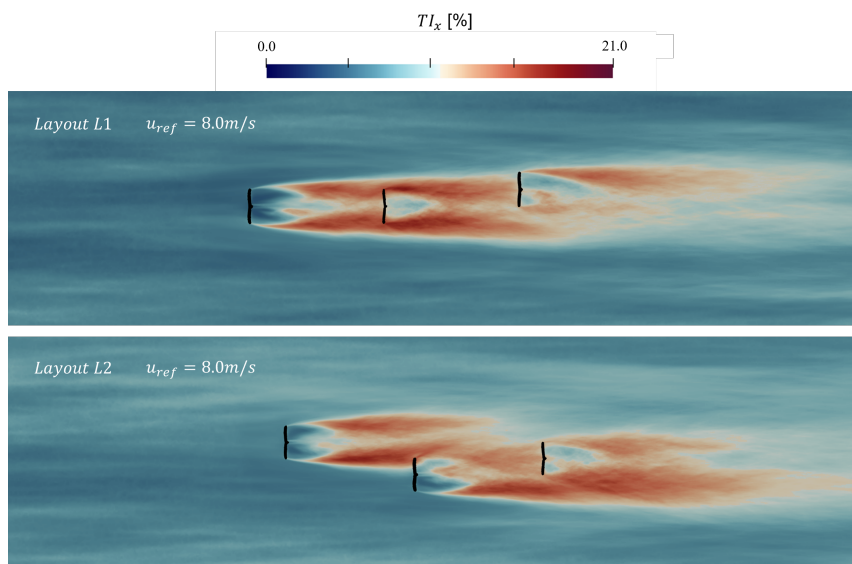


Figure 6.6: The turbulent intensity in the stream-wise direction visualized on a horizontal plane at hub height.

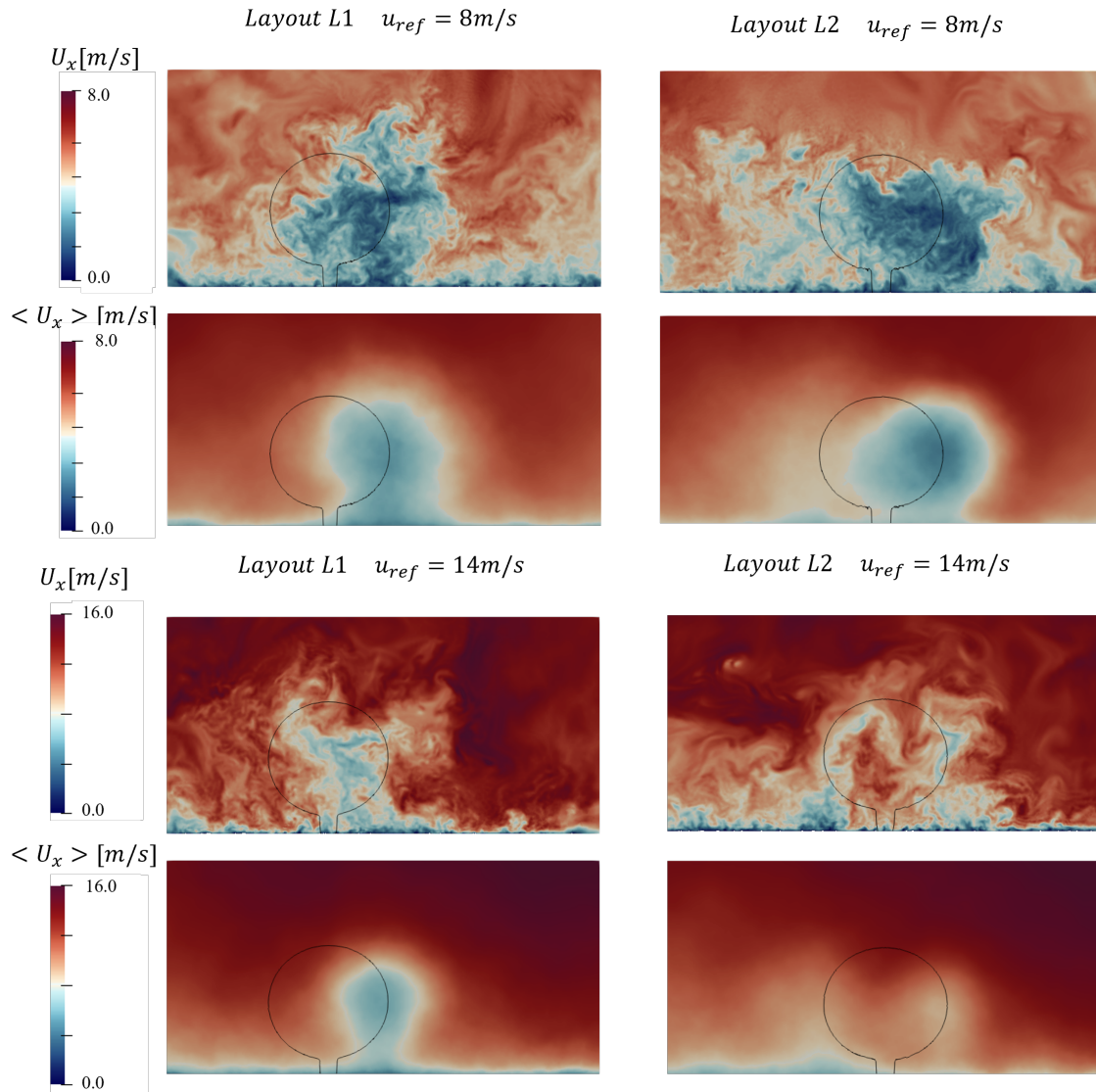


Figure 6.7: The instantaneous and time-averaged inflow on T3 (here highlighted by the black lines) in all of the four cases

Fig. 6.7 shows the iso-contours of U and U_x on a plane normal to the stream-wise direction at a distance of $1D$ upstream of T3. These indicate that in case of L1 and $u_{ref} = 8m/s$, the blade will experience free-stream flow for one half of its rotation and the combined wake of T1 and T2 for the other half. But when $u_{ref} = 14m/s$, the only 25% of the rotor plane of T3 is in the wake. With respect to L2, the wind speed also plays an important role. At $u_{ref} = 8m/s$, the interaction between the wakes of T1 and T2 causes 80% of the rotor plane of T3 to be in the wake of T1. But when $u_{ref} = 14m/s$, no such interaction takes place. Thus, the wakes of T1 and T2 are equally distributed over T3. Overall, based on the profiles of $\langle U_x \rangle$, the flow incident on T3 is more uniform in the L2 configuration.

The time-averaged velocity profiles along the lateral direction at hub-height incident on T3 in all four cases can be visualized in Fig. 6.8 and Fig. 6.9. It is seen that in L1, the inflow on T3 has a significant shear in the lateral direction. $\langle U_x \rangle$ varies between 4 to 7m/s in the 8m/s case while the variation is even larger in the 14m/s case with the wind speed ranging from 10 to 14 m/s.

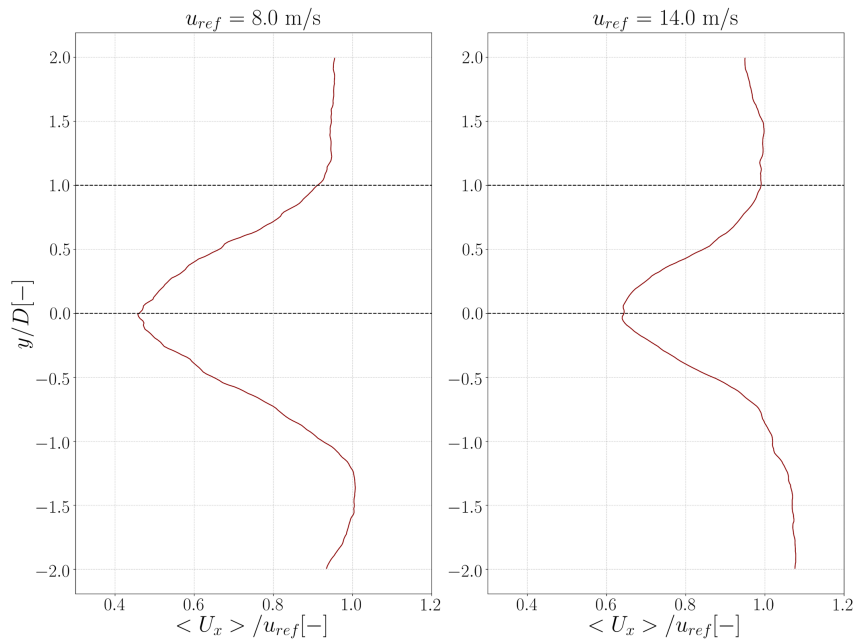


Figure 6.8: The profile of $\langle U_x \rangle$ along the lateral direction at a distance of 1D upstream of T3 in the L1 configuration. The black lines indicate the rotor location of T3.

For the L2 configuration, there is also a horizontal shear in the inflow but only for the 8m/s case. Here, the wind speed gradient is smaller than it was in L1, with $\langle U_x \rangle$ ranging between 3m/s to 5.5m/s. But when the reference wind speed is 14m/s, the inflow is more uniform with a slight speed up in the core. This is because at 14m/s the wakes produced by T1 and T2 are not as strong. Here, the turbines operate at above rated conditions, as seen in Fig. 6.10. Thus, the wake of T1 is no longer deflected by that of T2 leading to the latter being incident on the left half of T3. Additionally, the wakes of T1 and T2 never merge, which creates the small speed-up in the core.

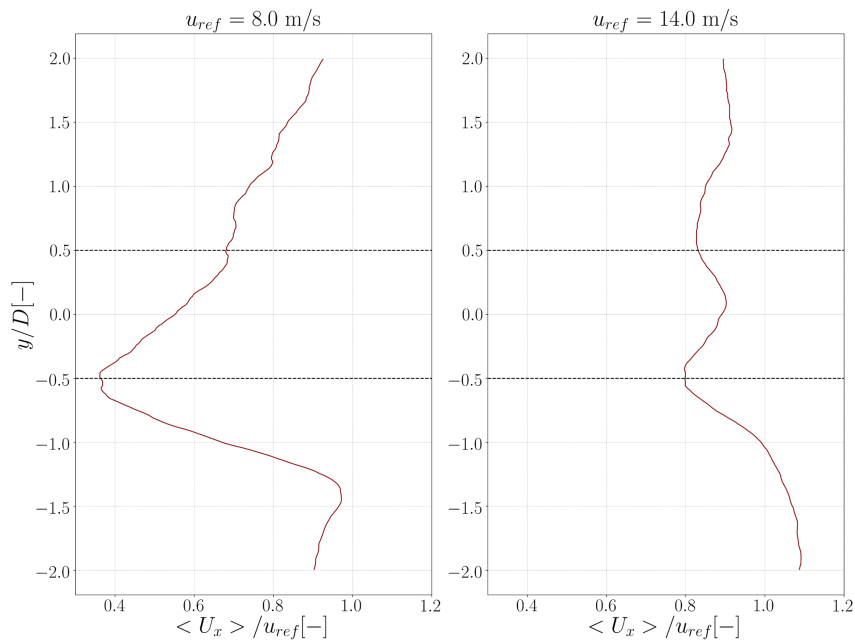


Figure 6.9: The profile of $\langle U_x \rangle$ along the lateral direction at a distance of 1D upstream of T3 in the L2 configuration. The black lines indicate the rotor location of T3.

It is also important to establish the operating condition of each turbine in all the four cases. This is achieved by visualizing the time-averaged power output, rotation speed and blade pitch, as shown in Fig. 6.10. It can be inferred that for both of the 8m/s cases, all the turbines are at below-rated condition since the pitch angles have the same sign and the power output is lower than P_{rated}^{elec} . Correspondingly, for the 14m/s cases, since the pitch angle changes sign and the power output is close to rated, T3 operates at full-load condition.

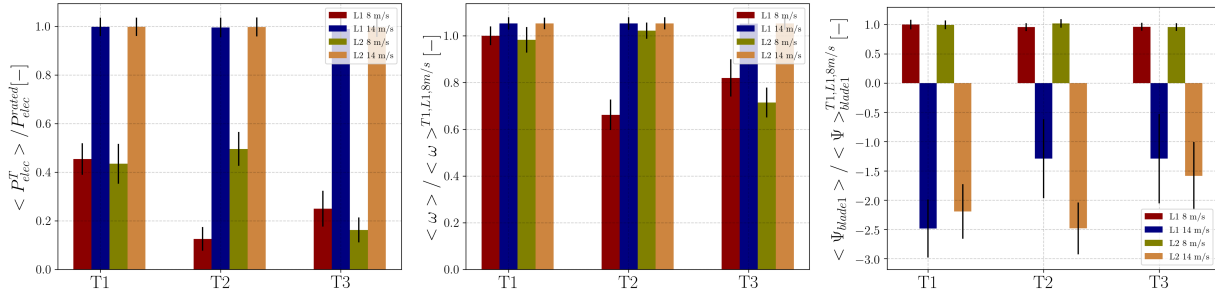


Figure 6.10: A comparison of the electrical power output (P_{elec}), the rotation speed (ω) and the blade pitch angle (Ψ) for all three turbines for the four cases. The error bars show the respective standard deviation.

6.2.2. Structural response of the rotor

Given the difference between the two configurations in terms of the spatial distribution of the wake, it is expected that the structural response of the blade will also differ. Thus, the forces and deflection of the blade is studied in the flap and edge-wise directions. These are defined with respect to the blade basis. The flap-wise direction is normal to the chord of the blade cross-section while the edge-wise direction is parallel to it.

Firstly, Fig. 6.11 and Fig. 6.12 show the time series and the Fourier Transform of the flap and edge-wise moments at the root of blades. For the purpose of clarity, only 100s of the time signal are shown here, during which, the turbine completes 13 full rotations. This is verified by the presence of 13 peaks and troughs in the time series of the edge-wise moment. Since the gravitational force makes the largest contribution to this channel, the moment changes direction twice in one rotation. There is not much difference between the two configurations which is also true for the 14m/s cases. With respect to the time series of the flap-wise moment, the difference between L1 and L2 from 100 to 120s can be attributed to the temporal location of the wake. As the wake meanders away from the rotor, the flap-wise loads can be expected to increase as they are more sensitive to the inflow itself.

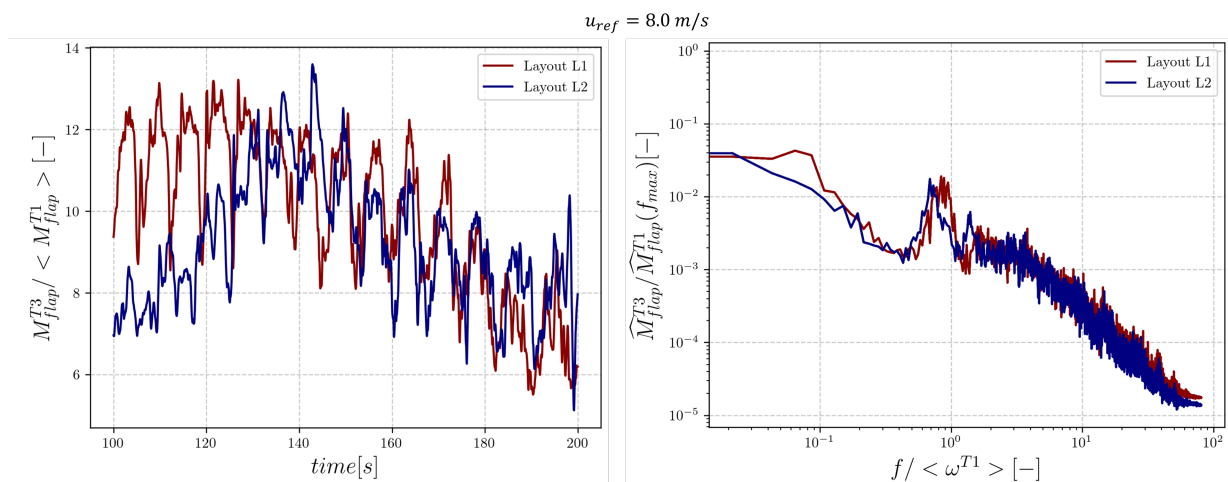


Figure 6.11: The time series for the flap-wise bending moment on blade 1 of T3 and its Fast Fourier Transform for the L1 and L2 8m/s cases

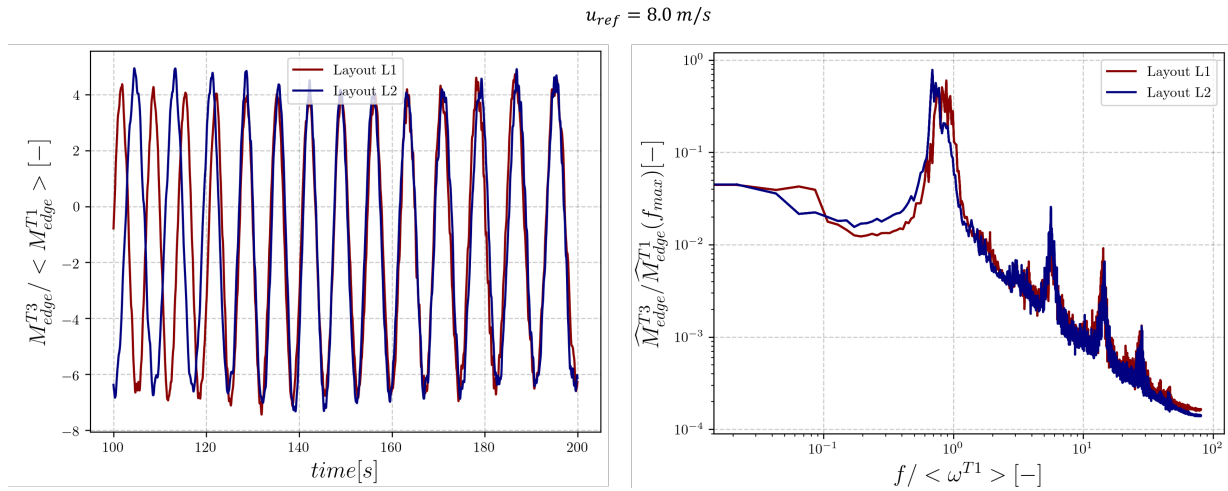


Figure 6.12: The time series for the edge-wise bending moment on blade 1 of T3 and its Fast Fourier Transform for the L1 and L2 8m/s cases

The spectra of the loads can also be seen in the same figure. For the flap-wise moment, the 1st peak is seen at 1P frequency. This is due to rotational sampling of the partial-wake in addition to the wind shear and tower shadow. The next peak is seen at 2P. The slight mismatch in the peaks is due to the difference in the rotational speed of T3 in L1 and L2. In the latter case, $\langle \omega \rangle$ is slightly higher. The edge-wise spectra in the two cases show more overlap with peaks of the same amplitude at 1P, 2P, 6P, 12P and 16P. The even-numbered harmonics can be attributed to the change in the direction of the gravitational load.

Next, the azimuthal and radial distribution of the flap-wise and edge-wise forces on the blades of T3 are shown in Fig. 6.13 and Fig. 6.14. In order to obtain the azimuthal data, 360 bins from 0 to 359° with a size of 1° are created. Then, the time series data of the blade forces are put into the bin corresponding to the location of the blade in the azimuth at the same time step. Next, the data in each bin are averaged to obtain the time-averaged value at each azimuth. Finally, the values are displayed in the dimensionless form as:

$$\langle F_{flap} \rangle^\theta = \frac{\langle F_{flap}(r, \theta) \rangle}{\langle \langle F_{flap}(r, \theta) \rangle \rangle^{T1}}, \quad (6.1)$$

where $\langle \langle F_{flap}(r, \theta) \rangle \rangle^{T1}$ is the force averaged over the entire rotor plane of T1 in the L1 8m/s case.

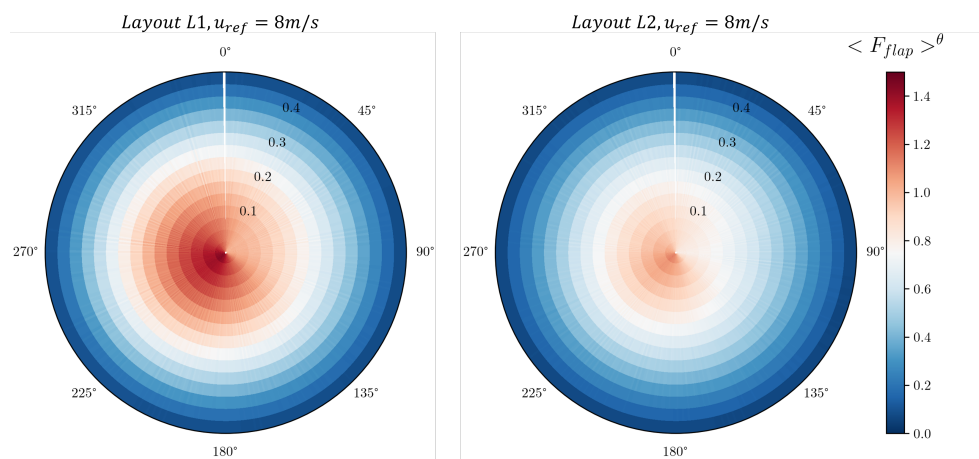


Figure 6.13: The azimuthal and radial distribution of the time-averaged flap-wise force on T3. On the left Layout L1 is shown while L2 is on the right.

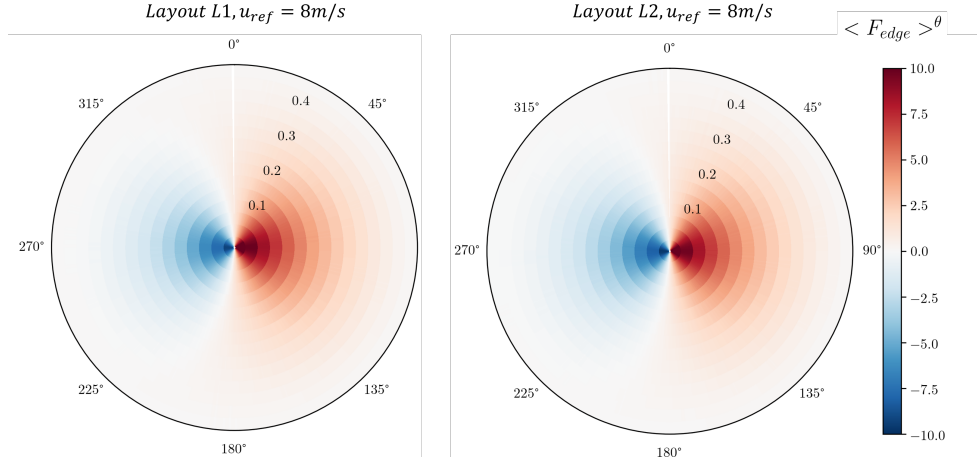


Figure 6.14: The azimuthal and radial distribution of the time-averaged edge-wise force on T3. On the left Layout L1 is shown while L2 is on the right.

With respect to the flap-wise forces, the magnitude decreases when moving outwards in the radial direction. This is a feature of blade design wherein the chord decreases in the span-wise direction to limit the moment induced at the blade-root. There also exists on average higher forces in the top half of the rotor than the bottom as a consequence of the vertical wind shear. In addition, the L1 configuration shows an asymmetry. The left half experiences higher forces than the right. When averaging over the two halves, the left one sees a 20% increase. This region of the rotor is also under wind speeds that are 20% higher. On the other hand, the profile of $\langle U_x \rangle$ on T3 in L2 is more uniform. Thus, the difference in the forces between the two halves is 4%. A similar trend is observed for the 14m/s cases and hence resulting figures are not shown here.

Next, in Fig. 6.14 two distinct regions can be identified. When the blade is between 45 to 135°, the edge-wise forces show a positive peak. This is due to the blade being close to its horizontal position where the component of the gravitational force in the edge-wise direction is the highest. Thus, a negative peak is also seen between 225 to 315° but since the blade is moving upwards, the sign changes. The edge-wise forces are also higher closer to the root since the blade section solidity and hence its weight is inversely proportional to the radial distance from the center. Here, not much difference is seen between L1 and L2 which suggests that the aerodynamic thrust is not as significant in this direction as compared to gravity.

It is also important to evaluate the effect of the computed forces on the blade deflection. This is shown in Fig. 6.15 and Fig. 6.16 wherein Eq. (6.1) is applied to the tip deflection. Thus, $r = \frac{D}{2}$ and the reference is the maximum tip deflection of T1 in the L1 8m/s case:

$$\langle \epsilon_{flap} \rangle^\theta = \frac{\langle \epsilon_{flap}(r = D/2, \theta) \rangle}{\max(\langle \epsilon_{flap}(r = D/2, \theta) \rangle^{T1})}, \quad (6.2)$$

In the flap-wise direction, on average, the tip deflection is 13% higher for the L1 configuration. The difference between L1 and L2 is more in the left half of the rotor plane. Again, the inflow is responsible for the observed trends. The root mean square of $\langle \epsilon_{flap} \rangle$ in the azimuthal direction can also be computed to further quantify the fluctuations:

$$\sigma_{\langle \epsilon_{flap} \rangle} = \frac{\text{rms}(\langle \epsilon_{flap} \rangle^{T3}) - \text{rms}(\langle \epsilon_{flap} \rangle^{T1})}{\text{rms}(\langle \epsilon_{flap} \rangle^{T1})} * 100. \quad (6.3)$$

For L1, it is 120% while for L2 it is only 15%, when $u_{ref} = 8m/s$. Thus, for the L1 configuration, the azimuthal fluctuations experienced by T3 are almost twice those of T1. When $u_{ref} = 14m/s$, a larger tip deflection is obtained since T3 operates at rated condition. Here, the wind shear is also stronger which causes the profile of $\langle \epsilon_{flap} \rangle$ to be elongated along the 0° direction. As seen from Fig. 6.8 and Fig. 6.9, compared to L2, the wind speed on T3 in L1 is higher in the left half of the rotor plane and lower in right

half. Correspondingly, $\langle \epsilon_{flap} \rangle_{L1}^{T3}$ is higher at 270° and lower at 90°. This further underlines the sensitivity of the blade structural response to the inflow.

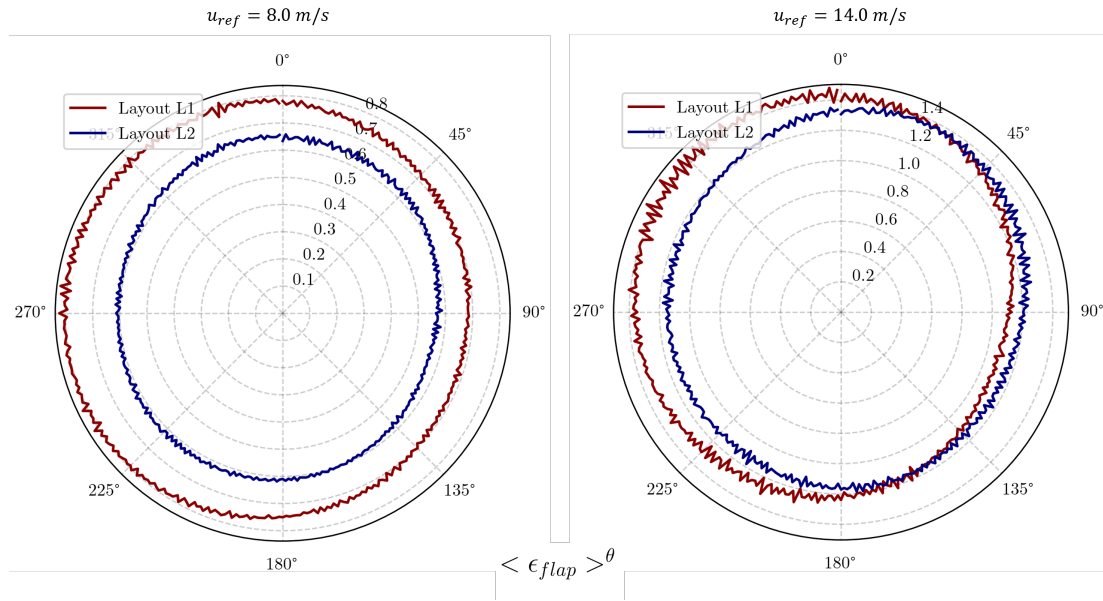


Figure 6.15: The azimuthal distribution of the tip deflection in the flap-wise direction on T3. On the left the cases for the 8m/s wind speed are shown while 14m/s is on the right.

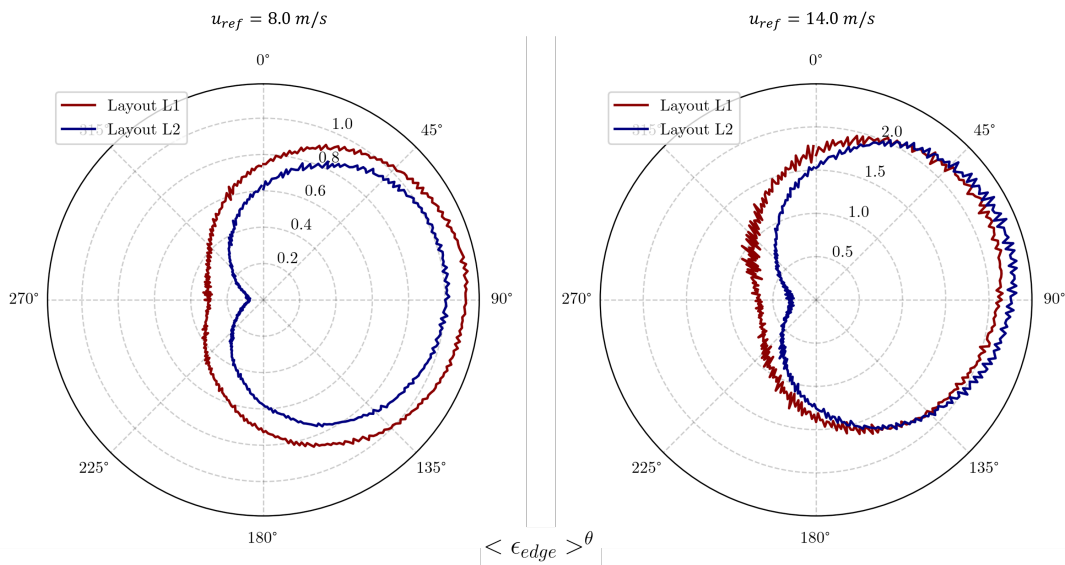


Figure 6.16: The azimuthal distribution of the tip deflection in the edge-wise direction on T3. On the left the cases for the 8m/s wind speed are shown while 14m/s is on the right.

The tip deflection in the edge-wise direction is shown in Fig. 6.16. An approximately kidney-shaped profile is observed for $\langle \epsilon_{edge} \rangle_{\theta}$. This is also a result of the change in the direction of gravitational force when the blade crosses the 180° point. Unlike the edge-wise forces, the deflection does not change sign due to the stiffness of the blade. In the 8m/s cases, the deflection is 40% higher in L1 than in L2. This is due to the average wind speed and thrust force being larger in this case. Indeed, on the left half of T3 in L2, the wind speed is close to 5m/s such that the weaker thrust force provides less resistance to the opposing gravitational force at 270°. Thus, there is a sharp dip in the blade deflection at this point. For the

14m/s case, T3 in L2 experiences higher wind speeds, as seen in Fig. 6.9. This, along with the increase in pitch angle results in the edge-wise deflection being 10% more in L2.

Thus, it can be established that the partial wake conditions to which T3 is exposed to in L1 and L2 produce significant fluctuations in the loads experienced by the blade. These variation occur not just in the azimuth but also vary with time as a result of turbulence in the wake. The subsequent impact of the load cycles on the fatigue life of the turbine forms the topic of the next section.

6.2.3. An evaluation of the fatigue damage

The fatigue damage accumulated by the turbines has been quantified using the Damage Equivalent Load (DEL) [100] which is part of the wind turbine design standards [75]. The DEL is related to the Miner's rule for computing the damage accumulated when a time-varying stress with zero mean is applied to an elastic structure:

$$D = \sum_{i=1}^n \frac{n_i^c}{N_i^F}, \quad (6.4)$$

where n_i^c is the number of cycles at a particular stress amplitude present in the load signal, N_i^F is the cycles to failure for that stress amplitude and n is the number of bins into which the stress amplitudes are categorized. The method for computing D is as follows. Once the stress data are binned, n_i^c is calculated via the rain-flow counting algorithm [101]. Then for each stress amplitude, N_i^F is computed from the Wohler or S-N curves. After summing over all the stress bins, the damage accumulated during the time range of the stress signal is obtained. DEL is then the stress amplitude which when applied for a certain number of cycles, produces the same damage D :

$$DEL = \left(\sum_{i=1}^n \frac{n_i^c M_{a,i}^m}{n_i^{c,eq}} \right)^{\frac{1}{m}}, \quad (6.5)$$

where $M_{a,i}$ is the moment amplitude (in Nm) and m is the slope of the Wohler curve, such that:

$$N_{F,i} = k M_{a,i}^{-m}, \quad (6.6)$$

with k being the material constant. Additionally, $n_i^{c,eq}$ is taken as 10 million cycles [102]. Here, the DEL is computed for the flap and edge-wise moments at the blade root as well as the yaw moment at the tower-top. The latter is taken into consideration since the partial-wake is expected to induce a net non-zero yaw moment on the rotor even at zero yaw misalignment. For all the cases, the time length corresponding to 100 cycles of the rotor is taken into consideration. For the flap and edge-wise DEL , m is taken as 10 for the glass fiber composite used in the blades. For the tower manufactured from low-carbon steel, m is 3 [103]. For the rain-flow counting, a bin size of 0.1MNm is considered with a range of 0 to 20MNm. It should also be mentioned that the rain-flow algorithm assumes that the mean stress amplitude is zero. The Wohler curve is also used under this assumption. The non-zero mean stresses require special treatment which is outside the scope of this project.

The DEL for the three load channels are presented in Fig. 6.17, Fig. 6.18 and Fig. 6.19. It is expressed as the relative difference with respect to the DEL for T1 in the L1 8m/s case:

$$\Delta DEL_{flap} = \frac{DEL_{flap}^{T3} - DEL_{flap}^{T1}}{DEL_{flap}^{T1}} * 100. \quad (6.7)$$

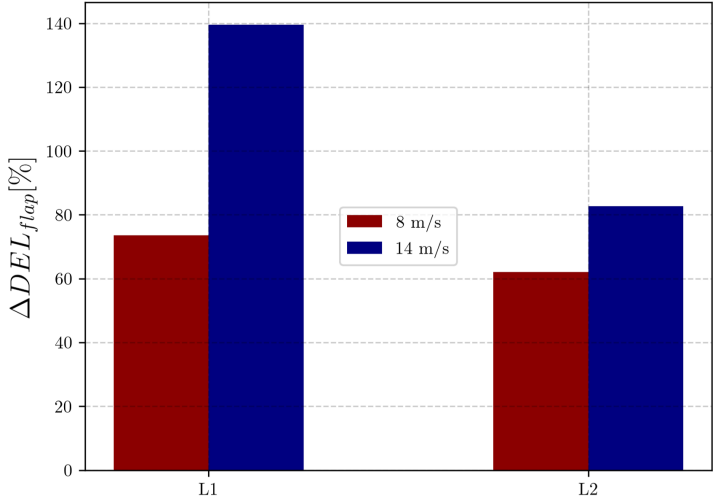


Figure 6.17: The Damage Equivalent Load in the flap-wise direction at the blade root of T3 expressed as the relative difference with respect to T1

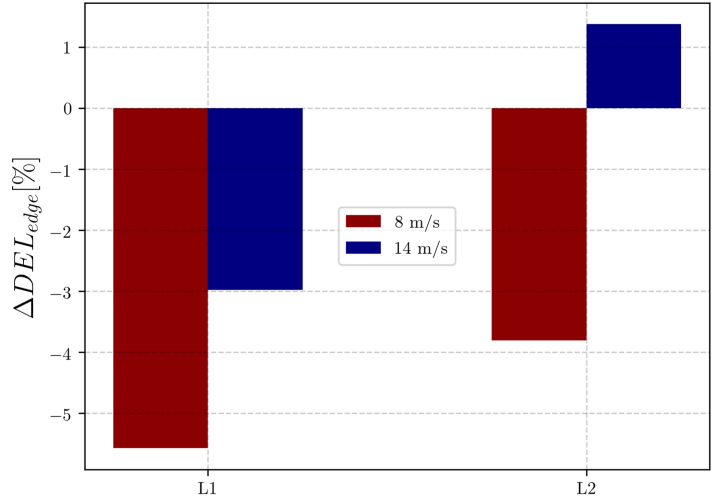


Figure 6.18: The Damage Equivalent Load in the edge-wise direction at the blade root of T3 expressed as the relative difference with respect to T1

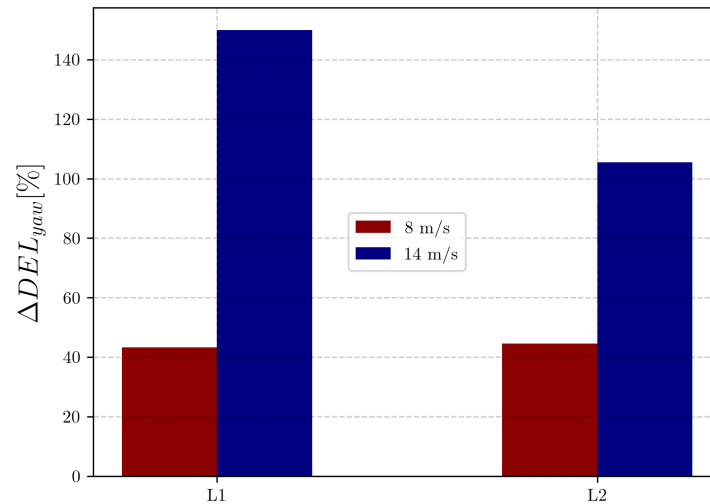


Figure 6.19: The Damage Equivalent Load in yaw on the tower top of T3 expressed as the relative difference with respect to T1

The detrimental effect of the wake is apparent from the fact that for all the cases, the fatigue damage in the flap-wise direction is at least 60% higher than for T1. Comparing between L1 and L2, it is 10 and 35% higher in L1 at 8 and 14m/s respectively. On the other hand, the difference in edge-wise DEL is limited to 4% at $u_{ref} = 14m/s$. The DEL of the tower-top yaw moment is 5 and 25% higher in L1 at 8 and 14m/s respectively.

The difference in the flap-wise DEL between L1 and L2 stems from the azimuthal distribution of the inflow on T3. As mentioned before, the rotor-averaged TI in L1 and L2 is similar, being 10% for the 8m/s case and 8% for the 14m/s one. This is partly responsible for the increase in DEL for T3 when compared to T1. But what differentiates the two configurations is the fluctuations experienced by the blade as it rotates around hub. Indeed, for the 14m/s cases, even the stress amplitude, M_{flap}^{T3} , is the same in both the layouts. Thus, the azimuthal distribution of the wake causes the difference in DEL . The increase in DEL with the wind speed, on the other hand, may be due to the higher magnitude of flap-wise loads rather than the change in the spatial distribution of the inflow. Fig. 6.19 can also be explained by a similar reasoning. Finally, there is no significant difference in the edge-wise fatigue damage between the two layouts. This is because at the wind speeds studied in this chapter, the pitch angle is low. Correspondingly, the component of the thrust force in the edge-wise direction is small and hence the fluctuations in the inflow do not have a large effect.

In summary, it can be verified from Fig. 6.8 and Fig. 6.9 that the velocity field incident on T3 is more non-uniform in the azimuthal and radial direction in layout L1 than in L2. Consequently, the variation in the structural response of the turbine is highlighted by Fig. 6.13 and Fig. 6.15. It can now be concluded that the resultant load cycling is detrimental to the fatigue life. Moreover, it is sensitive to the spatial distribution of the inflow. This is highly relevant for low-fidelity wake models used in the design and certification of wind turbines. Reduction in complexity, for example with the axisymmetric assumption or by averaging the velocity field on the rotor plane, must be done with utmost care since it can lead to erroneous load estimation. Special treatment must be given to the full, half or quarter wake interaction to which the turbine is subjected.

Thus, the discussion on partial-wake interaction can be concluded. The next chapter summarizes the most important insights from this project and provides recommendations for future studies.

Conclusion and recommendations

The aim of this project was to gather insights into the physics of wind turbine wake interactions with the aid of aero-servo-elastic Large Eddy simulations. This involved a number of milestones which began from generating a turbulent inflow and was followed by the implementation of a workflow to automatize the chain of simulations. Next, the workflow was applied to study the sensitivity of the wake to the inflow conditions. Finally, the structural impact of different partial wake situations was investigated.

This study relied on Actuator Line Large Eddy Simulations (ALM-LES), through the CFD library YALES2. LES allowed a reduction in the computational demand by decreasing the spatial and temporal scales of the flow field that need to be resolved. The Actuator Line method introduced an additional reduction in cost since it was no longer necessary to resolve the geometry of the blade. Instead, a model was used that emulated the blade behaviour. The effects of blade deformation and realistic turbine control were included by the coupling with the servo-elastic solver BHawC.

7.1. A reply to the research questions

This section provides an answer to the questions stated in Chapter 2 and provides the relevant future prospects.

What method can generate inflow turbulence for Large Eddy Simulations of wind turbine wakes such that the turbulence itself is fully developed and close to offshore conditions? In particular, what are the required boundary conditions and domain dimensions?

In Chapter 3, the recycling method was selected for generation of turbulent inflow. The length of the computational domain used in wind turbine wake simulations requires a fully developed turbulent inflow to prevent stream-wise evolution of the turbulent properties. A recycling method was able to achieve this while allowing sufficient control over the properties of the resultant flow field. Through a sensitivity study of velocity field to the boundary conditions and domain size, it was found that a vertical velocity profile close to the power law could be obtained by sufficient grid refinement and limiting the domain height. Additionally, periodic side-walls were used in the recycling zone to allow the unconstrained development of the turbulence in lateral direction. By specification of the flow-rate at the inlet and the ground roughness, it was possible to approximate conditions seen in typical offshore wind farms. But, a non-uniformity in the velocity along the lateral direction was also observed which did not disappear when increasing the domain width. Since the fluctuations were less than 2% of the velocity at hub height, especially over the rotor plane, it was judged that its impact on the turbine response and wake velocity profiles would be limited. Lastly, the vertical velocity profile and the rotor-averaged TI were found to be invariant to a 20% decrease in the recycling length. This resulted in a 10% decrease in the computational cost .

The next steps in this topic can focus on including the effects of temperature and buoyancy. This would provide a better emulation of atmospheric flow. The parametric study can be repeated to determine the effect of the surface temperature on the resultant flow field. An analysis of more turbulence properties such as the length scale, the two-point correlation and the energy spectra can also be included in the post-processing framework. This would provide more information while selecting an external turbulent flow for the subsequent wind turbine wake simulations. For example, if a particular length scale is desired, the corresponding solution can be chosen.

Can the usability of elastic ALM-LES be extended to parametric studies? This would involve a reduction in the human-time spent on the different steps of a simulation. Thus, in other words, what methodology can consolidate and automatize elastic ALM-LES of wind turbine wake while ensuring that it is easily adaptable to different user inputs

Chapter 4 described a robust mesh generation strategy and addressed the limitation of wind turbine wake simulations through ALM-LES which was the large amount of human-time required for setting up a simulation. Indeed regarding the mesh framework, the wake was flagged based on properties of the flow itself, not relying on human judgement. The subsequent refinement procedure was robust to changes in the inflow conditions and turbine layout. It was also able to reduce the amount of over-refinement while ensuring that the wake was always within the refined zone. Then, the steps of specifying the boundary conditions and solver settings, generation and convergence of turbulent inflow, mesh adaptation, wake flow convergence and accumulation of final statistics were consolidated into a single workflow. Herein, the user was only required to provide the initial setup such as the turbine layout, boundary conditions, etc. Subsequently, the final results could be obtained with minimal usage of human-time. Additionally, there was confidence in the results as the automatic framework minimized the possibility of bugs. Thus, parametric studies of wind turbine wakes became more feasible.

In this regard, the workflow can be used to carry out more parametric studies. For example, the effect of stream-wise turbine spacing or yaw offsets on wake recovery can be analysed. Similar to this thesis, the studies can reveal insights into the nature of wind turbine wakes and help improve engineering models. Or, the workflow can be used for load analysis during the design phase. As shown in Chapter 6, large amount of information can be obtained regarding the structural response. But, this would require a reduction in the computational cost. The cost of the coupling between YALES2 and BHawC can also be reduced by sub-stepping wherein the fluid domain is not solved for every time step. Another optimization would involve reducing the number of processors that register the actuator line data, which can improve the performance of the LES solver.

What is the impact of different inflow conditions, namely wind speed and turbulence intensity, on wake recovery, meandering and power production in multi-wake situation?

The aforementioned workflow was used in Chapter 5 to study the impact of the inflow wind speed and turbulence intensity (TI) on the wake behind a three turbine in-line configuration. Three wind speeds corresponding to below-, at- and above-rated operation of the turbine along with two turbulence intensities were simulated. Their effect on the velocity and TI profiles in the wake, wake recovery, power production and wake meandering was observed. From the vertical and lateral velocity profiles, it was seen that increasing the TI_{ref} from 5% to 10% led to 25% and 35% more wake expansion in the vertical and lateral directions respectively. Next, the time-averaged power production of all three turbines was analysed. It revealed that when the inflow wind speed is below-rated, the last turbine produces 25% more power than the middle one. Subsequently, the effect of the inflow conditions on wake recovery was studied. Here, $\langle U_x \rangle$ in the wake was averaged over the rotor plane at different stream-wise locations. It was observed that at $u_{ref} = 8m/s$, the wake recovered at a similar rate, irrespective of TI_{ref} . But at $u_{ref} = 14m/s$, wake recovery was 30% faster in the 10% TI_{ref} case. This points to the possibility that at low wind speeds, wake recovery in a multi-turbine configuration is driven by the wake-added turbulence and not the ambient turbulence. Lastly, the impact of the inflow turbulence on the wake meandering was investigated. When the ambient TI_y changed from 4% to 8%, the standard deviation in the wake center position increased by 60%. But a change in u_{ref} had no effect on the time-averaged wake center. This provides further validation of the literature by replicating the increase in meandering with the ambient TI and strengthens the hypothesis that meandering is driven by the external flow [95].

Overall, it is observed that the velocity field in the wake is affected not just by the ambient TI but also the wind speed. The latter determines the operating point of neighbouring turbines which in-turn affects their thrust and the wake-added turbulence. Thus, the improvement of engineering models [5] should focus on capturing the effect of the neighbouring turbines not just in terms of the reduced wind speed but also the wake-added turbulence. This can lead to better estimates of turbine loads and farm yield.

Additionally, the dependence of wake recovery on the wind speed (or turbine thrust) and the ambient TI requires further investigation. The results indicate that when a number of turbines operate in a line, the wake-added turbulence at low wind speeds might be more significant than the ambient turbulence. An analysis of the momentum and energy budgets can shed more light on this phenomenon.

How important is it to consider the wake position on the downstream rotor in different partial-wake situations when assessing the fatigue damage accumulated by the blade?

This question was discussed in Chapter 6 where two layouts of the turbines were studied: L1 and L2. L1 corresponded to the last turbine, T3, operating partly in free-stream and partly in wake conditions. While in L2, T3 was completely under wake inflow as its left half was under wake from T2 while the right half was under wake from T1. Two different wind speeds were also analysed. From the flow topology, it was observed that T3 in L1 experienced a sharp horizontal shear in the incident velocity field. But in L2, the stream-wise velocity incident on T3 was more uniform and the rotor-averaged TI in both the cases was similar. Next, the structural response of the blade was analysed in the flap and edge-wise directions. The spatial distribution of the velocity field on the rotor plane of the waked turbines led to a corresponding variation in the forces and tip deflection of the blade. Here, the difference between the two layouts was more apparent in the flap-wise direction. The resultant effect of the cyclic loading on the blade fatigue damage was quantified by the Damage Equivalent Load (DEL). This revealed that at $u_{ref} = 14m/s$, the blade underwent 35% more flap-wise damage in the L1 configuration. The difference in edge-wise DEL was limited to 4 % while the DEL in the yaw moment on the tower top increased by 25%. This showed the importance of considering the azimuthal and radial distribution of the wake on the rotor plane when evaluating the structural response of the turbine.

Thus, engineering models relying on the rotor-averaged wind speed or TI [99] to evaluate the fatigue damage can produce erroneous results if the spatial distribution of the wake is not considered. Subsequently, they can be improved by parameterizing and modelling the effect of different partial-wake scenarios. This will reduce the over-conservativeness if a high safety factor is used to compensate for the lack of sufficient flow resolution. The difference between partial-wake and full-wake also needs to be further analysed by repeating the present study with T3 in full wake of T2 and T1. Here, more load channels, such as the shaft torsion and tower fore-aft moment, can be included in the post-processing setup.

References

- [1] *Wind Electricity – Analysis - IEA*. URL: <https://www.iea.org/reports/wind-electricity>.
- [2] IRENA. “Future of Wind”. In: *International Renewable Energy Agency (IRENA) is* (2019), pp. 18–19.
- [3] A. Elia et al. “Wind turbine cost reduction: A detailed bottom-up analysis of innovation drivers”. In: *Energy Policy* 147 (Dec. 2020), p. 111912. DOI: 10.1016/J.ENPOL.2020.111912.
- [4] Kelsey Shaler et al. “Sensitivity analysis of the effect of wind and wake characteristics on wind turbine loads in a small wind farm”. In: *Wind Energy Science* 8.1 (Jan. 2023), pp. 25–40. DOI: 10.5194/wes-8-25-2023.
- [5] Fernando Porté-Agel et al. “Wind-Turbine and Wind-Farm Flows: A Review”. In: *Boundary-Layer Meteorology* 174.1 (Jan. 2020), pp. 1–59. DOI: 10.1007/s10546-019-00473-0.
- [6] D. Mehta et al. “Large Eddy Simulation of wind farm aerodynamics: A review”. In: *Journal of Wind Engineering and Industrial Aerodynamics* 133 (Aug. 2014), pp. 1–17. DOI: 10.1016/j.jweia.2014.07.002.
- [7] Sal Rodriguez et al. *Applied Computational Fluid Dynamics and Turbulence Modeling*. Tech. rep.
- [8] Jens Nørkær Sørensen et al. “Numerical Modeling of Wind Turbine Wakes”. In: *Journal of Fluids Engineering* 124.2 (June 2002), pp. 393–399. DOI: 10.1115/1.1471361. URL: <https://asmedigitalcollection.asme.org/fluidsengineering/article/124/2/393/444521/Numerical-Modeling-of-Wind-Turbine-Wakes>.
- [9] Vincent Moureau et al. “Design of a massively parallel CFD code for complex geometries”. In: *Comptes Rendus Mécanique* 339.2-3 (Feb. 2011), pp. 141–148. DOI: 10.1016/J.CRME.2010.12.001.
- [10] Peter Fisker Skjoldan. *Aeroelastic modal dynamics of wind turbines including anisotropic effects*. Risø National Laboratory, 2011.
- [11] L. J. Vermeer et al. *Wind turbine wake aerodynamics*. 2003. DOI: 10.1016/S0376-0421(03)00078-2.
- [12] “Handbook of Wind Energy Aerodynamics”. In: *Handbook of Wind Energy Aerodynamics* (2022). DOI: 10.1007/978-3-030-31307-4.
- [13] Benjamin Sanderse. *Aerodynamics of wind turbine wakes Literature review B*. Sanderse. Tech. rep.
- [14] Ding Liao et al. “Fatigue reliability of wind turbines: historical perspectives, recent developments and future prospects”. In: *Renewable Energy* 200 (Nov. 2022), pp. 724–742. DOI: 10.1016/j.renene.2022.09.093.
- [15] M J Churchfield et al. *A Comparison of the Dynamic Wake Meandering Model, Large-Eddy Simulation, and Field Data at the Egmond aan Zee Offshore Wind Plant: Preprint*. Tech. rep. 2015. URL: www.nrel.gov/publications.
- [16] David Bastine et al. “Stochastic Wake Modelling Based on POD Analysis”. In: *Energies* 2018, Vol. 11, Page 612 11.3 (Mar. 2018), p. 612. DOI: 10.3390/EN11030612. URL: <https://www.mdpi.com/1996-1073/11/3/612/htm%20https://www.mdpi.com/1996-1073/11/3/612>.
- [17] Zilong Ti et al. “Wake modeling of wind turbines using machine learning”. In: *Applied Energy* 257 (Jan. 2020), p. 114025. DOI: 10.1016/J.APENERGY.2019.114025.
- [18] Maciej Serda et al. “Dynamic wake meandering modeling”. In: *Uniwersytet śląski* 7.1 (2007). Ed. by G. Balint et al., pp. 343–354. DOI: 10.2/JQUERY.MIN.JS. URL: <https://orbit.dtu.dk/en/publications/dynamic-wake-meandering-modeling>.

- [19] Kelsey Shaler et al. "Benchmarking of a Free Vortex Wake Model for Prediction of Wake Interactions". In: *Renewable Energy* 136 (June 2019), pp. 607–620. DOI: 10.1016/J.RENENE.2018.12.044.
- [20] R. Courant et al. "On the Partial Difference Equations of Mathematical Physics". In: *IBM Journal of Research and Development* 11.2 (Apr. 1967), pp. 215–234. DOI: 10.1147/RD.112.0215.
- [21] Ye Zhou. *Turbulence theories and statistical closure approaches*. Nov. 2021. DOI: 10.1016/j.physrep.2021.07.001.
- [22] D Laurence et al. *Engineering Turbulence Modelling and Experiments-4 W Strategies for turbulence modelling and simulations*. Tech. rep.
- [23] Pierre Sagaut. *Large Eddy Simulation for Incompressible Flows*. 2006.
- [24] Pankaj K. Jha et al. "Guidelines for volume force distributions within actuator line modeling of wind turbines on large-eddy simulation-type grids". In: *Journal of Solar Energy Engineering, Transactions of the ASME* 136.3 (Aug. 2014). DOI: 10.1115/1.4026252/379616. URL: <https://asmedigitalcollection.asme.org/solarenergyengineering/article/136/3/031003/379616/Guidelines-for-Volume-Force-Distributions-Within>.
- [25] H. Sarlak et al. "Role of subgrid-scale modeling in large eddy simulation of wind turbine wake interactions". In: *Renewable Energy* 77 (May 2015), pp. 386–399. DOI: 10.1016/J.RENENE.2014.12.036.
- [26] Massimo Germano et al. "A dynamic subgrid-scale eddy viscosity model". In: *Physics of Fluids* 3.7 (1990), pp. 1760–1765. DOI: 10.1063/1.857955.
- [27] Joseph Boussinesq. "Théorie analytique de la chaleur mise en harmonie avec la thermodynamique et avec la théorie mécanique de la lumière : Boussinesq, Joseph, 1842-1929 : Free Download, Borrow, and Streaming : Internet Archive". In: (1901). URL: <https://archive.org/details/thorieanalytiqu00bousgoog/page/n16/mode/2up>.
- [28] Luther H Hodges et al. *DEPARTMENT OF COMMERCE MONTHLY WEATHER REVIEW GENERAL CIRCULATION EXPERIMENTS WITH THE PRIMITIVE EQUATIONS I. THE BASIC EXPERIMENT* 100 MONTHLY WEATHER REVIEW CONTENTS*. Tech. rep. 1963.
- [29] Luis A. Martínez-Tossas et al. "Comparison of four large-eddy simulation research codes and effects of model coefficient and inflow turbulence in actuator-line-based wind turbine modeling". In: *Journal of Renewable and Sustainable Energy* 10.3 (May 2018). DOI: 10.1063/1.5004710.
- [30] *YALES2 public page - www.coria-cfd.fr*. URL: <https://www.coria-cfd.fr/index.php/YALES2>.
- [31] *Open MPI: Open Source High Performance Computing*. URL: <https://www.open-mpi.org/>.
- [32] *GitHub - KarypisLab/METIS: METIS - Serial Graph Partitioning and Fill-reducing Matrix Ordering*. URL: <https://github.com/KarypisLab/METIS>.
- [33] *Mmg Platform – Upgrade your meshes*. URL: <http://www.mmgtools.org/>.
- [34] Nicolas Legrand et al. "A multi-grid framework for the extraction of large-scale vortices in Large-Eddy Simulation". In: *J. Comput. Phys.* 349 (Nov. 2017), pp. 528–560. DOI: 10.1016/J.JCP.2017.08.030.
- [35] V. Moureau et al. "From Large-Eddy Simulation to Direct Numerical Simulation of a lean premixed swirl flame: Filtered laminar flame-PDF modeling". In: *Combustion and Flame* 158.7 (July 2011), pp. 1340–1357. DOI: 10.1016/j.combustflame.2010.12.004.
- [36] Felix Houtin-Mongrolle. "Investigations of yawed offshore wind turbine interactions through aero-servo-elastic Large Eddy Simulations". PhD thesis. 2022.
- [37] M. Kraushaar. "APPLICATION OF THE COMPRESSIBLE AND LOW-MACH NUMBER APPROACHES TO LARGE-EDDY SIMULATION OF TURBULENT FLOWS IN AERO-ENGINES". PhD thesis. Institut National Polytechnique de Toulouse- INPT, 2011.
- [38] Alexandre Joel Chorin. "The numerical solution of the Navier-Stokes equations for an incompressible fluid". In: *Bulletin of the American Mathematical Society* 73.6 (1967), pp. 928–931. DOI: 10.1090/

- S0002-9904-1967-11853-6. URL: <https://www.ams.org/bull/1967-73-06/S0002-9904-1967-11853-6/>.
- [39] H. A. van der Vorst. "Bi-CGSTAB: A Fast and Smoothly Converging Variant of Bi-CG for the Solution of Nonsymmetric Linear Systems". In: <https://doi.org/10.1137/0913035> 13.2 (July 2006), pp. 631–644. DOI: 10.1137/0913035. URL: <https://epubs.siam.org/doi/10.1137/0913035>.
- [40] Desmond J. Higham. "Condition numbers and their condition numbers". In: *Linear Algebra and its Applications* 214.C (Jan. 1995), pp. 193–213. DOI: 10.1016/0024-3795(93)00066-9.
- [41] Luis A. Martínez et al. "A comparison of actuator disk and actuator line wind turbine models and best practices for their use". In: *50th AIAA Aerospace Sciences Meeting Including the New Horizons Forum and Aerospace Exposition*. 2012. DOI: 10.2514/6.2012-900.
- [42] L. PRANDTL. "Tragflügeltheorie. I. Mitteilung". In: *Nachrichten von der Gesellschaft der Wissenschaften zu Göttingen, Mathematisch-Physikalische Klasse* 1918 (), pp. 451–477.
- [43] Jens N. Sørensen et al. "Unsteady actuator disc model for horizontal axis wind turbines". In: *Journal of Wind Engineering and Industrial Aerodynamics* 39.1-3 (1992), pp. 139–149. DOI: 10.1016/0167-6105(92)90540-Q.
- [44] Jens Nørkær Sørensen et al. "A model for unsteady rotor aerodynamics". In: *Journal of Wind Engineering and Industrial Aerodynamics* 58.3 (1995), pp. 259–275. DOI: 10.1016/0167-6105(95)00027-5.
- [45] Yu Ting Wu et al. "Simulation of Turbulent Flow Inside and Above Wind Farms: Model Validation and Layout Effects". In: *Boundary-Layer Meteorology* 146.2 (Feb. 2013), pp. 181–205. DOI: 10.1007/s10546-012-9757-Y/METRICS. URL: <https://link.springer.com/article/10.1007/s10546-012-9757-y>.
- [46] Wen Zhong Shen et al. "The actuator surface model: A new navier-stokes based model for rotor computations". In: *Journal of Solar Energy Engineering, Transactions of the ASME* 131.1 (Feb. 2009), pp. 0110021–0110029. DOI: 10.1115/1.3027502/444133. URL: <https://asmedigitalcollection.asme.org/solarenergyengineering/article/131/1/011002/444133/The-Actuator-Surface-Model-A-New-Navier-Stokes>.
- [47] C. Sibuet Watters et al. "Application of the actuator surface concept to wind turbine rotor aerodynamics". In: *Wind Energy* 13.5 (July 2010), pp. 433–447. DOI: 10.1002/we.365. URL: <https://onlinelibrary.wiley.com/doi/full/10.1002/we.365%20https://onlinelibrary.wiley.com/doi/abs/10.1002/we.365%20https://onlinelibrary.wiley.com/doi/10.1002/we.365>.
- [48] Matthew J. Churchfield et al. "An advanced actuator line method for wind energy applications and beyond". In: *35th Wind Energy Symposium, 2017* (2017). DOI: 10.2514/6.2017-1998. URL: <https://arc.aiaa.org/doi/10.2514/6.2017-1998>.
- [49] Ronith Stanly et al. "Large-Eddy Simulation of a wind turbine using a Filtered Actuator Line Model". In: *Journal of Wind Engineering and Industrial Aerodynamics* 222 (Mar. 2022). DOI: 10.1016/j.jweia.2021.104868.
- [50] Matthew J. Churchfield et al. "Modeling wind turbine tower and nacelle effects within an actuator line model". In: *33rd Wind Energy Symposium*. American Institute of Aeronautics and Astronautics Inc., 2015. DOI: 10.2514/6.2015-0214.
- [51] Renwei Ji et al. "A novel actuator line-immersed boundary (AL-IB) hybrid approach for wake characteristics prediction of a horizontal-axis wind turbine". In: *Energy Conversion and Management* 253 (Feb. 2022). DOI: 10.1016/j.enconman.2021.115193.
- [52] Patrick J H Volker et al. "A comparative study of wake interactions between wind-aligned and yawed wind turbines using LES and actuator line models". In: *Journal of Physics: Conference Series* 1618.6 (Sept. 2020), p. 062009. DOI: 10.1088/1742-6596/1618/6/062009. URL: <https://iopscience.iop.org/article/10.1088/1742-6596/1618/6/062009%20https://iopscience.iop.org/article/10.1088/1742-6596/1618/6/062009/meta>.

- [53] F. Castellani et al. “CFD three dimensional wake analysis in complex terrain”. In: *Journal of Physics: Conference Series*. Vol. 923. 1. Institute of Physics Publishing, Nov. 2017. DOI: 10.1088/1742-6596/923/1/012031.
- [54] *OpenFAST | Wind Research | NREL*. URL: <https://www.nrel.gov/wind/nwtc/openfast.html>.
- [55] Taeseong Kim et al. “Development of an anisotropic beam finite element for composite wind turbine blades in multibody system”. In: *Renewable Energy* 59 (Nov. 2013), pp. 172–183. DOI: 10.1016/J.RENENE.2013.03.033.
- [56] Ming Chen Hsu et al. “Fluid-structure interaction modeling of wind turbines: Simulating the full machine”. In: *Computational Mechanics* 50.6 (Dec. 2012), pp. 821–833. DOI: 10.1007/S00466-012-0772-0/METRICS. URL: <https://link.springer.com/article/10.1007/s00466-012-0772-0>.
- [57] Fabián Duarte et al. “Arbitrary Lagrangian–Eulerian method for Navier–Stokes equations with moving boundaries”. In: *Computer Methods in Applied Mechanics and Engineering* 193.45-47 (Nov. 2004), pp. 4819–4836. DOI: 10.1016/J.CMA.2004.05.003.
- [58] *SOWFA: Simulator fOr Wind Farm Applications | Wind Research | NREL*. URL: <https://www.nrel.gov/wind/nwtc/sowfa.html>.
- [59] *OpenFOAM | Free CFD Software | The OpenFOAM Foundation*. URL: <https://openfoam.org/>.
- [60] Yefeng Cai et al. “Effects of yawed inflow and blade-tower interaction on the aerodynamic and wake characteristics of a horizontal-axis wind turbine”. In: *Energy* 264 (Feb. 2023). DOI: 10.1016/j.energy.2022.126246.
- [61] Ziyang Yu et al. “Aeroelastic Performance Analysis of Wind Turbine in the Wake with a New Elastic Actuator Line Model”. In: *Water* 2020, Vol. 12, Page 1233 12.5 (Apr. 2020), p. 1233. DOI: 10.3390/W12051233. URL: <https://www.mdpi.com/2073-4441/12/5/1233/htm%20https://www.mdpi.com/2073-4441/12/5/1233>.
- [62] Jiancai Zheng et al. “Numerical investigations of coupled aeroelastic performance of wind turbines by elastic actuator line model”. In: *Applied Energy* 330 (Jan. 2023). DOI: 10.1016/j.apenergy.2022.120361.
- [63] W. Chanprasert et al. “Large Eddy Simulation of wind turbine wake interaction in directionally sheared inflows”. In: *Renewable Energy* (Dec. 2022). DOI: 10.1016/j.renene.2022.11.021.
- [64] W. Chanprasert et al. “Large Eddy Simulation of wind turbine fatigue loading and yaw dynamics induced by wake turbulence”. In: *Renewable Energy* 190 (May 2022), pp. 208–222. DOI: 10.1016/J.RENENE.2022.03.097.
- [65] Joachim C. Heinz et al. “Fluid–structure interaction computations for geometrically resolved rotor simulations using CFD”. In: *Wind Energy* 19.12 (Dec. 2016), pp. 2205–2221. DOI: 10.1002/WE.1976.
- [66] Christian Grinderslev et al. “Wind turbines in atmospheric flow: Fluid-structure interaction simulations with hybrid turbulence modeling”. In: *Wind Energy Science* 6.3 (May 2021), pp. 627–643. DOI: 10.5194/WES-6-627-2021.
- [67] Joachim C. Heinz et al. “Vortex-induced vibrations on a modern wind turbine blade”. In: *Wind Energy* 19.11 (Nov. 2016), pp. 2041–2051. DOI: 10.1002/WE.1967. URL: <https://onlinelibrary.wiley.com/doi/full/10.1002/we.1967%20https://onlinelibrary.wiley.com/doi/abs/10.1002/we.1967%20https://onlinelibrary.wiley.com/doi/10.1002/we.1967>.
- [68] Chuan Chen et al. “Stall-induced vibrations analysis and mitigation of a wind turbine rotor at idling state: Theory and experiment”. In: *Renewable Energy* 187 (Mar. 2022), pp. 710–727. DOI: 10.1016/J.RENENE.2022.01.078.
- [69] Marc Bromm et al. “Numerical investigation of wind turbine wake development in directionally sheared inflow”. In: *Wind Energy* 20.3 (2017), pp. 381–395. DOI: <https://doi.org/10.1002/we.2010>. URL: <https://onlinelibrary.wiley.com/doi/abs/10.1002/we.2010>.

- [70] Xiaohua Wu. “Inflow Turbulence Generation Methods”. In: *Annual Review of Fluid Mechanics* 49.1 (2017), pp. 23–49. DOI: 10.1146/annurev-fluid-010816-060322. URL: <https://doi.org/10.1146/annurev-fluid-010816-060322>.
- [71] B. Dose et al. “Fluid-structure coupled computations of the NREL 5 MW wind turbine by means of CFD”. In: *Renewable Energy* 129 (Dec. 2018), pp. 591–605. DOI: 10.1016/j.renene.2018.05.064.
- [72] B. Elie et al. “Simulation of two in-line wind turbines using an incompressible Finite Volume solver coupled with a Blade Element Model”. In: *Renewable Energy* 187 (Mar. 2022), pp. 81–93. DOI: 10.1016/j.renene.2021.12.082.
- [73] Shun Xu et al. *A Review of High-Fidelity Computational Fluid Dynamics for Floating Offshore Wind Turbines*. Oct. 2022. DOI: 10.3390/jmse10101357.
- [74] Etienne Muller et al. “Field data based validation of an aero-servo-elastic solver for high-fidelity LES of industrial wind turbines”. In: (). DOI: 10.5194/wes-2023-41. URL: <https://doi.org/10.5194/wes-2023-41>.
- [75] *IEC 61400-1:2019 | IEC Webstore | rural electrification, wind power*. URL: <https://webstore.iec.ch/publication/26423>.
- [76] G. R. Tabor et al. *Inlet conditions for large eddy simulation: A review*. Apr. 2010. DOI: 10.1016/j.compfluid.2009.10.007.
- [77] J. L. Lumley. “Interpretation of Time Spectra Measured in High-Intensity Shear Flows”. In: *The Physics of Fluids* 8.6 (June 1965), pp. 1056–1062. DOI: 10.1063/1.1761355. URL: [/aip/pfl/article/8/6/1056/824966/Interpretation-of-Time-Spectra-Measured-in-High](https://aip/pfl/article/8/6/1056/824966/Interpretation-of-Time-Spectra-Measured-in-High).
- [78] Jakob Mann. “Wind field simulation”. In: *Probabilistic Engineering Mechanics* 13.4 (Oct. 1998), pp. 269–282. DOI: 10.1016/S0266-8920(97)00036-2.
- [79] P. Druault et al. “Generation of Three-Dimensional Turbulent Inlet Conditions for Large-Eddy Simulation”. In: <https://doi.org/10.2514/1.3946> 42.3 (May 2012), pp. 447–456. DOI: 10.2514/1.3946. URL: <https://arc.aiaa.org/doi/10.2514/1.3946>.
- [80] L. di Mare et al. “Synthetic turbulence inflow conditions for large-eddy simulation”. In: *Physics of Fluids* 18.2 (Feb. 2006). DOI: 10.1063/1.2130744/255709. URL: [/aip/pof/article/18/2/025107/255709/Synthetic-turbulence-inflow-conditions-for-large](https://aip/pof/article/18/2/025107/255709/Synthetic-turbulence-inflow-conditions-for-large).
- [81] Serge Meynet et al. “Roughness-Resolved Large-Eddy Simulation of Additive Manufacturing-Like Channel Flows”. In: *Journal of Turbomachinery* 145.8 (Aug. 2023). DOI: 10.1115/1.4062245. URL: <https://asmedigitalcollection.asme.org/turbomachinery/article/145/8/081013/1160436/Roughness-Resolved-Large-Eddy-Simulation-of>.
- [82] F. Xiao et al. “An LES Turbulent Inflow Generator using A Recycling and Rescaling Method”. In: *Flow, Turbulence and Combustion* 98.3 (Apr. 2017), pp. 663–695. DOI: 10.1007/s10494-016-9778-6.
- [83] L. C. Cheung et al. “A Simple Model for the Turbulence Intensity Distribution in Atmospheric Boundary Layers”. In: *Journal of Physics: Conference Series*. Vol. 753. 3. Institute of Physics Publishing, Oct. 2016. DOI: 10.1088/1742-6596/753/3/032008.
- [84] Matthias Türk et al. “The dependence of offshore turbulence intensity on wind speed”. In: *Journal of Wind Engineering and Industrial Aerodynamics* 98.8-9 (2010), pp. 466–471. DOI: 10.1016/j.jweia.2010.02.005.
- [85] R. Vasaturo et al. “Large eddy simulation of the neutral atmospheric boundary layer: performance evaluation of three inflow methods for terrains with different roughness”. In: *Journal of Wind Engineering and Industrial Aerodynamics* 173 (Feb. 2018), pp. 241–261. DOI: 10.1016/j.jweia.2017.11.025.
- [86] S. Caires et al. “Uncertainties in offshore wind turbulence intensity”. In: *Journal of Physics: Conference Series*. Vol. 1356. 1. Institute of Physics Publishing, Oct. 2019. DOI: 10.1088/1742-6596/1356/1/012037.

- [87] B. W. Yan et al. "Characterising wind shear exponents in the offshore area using Lidar measurements". In: *Applied Ocean Research* 127 (Oct. 2022). DOI: 10.1016/j.apor.2022.103293.
- [88] Olivier Desjardins et al. "An accurate conservative level set/ghost fluid method for simulating turbulent atomization". In: *Journal of Computational Physics* 227.18 (Sept. 2008), pp. 8395–8416. DOI: 10.1016/j.jcp.2008.05.027.
- [89] F. Houtin - Mongrolle et al. "A level-set framework for the wind turbine wake analysis: from high-fidelity unsteady simulations to 1D momentum theory". In: *Journal of Physics: Conference Series* 1934.1 (May 2021), p. 012011. DOI: 10.1088/1742-6596/1934/1/012011. URL: <https://iopscience.iop.org/article/10.1088/1742-6596/1934/1/012011><https://iopscience.iop.org/article/10.1088/1742-6596/1934/1/012011/meta>.
- [90] Jang Oh Mo et al. "Large eddy simulation of the wind turbine wake characteristics in the numerical wind tunnel model". In: *Journal of Wind Engineering and Industrial Aerodynamics* 112 (2013), pp. 11–24. DOI: 10.1016/j.jweia.2012.09.002.
- [91] R. J. Barthelmie et al. *Flow and wakes in large wind farm : final report for UpWind WP8*. Risø DTU - National Laboratory for Sustainable Energy, 2011.
- [92] Christopher Vogel et al. *Investigation of wind turbine wake superposition models using Reynolds-Averaged Navier-Stokes simulations*. Tech. rep.
- [93] Erwan Jézéquel. "Simulations of wind turbine wakes in realistic atmospheric conditions: from large eddy simulations to analytical models." In: (2022).
- [94] N. Coudou et al. "Development of wake meandering detection algorithms and their application to large eddy simulations of an isolated wind turbine and a wind farm". In: *Journal of Physics: Conference Series*. Vol. 1037. 7. Institute of Physics Publishing, June 2018. DOI: 10.1088/1742-6596/1037/7/072024.
- [95] Xiaolei Yang et al. *A review on the meandering of wind turbine wakes*. Dec. 2019. DOI: 10.3390/en12244725.
- [96] D. Onnen et al. "Dynamic wake tracking based on wind turbine rotor loads and Kalman filtering". In: *Journal of Physics: Conference Series*. Vol. 2265. 2. Institute of Physics, June 2022. DOI: 10.1088/1742-6596/2265/2/022024.
- [97] Lukas Vollmer et al. "Estimating the wake deflection downstream of a wind turbine in different atmospheric stabilities: An LES study". In: *Wind Energy Science* 1.2 (July 2016), pp. 129–141. DOI: 10.5194/wes-1-129-2016.
- [98] Milan Meloun et al. *Statistical Data Analysis: A Practical Guide*. Elsevier, Jan. 2011, pp. 1–773. DOI: 10.1533/9780857097200.frontmatter. URL: <http://www.sciencedirect.com:5070/book/9780857091093/statistical-data-analysis>.
- [99] Tuhfe Göçmen et al. *Wind turbine wake models developed at the technical university of Denmark: A review*. July 2016. DOI: 10.1016/j.rser.2016.01.113.
- [100] J P A A Blasques et al. *Mean load effects on the fatigue life of offshore wind turbine monopile foundations*. Tech. rep. 2013, pp. 818–829.
- [101] M. Matsuichi et al. "Fatigue of metals subjected to varying stress". In: (1968).
- [102] H B Hendriks et al. *Fatigue Equivalent Load Cycle Method A General Method to Compare the Fatigue Loading of Different Load Spectrums Fatigue Equivalent Load Cycle Method*. Tech. rep. 1995.
- [103] *The new guideline for the certification of wind turbines, edition 2010 DNV*. URL: <https://www.dnv.com/publications/the-new-guideline-for-the-certification-of-wind-turbines-edition-2010-71595>.



Appendix 1: Estimation of CPU costs

The computational cost of all the simulations carried out for Chapter 5 and Chapter 6 are shown in Table A.1. The wall clock time and CPU consumption are with reference to the 8m/s wind speed cases since these correspond to the longest physical time of the simulation.

Table A.1: Overview of Wall Clock Time, Number of Processors and CPU consumption for the simulations of Chapter 5 and 6.

Workflow	Step	WCT (hrs)	Nprocs	CPUhrs	WCT per 1s of physical time
Chapter 5	1	22.0	128	2800	2.79
	2	3.6	128	460	13.74
	3	7.5	128	960	13.74
	4	32.5	3465	76990	-
	5	33.5	2560	85760	208.83
	6	52.7	2560	135680	208.83
Chapter 6	1	22.0	128	2800	2.79
	2	3.6	128	460	13.74
	3	7.5	128	960	13.74
	4	33.2	3465	81540	-
	5	35.1	2560	89330	208.83
	6	53.6	2560	140680	208.83

For the Chapter 5 the total cost was approximately 1.5M CPUhrs while for Chapter 6 the cost was 1.4M CPUhrs.

A breakdown of the expense of the different steps involved in a single simulation are shown in Table A.2 in terms of the reduced computation time (RCT). This is presented for the last run (no. 5) of the workflow since it is the most expensive step. The RCT is computed as follows:

$$RCT = \frac{WCT \cdot N_{procs}}{N_{\Delta t} \cdot N_n}, \quad (\text{A.1})$$

where WCT is the wall clock time, N_{procs} is the number of processors used, $N_{\Delta t}$ is the number of time-steps completed and N_n is the number of nodes in the simulation.

Table A.2: The Reduced Computational Time (RCT) of the simulation steps.

Step	RCT (μs)
Calculate ∇U	2.2
Calculate ν	8.8
Wall Law	2.3
Actuator Line & coupling	26.1
Recycling	8.5
Pressure correction	76.7
Advection	8.3

It can be observed that the pressure correction step of the Chorin method used in YALES2 is the most expensive step of the simulation. The Actuator line method also has a significant cost due to the source term being registered on all the processors. The Recycling method can also be costly if the recycling frequency is not adjusted based on the time-step. For steps 5 and 6 of the workflow wherein the BHawC coupling is activated and the time-step is reduced to 0.02s, the recycling frequency has to be reduced to ensure its RCT is limited.